Atmospheric Sensing in Tropical Forests Using Unmanned Aerial Vehicles

Share Your Story

HARVARD UNIVERSITY

Graduate School of Arts and Sciences

DISSERTATION ACCEPTANCE CERTIFICATE

The undersigned, appointed by the

Harvard John A. Paulson School of Engineering and Applied Sciences
have examined a dissertation entitled:

"Atmospheric Sensing in Tropical Forests Using Unmanned Aerial Vehicles"

presented by: Tianning Zhao

Signature *Scot Martin*

    Typed name: Professor S. Martin

Signature

    Typed name: Professor J. Vlassak

Signature *Steven C Wofsy*

    Typed name: Professor S. Wofsy

October 28, 2021

Atmospheric Sensing in Tropical Forests Using Unmanned Aerial Vehicles

A dissertation presented

by

Tianning Zhao

to

The School of Engineering and Applied Science

in partial fulfillment of the requirements

for the degree of

Doctor of Philosophy

in the subject of

Engineering Sciences

Harvard University

Cambridge, Massachusetts

Oct 2021

Dissertation Advisor: Professor Scot T. Martin   Author: Tianning Zhao

Atmospheric Sensing in Tropical Forests Using Unmanned Aerial Vehicles

Abstract

Tropical regions play indispensable roles in the energy balance, biogeochemical cycles, and air quality at regional and global scales. The Amazon basin attracts great research interest because of its immense size and complex biosphere-atmosphere interactions. Atmospheric studies benefit from advance in technologies in the past few decades, such as mass spectrometry and satellite. Observational platforms for investigating intermediate-scale phenomena like river winds, however, have been lacking. Local atmospheric recirculation flows (i.e., river winds) induced by thermal contrast between wide Amazon rivers and adjacent forests can affect pollutant dispersion. The transport of urban, fire, and forest pollutant emissions by river winds has implications for the health of the millions of river-side inhabitants.

The combination of miniature sensor and unmanned aerial vehicles (UAVs) opens a new horizon for atmospheric sensing. Herein, different types of low-cost sensors were evaluated and deployed on UAVs to collect data in tropical forests. Commercial metal oxide semiconductor (MOS) sensors were optimized and evaluated for detection of trace-level biogenic volatile organic compound (BVOC). Selectivity among major BVOC species was evaluated and improved with gas separation membrane upstream of a MOS

sensor. Mixed matrix membranes composed of metal organic framework and polymer were able to separate a chemically similar mixture of isoprene and α-pinene. Electrochemical sensors and other meteorological sensors were also pre-calibrated and deployed on the UAVs in the tropical forest.

Daytime vertical profiles of meteorological variables and chemical concentrations up to 500 m were collected by a copter-type unmanned aerial vehicle (UAV) operated from a boat during the 2019 dry season. Cluster analysis showed that a river-forest recirculation flow occurred from surface to 300 m for 23% (13 of 56) of the profiles whereas it was completely absent for 21% of them. In fair weather, the thermally driven river winds fully developed for synoptic wind speeds below 4 m s^{-1}, and during these periods the vertical profiles of carbon monoxide (CO) and total oxidants (O$_x$, defined as O$_3$ + NO$_2$) were significantly altered. Under some conditions, the river winds recirculated pollution back toward the riverbank and its point of origin.

Numerical experiments through large-eddy simulation were validated for river winds simulation with observational data. Simulation results supported that under some conditions river winds can enhance pollutant mixing perpendicular to the river orientation even when the synoptic-scale winds are parallel. The impacts on interpretation of riparian surface measurement depend on locations and should be considered carefully in the future.

The results of this dissertation advance an urgent need to quantify the occurrence and properties of river winds in respect to mesoscale chemical dispersion, air quality, and human health. There are significant implications for the many human settlements along the rivers throughout northern Brazil.

Contents

Contents

List of Tables

List of Figures

Previously Published Work

Chapter 3 and 4 were published as

Zhao, T., Ye, J., Ribeiro, I.O. et al. River winds and pollutant recirculation near the Manaus city in the central Amazon. *Nature Commun Earth Environ* 2, 205 (2021). https://doi.org/10.1038/s43247-021-00277-6. Reproduced under the Creative Commons Attribution 4.0 International License together with an author copyright.

Acknowledgments

When you are doing something with great enjoyment, you do not notice that the time passes. The past four years has shaped my life from all aspects. I'm truly thankful for all the people who brought me here and accompanied me through the journey.

First and foremost, I would like to thank my advisor, Professor Scot Martin, for his invaluable guidance and generous support in the past four years. He gave me the freedom to explore the unknown and always supported me to pursue new ideas. I appreciate the rigorous scientific training I received from him, which cultivated me into a critical thinker and a resilient problem solver. I would also like to thank my PhD qualification exam committee and my PhD thesis committee (sorted alphabetically by last names): Frank Keutsch, Zachary Smith, Elsie Sunderland, Joost Vlassak, and Steve Wofsy. Thank you all for your invaluable support and inspiring discussion.

I was very honored to have the opportunity to work with amazing colleagues at Harvard and beyond. Science happens when there is vibrant discussion and great work is done where collaboration shines. I would like to thank all members of the Martin group, past and present: Pengfei Liu, Jianhuai Ye, Yiming Qin, Matthew Stewart, Hua Li, Yongjing Ma, Zhaoheng Gong, Suzane Simões de Sá, Junfeng Wang, Paul Ohno, Yali Lei, Aruffo Eleonora, and Javier Farago Escobar. Special thanks to Pengfei Liu, my mentor during my summer internship. He ignited my passion for atmospheric science and opened my eyes to see how cool research could be. To Yiming Qin, Jianhuai Ye, and Matthew Stewart, who started at the same time with me in the group, I really appreciate your continuous support and help for the past four years. To Hua Li and Yongjing Ma, who offered generous help to my research, I appreciated your advice and guidance on

pursuing the scientific question rigorously.

I would like to thank my colleagues for the Brazil campaign (sorted alphabetically by last names): Jianhuai Ye, Jian Wang, Matthew Stewart, Igor Ribeiro, Adan Medeiros, Patricia Guimarães, Alex Guenther, Rodrigo de Souza, Jesus Campos, and Carla Batista. I will always remember the great days on the boat over Rio Negro in the Amazon rainforest. I would also like to thank my collaborators for different projects: Hui-Ming Hung, Jordi Vilà-Guerau de Arellano, Won Seok Chi, Gang Han, Andreas Güntner, and Jan Van Den Broek. Thank you for sharing your knowledge expertise and broadening my perspective.

I would like to thank my friends at Harvard for their amazing company in the past four years. To the best chefs at Mellen Street Diner: Muqing Xu, Ruihua Fan, and Chang Liu. To all my friends at Harvard CSSA, who have made my time at Harvard much more memorable. Special thanks to my quarantine buddy Fangyuan Hu, for sharing the laugh and fear during the pandemic. Special thanks to Sijie Chen for gracing my life with his lovely presence. Thank you for supporting me through thick and thin and calming all my inner fears.

Finally, I dedicate this dissertation to my beloved parents. Thank you for being there whenever I needed it and being the source of self-discipline and the root of kindness. I cannot thank enough for all the support and love you have given me. All that I am, or hope to be, I owe to my parents.

Abbreviations

BVOCs	Biogenic volatile organic compounds
CO	Carbon monoxide
LES	Large eddy simulation
MOS	Metal oxide semiconductor
NO_x	Nitrogen oxides
O_3	Ozone
O_x	Total oxidants, $O_3 + NO_2$
UAVs	Unmanned aerial vehicles
VOCs	Volatile organic compounds

但行好事，莫问前程

Keep going, no matter what.

1 Introduction

1.1 Atmospheric science in tropical forests

Understanding tropical regions in natural and perturbed states is crucial to accurately modeling the Earth system. The abundant net surface radiation in tropical regions results in differential heating and consequent pressure gradient at surface level horizontally. Such gradient powers the motion in the atmosphere and in the oceans to compensate for the observed imbalance (Garstang and Fitzjarrald 1999). Tropical regions store large quantities of carbon in the diverse ecosystems such as tropical forest biome. Besides serving as a gigantic carbon reservoir, tropical forests constantly process carbon in great amount via photosynthesis and respiration. Biosphere-atmosphere interactions also emit volatile organic compounds (VOCs), primary and secondary aerosols, which together play an important role in atmospheric composition, energy budget, and cloud dynamics (Pöschl et al. 2010). Even small changes in the tropical forests can lead to major impacts on global and regional climate.

In particular, the Amazon basin greatly influences both the regional climate and the global circulation. Spanning across three million square miles, the Amazon basin occupies 40% of South American continent and has the biggest rainforest in the world (Butler 2020). The immense size and equatorial location make the Amazon an indispensable driving force in the Earth's climate. The strong water evaporation, at a rate of 3 to 3.5 mm d^{-1} year-round, transports the moisture and therefore the latent heat into

the atmosphere, from there it regulates regional rainfall and contributes energy to the

global atmospheric circulation (Nobre et al. 2009). Numerous biogenic volatile organic

compounds (BVOCs) and other trace gases are emitted from the Amazon rainforest to the

atmosphere and the induced atmospheric chemical reactions are pivotal to oxidant

balance and aerosol formation (Kesselmeier et al. 2009). Atmospheric aerosols affect the

global climate in both direct and indirect pathways: they can scatter or adsorb sunlight

directly or modify the cloud formation and change the radiation budget indirectly.

Besides the natural processes, human activities in the Amazon basin also exert

substantial influence on regional climate. Taking Manaus as an example, the urban region

situated at the heart of the Amazon basin has seen great economic growth since the

opening of free trade zone in 1967. Surrounded by the natural forest, the tropical

metropolis in expansion is a huge source of pollution to the natural environment. In the

past few decades, dramatic changes also occurred in the Amazon basin via deforestation

and subsequent conversion to other land-use for capital gains, including cattle-ranches,

soy farms, and palm oil plantations (Lewis 2006). Biomass burning associated with the

deforestation releases various air pollutants into the atmosphere including carbon

monoxide and particulate matters, which can lead to negative effects on human health,

regional air quality, and global climate (Martin et al. 2010).
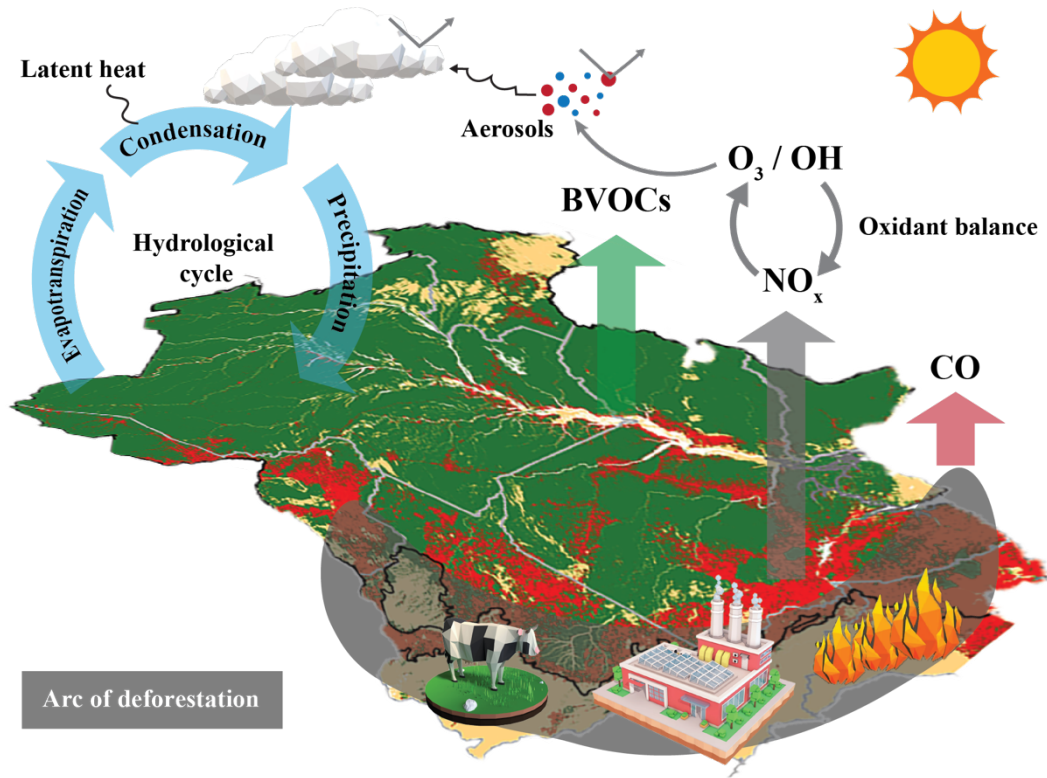
Figure 1-1. Important atmospheric processes in the Amazon Basin related to natural and human activities.

The important atmospheric processes happening in the Amazon Basin related to natural-human activities are summarized in Figure 1-1. Despite the great importance, the understanding of human activities and nature-human interactions has been limited, which leads to great uncertainty in accurate prediction for climate change. One example is the impact of anthropogenic emissions on hydrological cycles. Anthropogenic emissions alter aerosol particle concentration and composition and therefore affect cloud properties, precipitation, and regional climate (Andreae et al. 2004, Martin et al. 2010). These processes can cause changes in the hydrological cycle of the Amazon basin (Davidson et al. 2012). Observations and modeling results regarding net drying or wetting effects remain uncertain, and there are large gaps for understanding the underlying processes (Gloor et al. 2013, Boisier et al. 2015)

Great research effort has been made to advance the understanding in the tropical context. Several intensive field campaigns in the Amazon basin were dedicated to understanding natural functioning of Amazonia and its interaction with the Earth system under natural and perturbed state, including the Large-scale Biosphere-Atmosphere Experiment in Amazonia, the Amazonian Aerosol Characterization Experiment, and the Green Ocean Amazon (Avissar et al. 2002, Martin et al. 2010, Martin et al. 2016). Various data sets have been collected to cover a wide range of scales and resolutions, including field site experimentation, aircraft measurement, remote sensing studies and modelling work. Despite impressive advances, measurements at scales of several hundred meters are still warranted for better understanding of intermediate-scale phenomena.

1.2 Novel technology for atmospheric measurement

1.2.1 Low cost air sensors

Low-cost air sensors refer to a class of affordable technology that reads air pollutant concentration directly and has miniature design for a wide range of applications. Potential uses of low-cost air sensors range from scientific research and supplementing existing monitoring to education and personal exposure monitoring. Application of low-cost sensors in ambient air measurement started in 1990s for automobile exhaust pollution monitoring. Metal oxide sensors with metallic filters were used for ppm-level gas detection of automotive pollutants, such as carbon monoxide and nitrogen dioxide (Pijolat et al. 1999). In the past decade, the application of low-cost sensors becomes more popular in the atmospheric studies, thanks to the advance in sensing technology (Williams et al. 2018).

Recent progress in sensing technology presents a great opportunity to integrate data

from satellites and air quality inference monitors to better understand and communicate

air quality and more broadly, atmospheric science. Low-cost sensor networks can

complement the existing framework by improving the spatial and temporal coverage

while reducing the purchase and operation cost. Additional benefits follow as low-cost

sensor networks develop in the future, including democratizing air quality monitoring and

promoting public health risk assessment.

A growing number of low-cost air sensors are commercialized for air quality

measurement. Different ways of segmenting the large pool of available commercial

sensors exist, including by targeted air pollutants and operation principles. In the scope of

this dissertation, electrochemical sensors and metal oxide sensors for trace level gas

phase air pollutants were selected for evaluation and field application.

(a)

Gas diffusion barrier

Working electrode

Wetting filter

Reference electrode

Wetting filter

Counter electrode

Wetting filter

Electrolyte

(b)

Target analyte

O^{2-} O^{2-} O^{2-} O^{2-}

Electrode   Sensing layer   Electrode

Dielectric substrate with heater
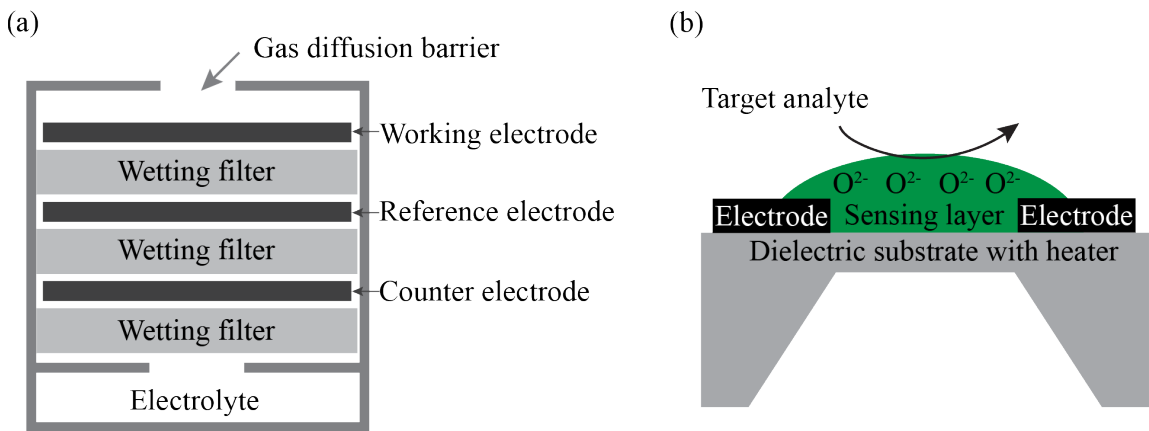
Figure 1-2. Operation principles of (a) electrochemical sensors and (b) metal oxide sensors. Figures are adapted from Figure 1 in Mead et al, 2013 and Figure 9 from Korotcenkov et al, 2017.

Electrochemical gas sensors provide quantitative measurement for different

chemicals based on the electron transfer from electrode to electrolyte (Figure 1-2a). The

targeted gas analytes reach the electrode through diffusion and then go through

electrochemical reactions. The so-produced current is proportional to the gas

concentration and is used for quantification. Electrochemical sensors face certain technical challenges that hinder the accurate quantification results, including non-selective response to other atmospheric compounds, sensitivity to changing environmental conditions, and long-term stability issues (Mead et al. 2013). Despite the challenges, many studies have been carried out to assess the potential of deploying electrochemical sensors in the ambient air quality monitoring. As an example, commercial electrochemical sensors were evaluated for measuring sulfur dioxide (SO_2) on the island of Hawaii, where the concentration of SO_2 is relatively high with few interferents (Hagan et al. 2018).

The response of metal oxide sensors is based on altered resistivity during the surface chemical reaction (Figure 1-2b). In the absence of competitive adsorbates, molecular oxygen from air splits into adatoms on the surface of metal oxides, leading to an electron-depletion layer at the surface. Electric resistivity changes when the sensor is exposed to air laden with organic analytes. A catalyzed chemical reaction takes place between the oxygen adatoms and organic analytes, and electrons are injected into the depletion layer. Metal oxide sensors face similar challenges as electrochemical sensors in terms of sensitivity, selectivity and stability, but are found to have a wider range of sensitivity to volatile organic compounds than electrochemical sensors (Spinelle et al. 2015). There are also more studies focusing on engineering the nanostructure and composition of metal oxides to improve their sensing performance. For example, nanostructured Ti-doped ZnO particles produced by flame spray pyrolysis were found to be selective to isoprene at concentration levels as low as 5 ppb (Güntner et al. 2016).

In real-world applications, different types of sensors are usually assembled in an

integrated system for long-term measurement to provide a comprehensive understanding of multiple pollutants (Jiao et al. 2016, Liu et al. 2020). Relative humidity and temperature are typically measured for correction or calibration purposes.

1.2.2   UAV measurement

Broad capabilities of unmanned aerial vehicles (UAVs) have made possible their many applications in commercial and consumer market in the past decade. In the field of atmospheric studies, UAVs are deployed as platforms for mobile chemical sensing. Among different types of UAVs, rotary-wing UAVs are specifically suitable for airborne measurements within the lower boundary layer due to their excellent maneuverability (Villa et al. 2016). They can be utilized in various situations, including forest canopies, water surface, and even indoor environment (Burgués and Marco 2020). Together with the benefits of flexibility comes the limitation of payload capacity and endurance. Such limitation requires the onboard measurement system to be light-weight and fast-response. UAVs with proper lightweight sensor payloads can be utilized for in-situ pollutant measurement within an intermediate range at around 1-m resolution vertically and horizontally (Stewart and Martin 2020). The range and the resolution made possible by UAVs fill the gap of atmospheric measurement platforms (Figure 1-3).
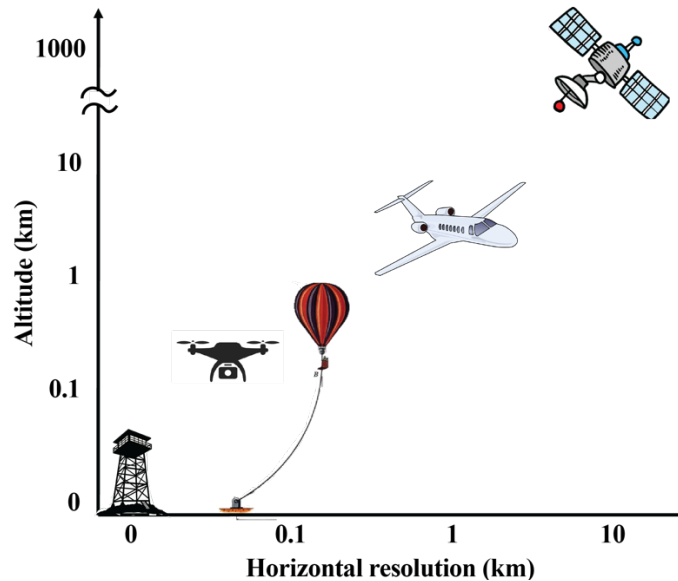
Figure 1-3. Overview of different atmospheric measurement platforms.

Atmospheric measurements using UAVs with onboard miniature systems have been reported in several studies conducted by our group. A sampler for VOCs was built around adsorbent cartridges, which can then be analyzed using gas chromatography-mass spectrometry (GC-MS) to provide VOC identification and quantification (McKinney et al. 2019). The sampler was deployed in several field studies to measure the horizontal heterogeneity of BVOCs in the near-canopy atmosphere over tropical forests (Batista et al. 2019, Ye et al. 2021). Commercial sensors, such as DustTrak™ II Aerosol Monitor and Personal Ozone Monitor, were also explored for UAV onboard measurement to collect vertical profiles of particulate matter and ozone in the atmospheric boundary layer (Guimarães et al. 2019, Liu et al. 2020). Various applications of UAVs are reported beyond atmospheric measurements in the tropical forest context, including pollutant source monitoring and plume tracking (Stewart and Martin 2020). Besides the promising applications, there are complications involved in UAV measurement that should be carefully considered for accurate interpretation of the results. Numerical modelling can

simulate the impact of UAV-induced turbulence and advise UAV sampling protocols (Ma et al. 2021).

1.3   River winds in the tropical forest

Thermal difference on the hot land and cool water bodies, if strong enough, can induce local air circulations (Figure 1-4). Sea breeze and urban heat island effect are both good examples for such circulations, which are well documented and studied in multiple regions (Simpson 1994). The Amazon has the largest drainage system in the world and the width of the Amazon River can vary from 10 km in the dry season to over 40 km in some locations in the wet season. Huge river water bodies drive strong local circulations, such as river winds. River winds are wind patterns caused by thermal difference on the hot land and cool water. During the day, hot air arises from the land and descends over the water. Horizontal wind moves accordingly to close the cell, i.e. from river to land at surface and vice versa at higher altitude. During the night, the situation is reversed and air movement in the opposite direction is expected.
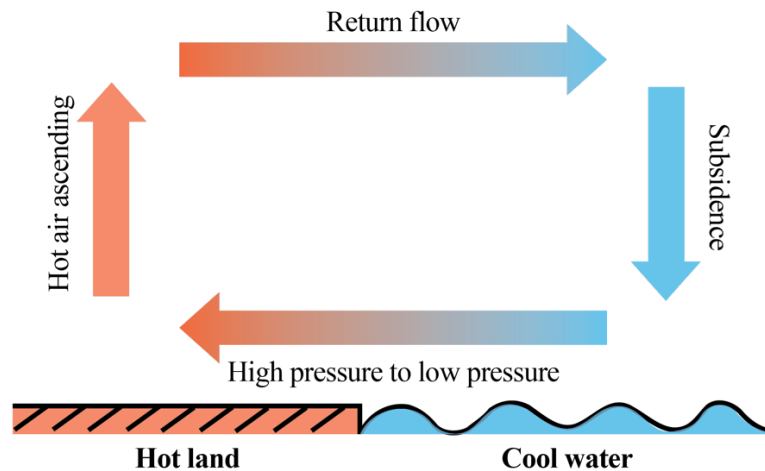
Figure 1-4. Schematic view of river winds development

River winds can be observed directly from wind measurement along the riverbank

when conditions permit. Radiosondes, typically carried by weather balloons, are
commonly used for collecting vertical profiles of meteorological data and provide direct
evidence for river winds (Dias et al. 2004). Other indicators of local circulations can be
inferred from satellite observations such as precipitation patterns (Paiva et al. 2011). The
development and impact of local circulations are also studied in high-resolution models
and validated with surface weather observations (Lu et al. 2005). In-situ measurement at
higher spatial and temporal resolution is preferred for more accurate understanding, but it
was not possible using traditional measurement tools.

River winds were found to alternate precipitation in the riparian regions from
observations and modelling studies. de Souza et al identified the correlation between the
growth of urban area in Manaus city and the increase in precipitation through simulations
in Brazilian Developments on the Regional Atmospheric Modeling System (BRAMS)
model (de Souza et al. 2016). Satellite observations from Tropical Rainfall Measurement
Mission (TRMM) revealed the pattern of lower precipitation over large water bodies in
the Amazon region (Paiva et al. 2011). Similar precipitation patterns were observed in
long-term surface weather station dataset (Dos Santos et al. 2014).

Besides the water vapor, river winds can circulate air pollutants and thus have
substantial impacts on riparian air quality and human health. The extent of such
circulation depends on the strength of river winds and the extrapolation of riparian
measurements of chemical concentrations to a larger scale should be considered
cautiously. Riparian regions in the Amazon basin are home to many human settlements
and the impact of river winds on air quality can be translated to human health impacts.

The strength of river winds depends on several factors and numerical modelling has

been widely used to study the relationship between characteristics of river winds and the controlling geophysical variables (Crosman and Horel 2010). Among different variables, thermal contrast and synoptic scale wind field are two most important ones. Thermal contrast between the land and the water body, which is affected by insolation and land cover, provides the driving force for river winds. Thermally driven circulations like river winds are usually very weak and can be overwhelmed by the synoptic scale winds (Crosman and Horel 2010). Detailed observational evidence is lacking for better understanding of river winds development.

1.4 Motivation and organization of this thesis

Amazon basin plays an important role in regulating hydrological cycles, energy balance and air quality at regional and global scales. Human activities such as deforestation and urbanization can alter the atmospheric processes to different extents. Novel technologies like low-cost sensors and UAVs open a new horizon for high temporal and spatial resolution measurement and fill the gap of the current quantitative suite in atmospheric science. River wind is an interesting yet poorly quantified phenomenon and understanding of river winds greatly benefits from the new capabilities. In-situ measurement of meteorological and chemical vertical profiles within a few hundred meters provides direct evidence to study the development and impact of river winds.

The studies presented in this thesis aim to explore the atmospheric application of novel technologies in the challenging tropical regions. Commercial sensors were evaluated in atmospheric relevant conditions and modifications were implemented to enhance the selectivity towards target analytes (Chapter 2). Charms and challenges of

commercial sensors for chemical detection at trace level concentrations were explored in

laboratory conditions. Commercial sensors for both meteorological and chemical

measurement were assembled on UAVs and deployed to collect vertical profiles over the

river surface near Manaus city in central Amazonia (Chapter 3). The linkage between the

development of river winds and meteorological conditions was revealed through

clustering analysis. The impact of river winds on chemical transport was observed in

vertical profiles of chemicals and was further simulated in Large Eddy Simulations

(Chapter 4). The impact of river winds on riverbank tower measurement was also studied

from simulation experiments. Chapter 5 summarizes the major results in this dissertation

and provides outlook for related studies.

2 Selectivity For Metal Oxide Sensing of Biogenic Volatile Organic Compounds

2.1 Introduction

Biogenic volatile organic compounds (BVOCs) emitted from terrestrial vegetation contribute in vast quantities to the atmospheric burden of gaseous organic compounds (Guenther et al. 2006). Emitted BVOCs can vary widely across different vegetation types and environmental conditions (Kesselmeier and Staudt 1999). Variations in emission and atmospheric chemistry can have significant effects on air quality and global climate (Pierce et al. 1998, Bates and Jacob 2019). Ecosystem change and stress can also occur. Among hundreds of BVOC species, the five-carbon compound isoprene contributes to about half of the annual global emissions of non-methane hydrocarbons, followed by ten-carbon monoterpenes (15%). Accurate quantification of the emissions of major BVOC species is important for understanding the impacts of BVOCs on the biosphere-atmosphere-climate system (Guenther et al. 1995, Guenther et al. 2006, Guenther et al. 2012).

With the advance of microfabrication technology and materials science, compact low-cost sensors open a new horizon of distributed monitoring in atmospheric measurement. Currently employed VOC measurement systems include proton-transfer-reaction mass spectrometry (PTR-MS), gas chromatography-mass spectrometry (GC-MS), and chemical ionization mass spectrometry (CIMS). Mass spectrometry provides detailed information about chemical composition in real-time but faces challenges in spatial resolution because of its expense and size. Measurements of atmospheric trace gases, such as CO_2, CO, NO_x, ozone, and volatile organic compounds (VOCs), have been explored using low-cost sensors (Spinelle et al. 2017, Zanni et al. 2018). Sensors of different operational principles, including photoionization detectors (PID), metal oxide semiconductors (MOS), and electrochemical sensors, provide a wide range of sub-ppb to ppm detection and quantification of VOCs at 1 atm and 20 °C. Among these approaches, PID and MOS can detect VOCs at ppb concentrations and hold promise for meeting the requirements of atmospheric BVOC measurements (Williams et al. 2015).

Metal oxides, when operated at high temperatures in air, create a surface layer of chemisorbed oxygen species in ionic form and an electron-depleted region. The reactions between the oxygen species and the adsorbed VOCs on the surface lead to a change in resistance of the sensor. The change is proportional to the concentration of VOCs, and it can be used for species quantification. VOC sensing using metal oxide sensors has been studied for prevalent chemical compounds, such as ethanol and acetone at ppm concentrations (Mirzaei et al. 2016, Lin et al. 2019). The sensitivity of MOS sensors can be further improved to ppb level detection by adjusting the chemical composition and the nanostructure (Elmi et al. 2008, Güntner et al. 2016, Li et al. 2016, Zhang et al. 2018).

14

A complication in mixed atmospheric systems is that MOS sensors are weakly selective, and there is cross sensitivity to multiple species. Species-specific detection, which is crucial to constraining emission inventories of different VOCs, remains lacking. Different approaches have been explored to improve the selectivity for VOC sensing, including pre-separation and in-situ selective response. Indoor air pollutants like benzene, toluene, and m-xylene have been studied by use of a pre-separation column of the chromatographic type (Zampolli et al. 2005, Zampolli et al. 2009, Garg et al. 2015). Activated alumina packed-bed filters can retain hydrophilic species for short times (5 min) while letting VOCs pass through (Van Den Broek et al. 2018). Selective sensing by modulating the metal oxide composition and operation temperature has also been studied (Kanan et al. 2009, Leidinger et al. 2014). Specifically, Ti-doped ZnO was more sensitive to isoprene compared with acetone, methanol, and other oxygenated species (Güntner et al. 2016).

In this context, pre-separation by a gas separation membrane shows the potential for VOC selectivity by molecular size (Wang et al. 2020). When a concentration difference is present on two sides of the membrane, molecules tend to flow from high to low concentration. Permeability, which affects the flow rate, depends on thermodynamic partitioning of species from feed phase to membrane phase and kinetic diffusion within the membrane (Bernardo et al. 2009).

Mixed matrix membranes are promising regarding possibilities for selective permeability. They combine polymeric and microporous inorganic materials to obtain good performance for gas separation and mechanical properties (Chung et al. 2007). Traditional polymer membranes often have good mechanical strength but face a trade-off

between permeability and selectivity (Robeson 2008). Micro-porous materials of precisely defined pore structure, such as metal organic frameworks, improve selectivity when embedded in the polymer matrix (Zhao et al. 2018). Mixed matrix membranes have been studied for air, hydrogen, CO_2, and hydrocarbon separations (Tantekin-Ersolmaz et al. 2001, Fang et al. 2015). Application for C_5 and C_{10} hydrocarbon separations at ppb concentrations typical of atmospheric conditions is unexplored.

This chapter focuses on use of metal oxide semiconductors for the detection and quantification of BVOCs for ppb concentration at 1 atm and 20 °C. The sensitivity and stability of metal oxide semiconductors are evaluated for prevalent BVOC species (i.e., isoprene) under realistic environmental conditions. Selectivity was evaluated for standalone MOS sensors as well as for upstream use of mixed matrix membranes at ambient atmospheric pressure.

2.2   Experimental

2.2.1   Sensor system

Figure 2-1 shows a picture of the sensor system, including the electronic circuits and flow chambers for sensors. Commercial metal oxide sensors (Alphasense, VOC *p*-type metal oxide sensors) were used. The sensors were operated in a temperature cycle between 400 °C and 525 °C by supplying a square wave of voltage to the substrate-mounted Pt-heaters (Alphasense 2021). Eight sensors were mounted and housed in individual chambers. Each chamber had an inlet and outlet, and the chambers could be connected in series or parallel.

For selectivity tests, the membrane was attached to a brass disk that had a concentric hole (Figure 2-1). It was sealed by impermeable epoxy glue (Devcon, 5

Minute Epoxy, 14250). Gas flows of the analyte species passed on the front side of the membrane, and the analyte concentration on the back side was monitored by the MOS sensor system. The system was assembled in a parallel configuration so that redundant measurements across the individual sensors were made.
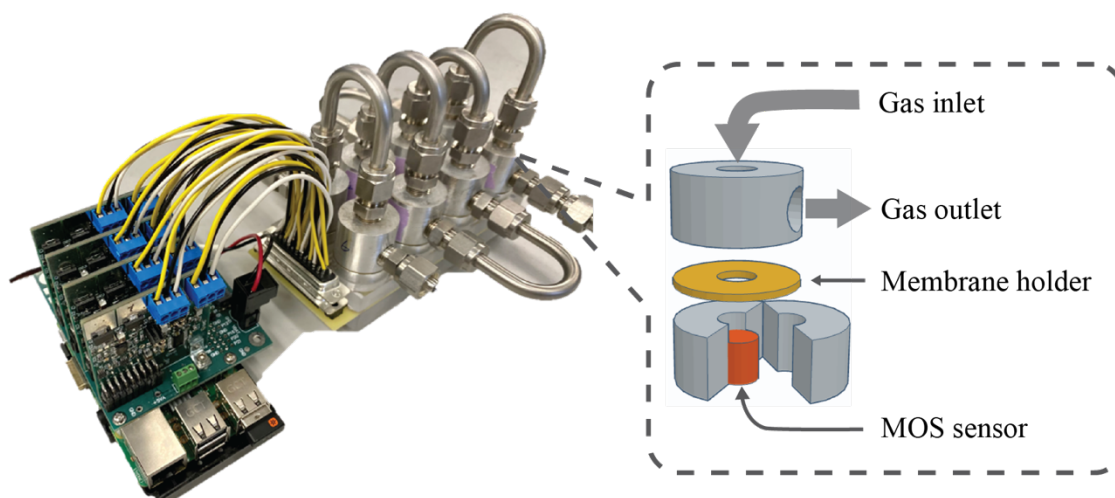
Figure 2-1. Photograph of the sensor system.

The electronic circuits to power the sensors were home built for optimizing a combination of response time, operation temperature, and signal quality. The sensors were programmed and controlled through a micro-controller (*Raspberry Pi*), including temperature cycling.

The performance of metal oxide sensors depends strongly on the operating temperature, especially when using two-temperature pulsing approach. The as-recommended operation temperature, however, is not optimized towards isoprene detection. Here, different operation temperatures in a range from 250 to 450 °C were explored for the best performance. The detection limit, defined as 3 times of the background noise in ultra-pure air, was selected as the benchmarking parameter. The

results for isoprene and α-pinene are shown in Figure 2-2. As the temperature increases from 250 to 350 °C, both the signal and the noise decrease but the detection limit improved. There was no significant difference in performance above 350 °C.
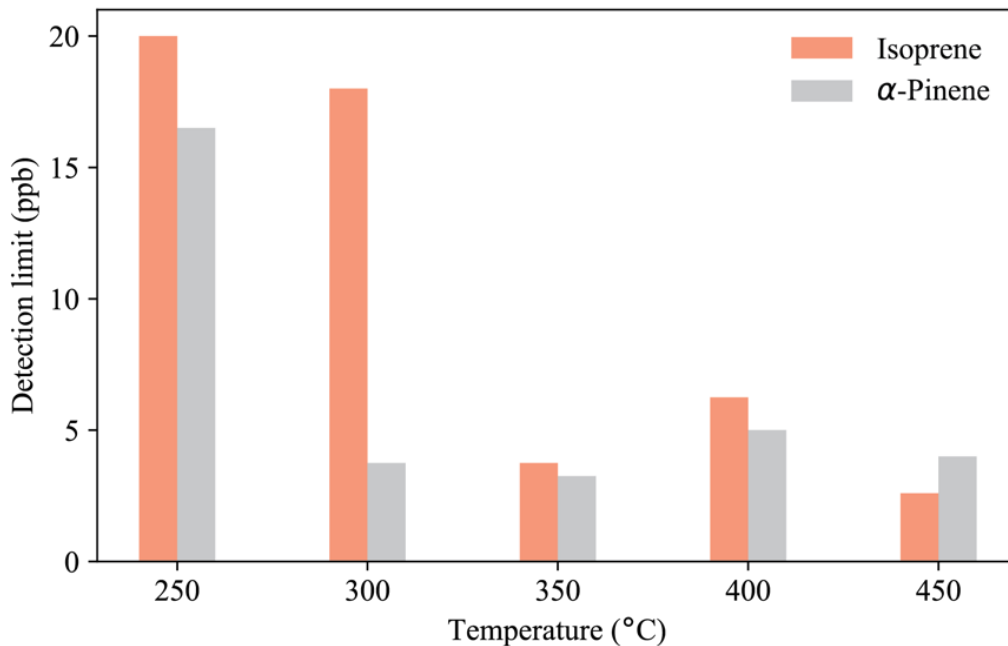
Figure 2-2. Detection limit as a function of sensor operation temperature for isoprene and α-pinene. The detection limit was calculated from three times of the noise in pure air.

Fast-changing BVOC concentrations indicate a requirement for real-time measurements. The time resolution preset by Alphasense electronic circuit is 6 min (300-s measurement and 60-s "reset"). The possibility of improving the time resolution was explored. Calibrations were conducted with the same sensor under different time cycles. The linear relationship persists for operation at one-minute time resolution (40-s measurement and 20-s "reset"). Therefore, the rest of the study adopted the one-minute time resolution for sensor evaluation.

The sensor system was evaluated for sensitivity and stability for detection and quantification of isoprene. A flow of known gas concentration was achieved by mixing higher concentration VOCs (1 ppm isoprene in pure nitrogen, Apel Riemer, Broomfield, CO) with ultra-pure synthetic air (Airgas) (Figure 2-3). Mass flow controllers were automated through *Labview*. The room temperature was 20 °C. Experiments were conducted for flows of pure isoprene from 1 to 100 ppb. Stability was evaluated by daily calibration with isoprene for seven consecutive days.
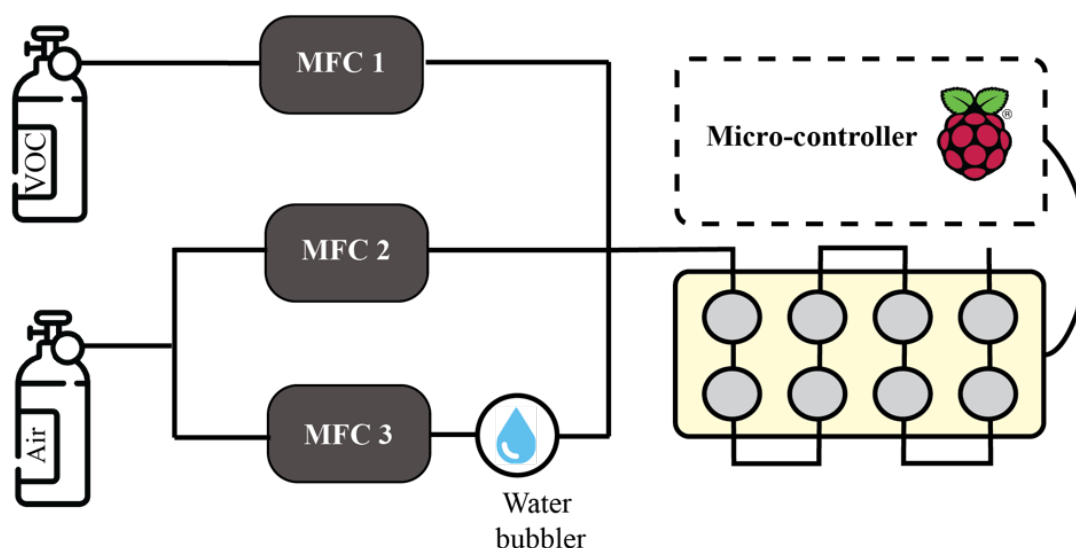
Figure 2-3. Schematic diagram of gas flow setup for sensor evaluation

2.2.2   Preparation and characterization of mixed matrix membranes

Mixed matrix membranes were prepared by the method of Chi et al (Chi et al. 2019). To prepare HKUST-1 nanoparticles, precursor solutions were first prepared separately. The copper precursor solution was prepared by dissolving copper nitrate trihydrate (0.9 g, 3.7 mmol) in methanol (100 mL). The organic ligand solution was prepared by dissolving trimesic acid (0.43 g, 2 mmol) in methanol (100 mL). The two separate solutions were mixed, and sodium acetate (0.0492 g, 0.6 mmol) was added as a

modulator to tailor the morphology and size of HKUST-1 crystals. The mixture was vigorously stirred at room temperature for 1 h. This MOF suspension was washed three times to remove the residual precursors. Each washing step proceeded by centrifuging the MOF suspension, removing supernatant, and dispersing the MOF nanoparticles in fresh methanol.

To prepare mixed matrix membranes (MMM), MOF nanoparticles were then transferred from methanol to tetrahydrofuran (THF) by three similar centrifugation and washing steps. Each step added fresh THF. To determine the concentration of HKUST-1 in the stock suspension, a small volume (0.5 mL) of the HKUST-1 suspension in THF was evaporated in a pre-weighed vial in a vacuum oven. The vial with dried HKUST-1 particles was weighed again to calculate the appropriate concentration of HKUST-1 suspension. For the targeted weight loading (10%, 20%, or 30%) of MMM, the polymer weight was then calculated to achieve the total mass of 0.1 g. The mass of 0.1 g was used for best membrane casting result. Membrane thickness was controlled by changing the total material mass (0.05 g, 0.1g, 0.2g) used for casting the membrane during the process of solvent evaporation. The calculated weight of the 6FDA-DAM polymer was dissolved in THF and stirred for 3 h to achieve good mixing. The MOF suspension in THF was then added, stirred, and horn-sonicated to prevent agglomeration. It was poured onto a glass petri dish covered by an aluminum foil cap with holes and cast in an oven at 50 °C overnight. The membrane was then detached from the petri dish and dried in a vacuum oven to remove the residual solvent. The membranes were activated at 150 °C in situ under dynamic vacuum for 2 h in the oven. After activation, the membrane remained at

room temperature to cool down overnight. Transmission electron microscope (TEM) images were obtained using a FEI Tecnai (G2 Spirit TWIN) operating at 120 kV.

2.3   Results and discussion

2.3.1   Sensitivity

Metal oxide sensors were operated by two-temperature pulsing, which is an approach that improves the sensitivity and stability (Alphasense 2021). Two-temperature pulsing raised the temperature from 400 °C to 525 °C for regeneration and then returned it to 400 °C for measurement, as shown in Figure 2-4a. The sensors were exposed to isoprene concentrations from 1 to 10 ppb, which is representative of typical atmospheric concentrations. The concentration in each step was calculated from the dilution ratio in the gas flow setup (Figure 2-4b). The corresponding sensor responses are shown in Figure 2-4c. The sensor resistance R_g was recorded in the presence of target analyte. The sensor resistance R_0 was recorded when exposed only to pure air. The sensor response ξ, defined as $\xi = R_g/R_0 - 1$, for the fractional change in resistance is used, herein, for comparison across different sensors and different operating conditions.

(a)

(b)

(c)
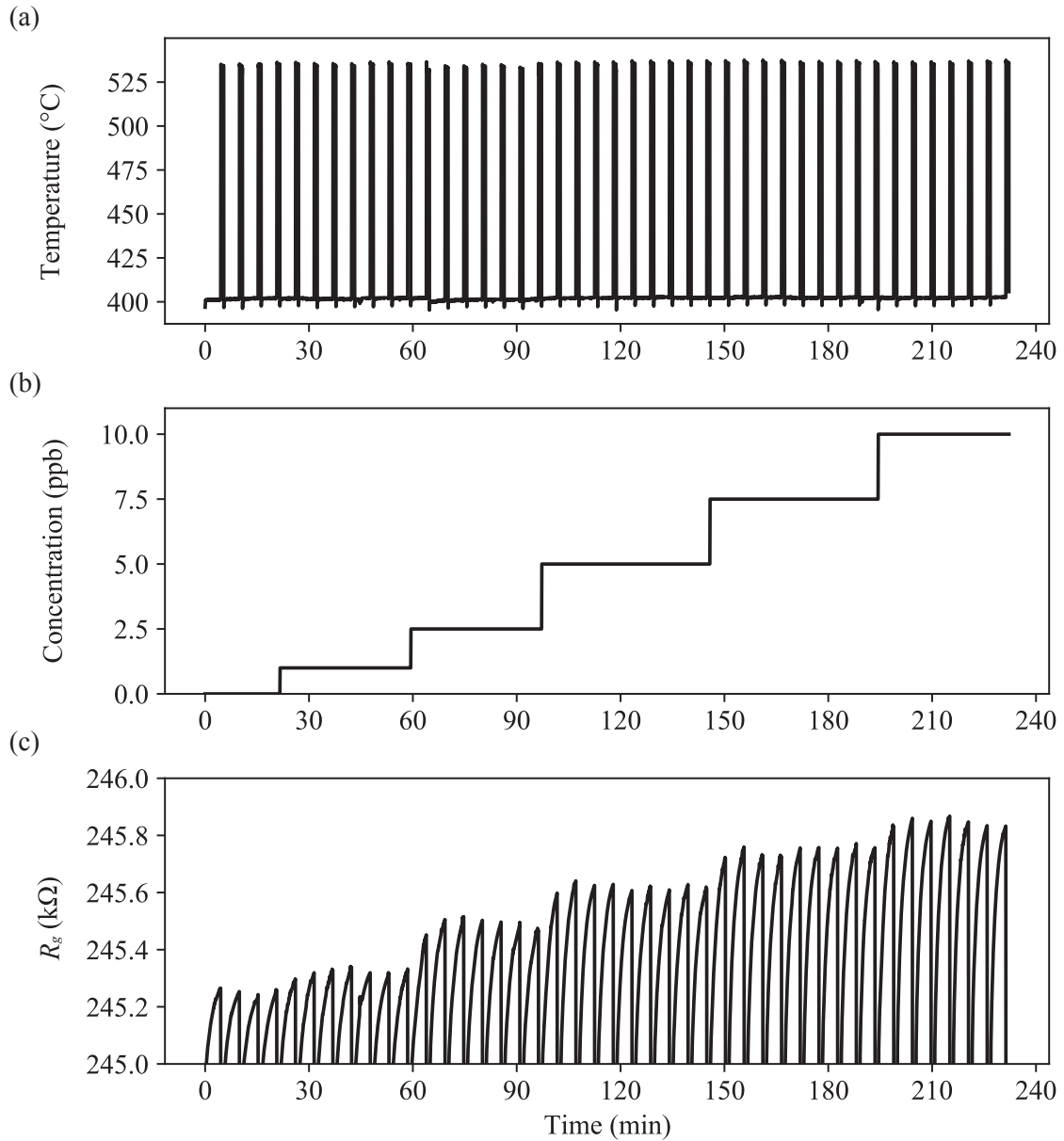
Figure 2-4. Examples of sensor control and response. (a) Temperature pulsing profiles. (b) Change of flow concentration over time. (c) Sensor response to the flow concentration change. The temperature was converted from the platinum heater resistance.

The sensor response was linear with concentration within the studied range (Figure 2-5). The slope of the calibration is denoted by m. The signal noise when exposed

to pure air was equivalent to 0.5 ppb for one-hour averaging. The detection limit, defined

as three times the signal noise, was 1.5 ppb.
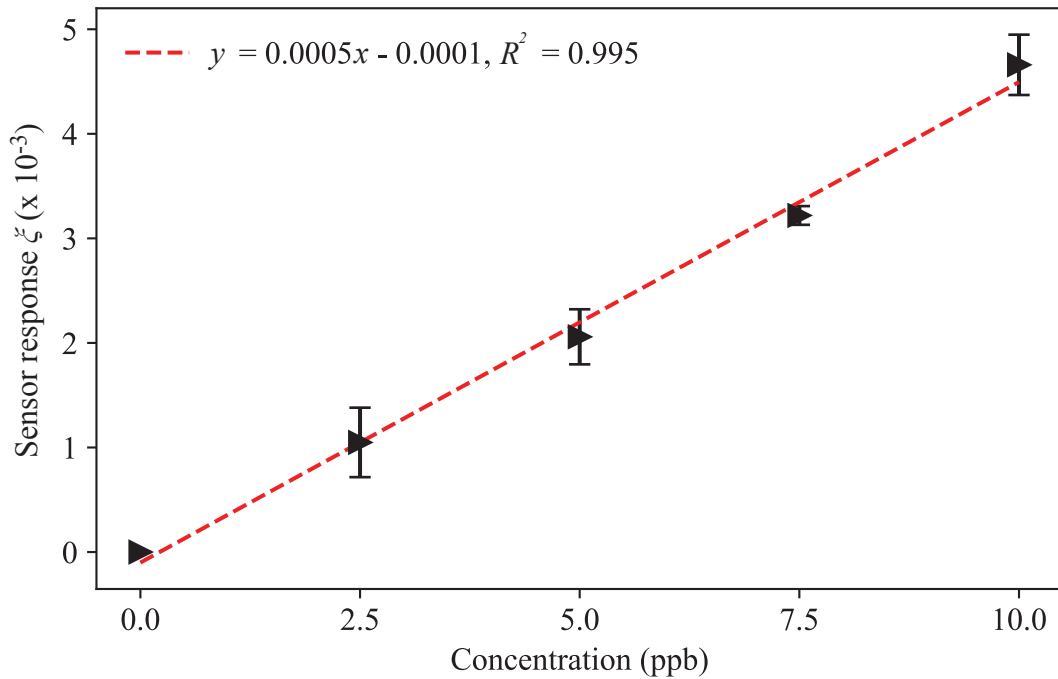
Figure 2-5. Sensor response to isoprene up to 10 ppb.

2.3.2 Stability

Drift in the response of MOS sensors is linked to multiple factors of structure

transformation and contact degradation (Korotcenkov and Cho 2011). The sensor

response ξ is typically more stable for quantification. Consecutive calibrations were

conducted across seven days to evaluate sensor stability (Figure 2-6).
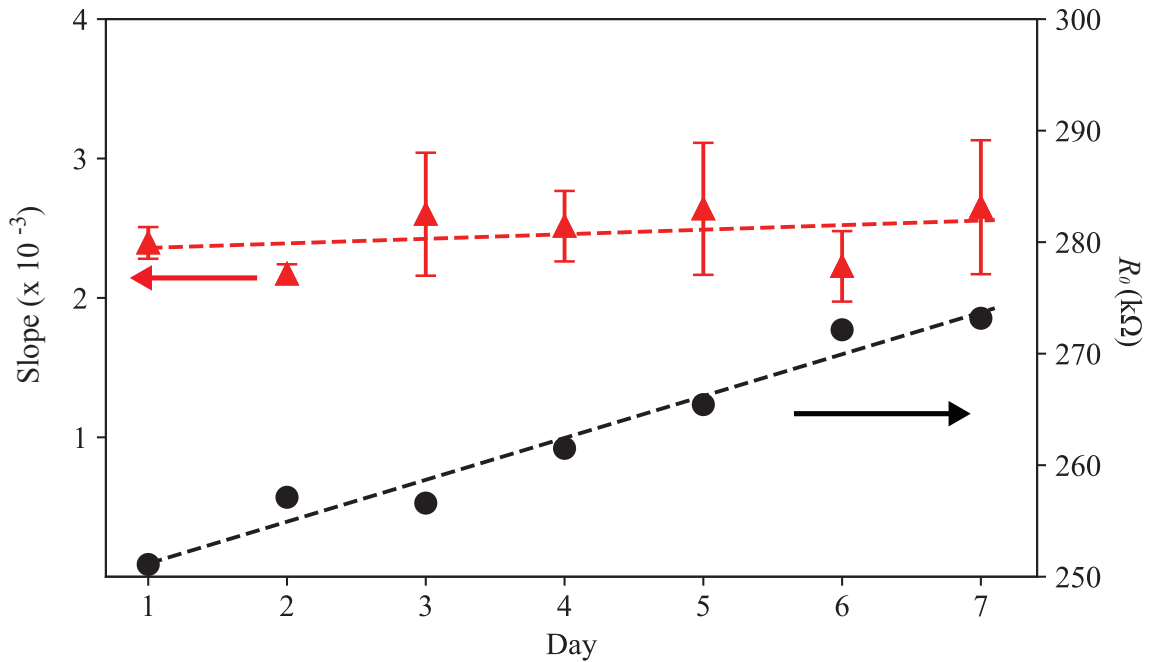
Figure 2-6. Sensor stability across one week. Stability is represented by slope m of linear calibration equation and the resistance R_0 when exposed to pure air on each day.

Over the course of seven days, R_0 increased by 8%. The slope m of the calibration did not vary. Results indicate that a calibration for sensor response holds for seven days within 10% accuracy in dry air. More accurate quantification requires more frequent calibration.

2.3.3   Humidity

In a humid environment, water adsorbs to the MOS surface. In consequence, the surface adsorption of analytes, their surface catalytic reactions, and the electronic properties of the metal oxide semiconductors can all be affected (Korotcenkov and Cho 2011). The sensor response change induced by 80% relative humidity at 20 °C amounts for 276 ppb isoprene according to the calibration under dry air conditions (Figure 2-7).
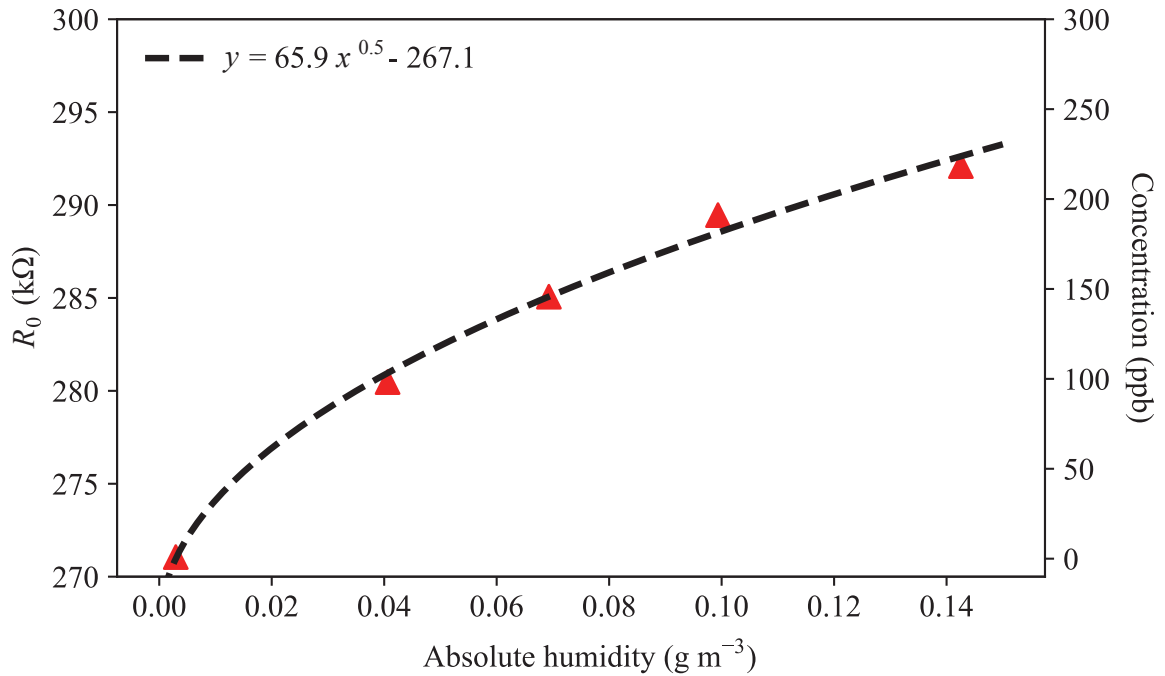
Figure 2-7. Changes of R_0 under different humidity conditions and the corresponding concentration change of isoprene calculated by the calibration curve as shown in Figure 2-5.

Correction for humidity in the calibration is crucial for accurate quantification to integrate humidity into calibration. The calibrations conducted at different humidity conditions are plotted in Figure 2-8. Linear relationships hold for sensor response ξ under different humidity conditions with minor changes in the parameters. Qualitatively speaking, the sensor becomes more sensitive as relative humidity increases. The difference is only visible over large changes on relative humidity under room temperature.
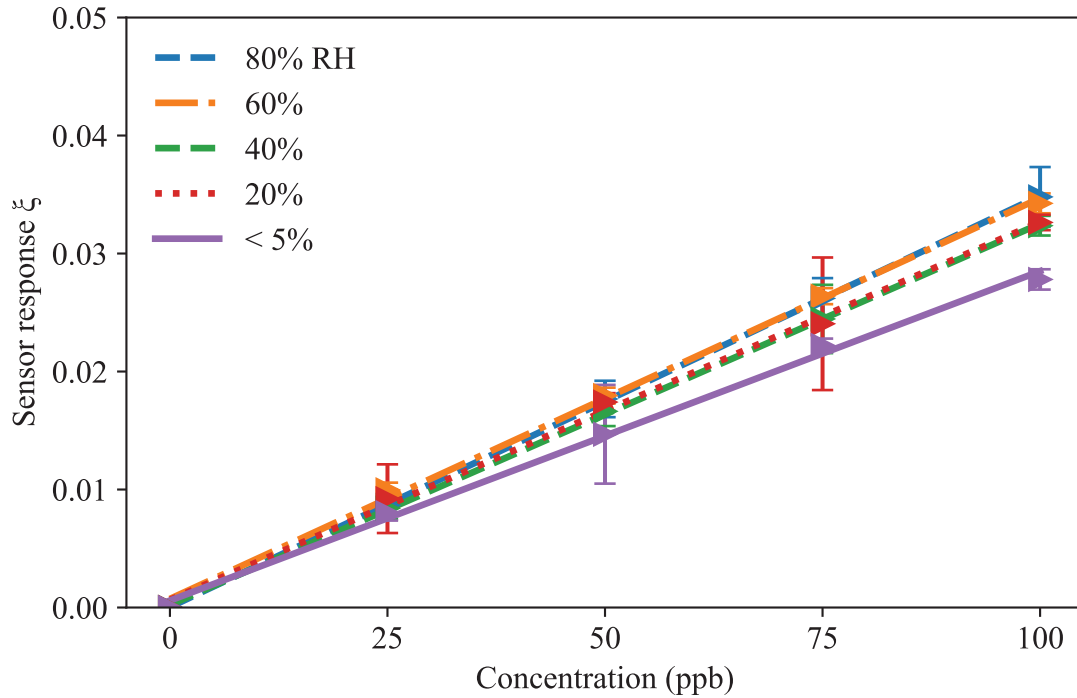
Figure 2-8. Sensor calibrations under different relative humidity conditions.

The two important parameters in obtaining calibration curve for sensor response ξ are R_0 and slope m, which can be fit against absolute humidity ρ_v using the following equations (Figure 2-9):

$$\Delta R_0 = a \rho_v{}^b + c \qquad (2\text{-}1)$$

$$\Delta m = a_1 \rho_v + b_1 \qquad (2\text{-}2)$$

The impact of water vapors can be considered as twofold: (1) interaction with surfaced adsorbed oxygen and (2) direct release of electrons by OH groups (Yan et al. 2021). The power law fitting of R_0 accounts for the change induced by the surface interaction. The linear relationship of m quantifies the increased sensitivity due to direct reaction of chemisorbed water vapor with VOCs. The quantified relationship can then be integrated in the calibration function for future applications.
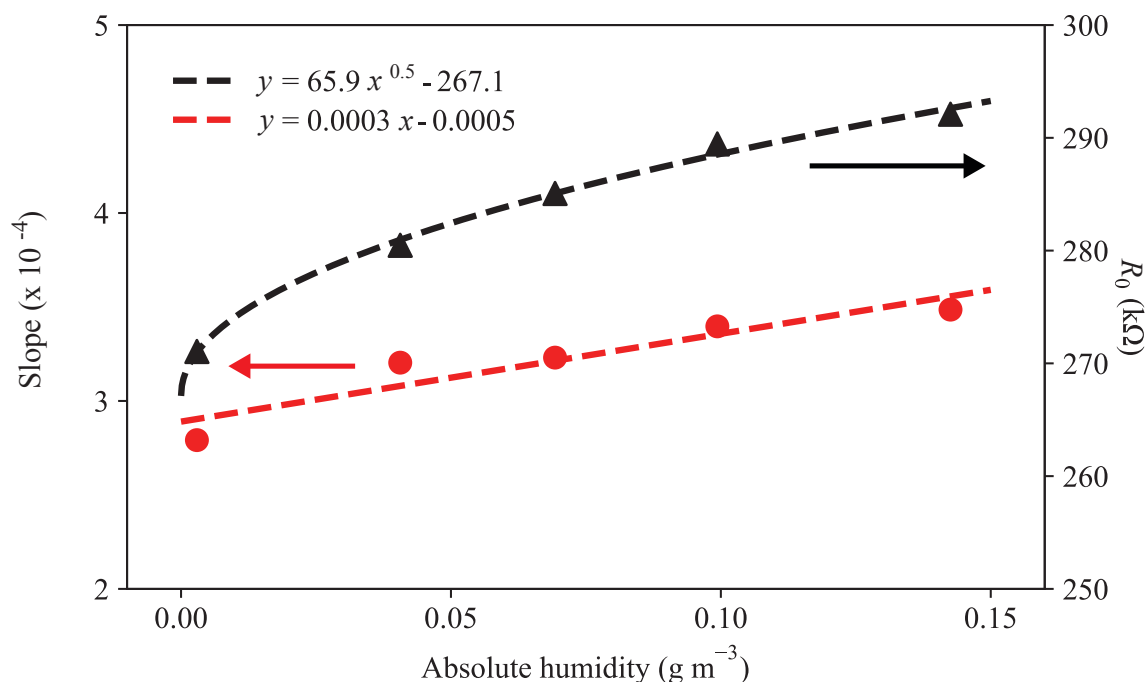
Figure 2-9. Slope of linear calibration equation and resistance R_0 when exposed to pure air for relative humidity conditions.

Besides humidity correction for baseline and parameters of calibration curves, stabilization of humidity level also provides an alternative for accurate quantification. Removing the water vapor with adsorption-type setup can be difficult for trace level volatile organic compounds. Traditional desiccants such as silica gel adsorb the target analytes at trace level when removing the water vapor. Materials with great adsorption capacity for water vapor but unknown adsorption capacity for VOCs, such as Nafion, should be carefully evaluated before application.

Condensing the water vapor, however, is promising for stabilizing the humidity in measurements of hydrophobic volatile organic compounds. Especially for application in the tropical forests, where the ambient air is very hot and humid, a cold trap can remove the excess water vapor and stabilize the humidity level for improve quantitative accuracy.

The efficiency of the cold trap should be evaluated thoroughly in various field conditions before application.

2.3.4 MOS selectivity without pre-separation

The comparison of the MOS sensor response to five species at 10 ppb is shown in Figure 2-10. Further information on each species is listed in Table 2-1. The sensor responded most strongly to isoprene and α-pinene. For a selective response factor defined as unity for isoprene, the response factors of α-pinene, acetone, methanol, and formaldehyde were 1.0, 0.7, 0.17, and 0.13, respectively.

Table 2-1. Formula, biogenic sources, estimated global emissions, and bimolecular rate constants with hydroxyl radicals.

Compound	Formula	Lathiere et al. (2006) [a] ($Tg\ C\ yr^{-1}$)	Sindelarova et al. (2014) [b] ($Tg\ C\ yr^{-1}$)	Bimolecular rate constant with hydroxyl radical [c] ($10^{12}\ cm^3\ mole^{-1}\ s^{-1}$)
Isoprene	$CH_2=C(CH_3)CH=CH_2$	460	594	101
α-Pinene	$C_{10}H_{16}$	117	95	53.7
Methanol	CH_3OH	106	130	0.944
Acetone	$CH_3\text{-}CO\text{-}CH_3$	42	37	0.219
Formaldehyde	$HCHO$	10	4.6	9.37

[a] Calculated global mean emissions from Lathiere et al.(2006) were for 1983–1995 using the global dynamic vegetation model Organizing Carbon and Hydrology in Dynamic EcosystEms (ORCHIDEE)(Lathière et al. 2006).

[b] Calculated global mean emissions from Sindelarova et al. (2014) were used for 1980–2010 using Model of Emissions of Gases and Aerosols from Nature (MEGAN 2.1) (Sindelarova et al. 2014).

[c] The bimolecular rate constant is listed for reaction with hydroxyl radical at 298 K (Seinfeld and Pandis 2016).

The similar selective responses of isoprene and α-pinene can be explained by the similar functional groups of each. They are both unsaturated hydrocarbons. The decreased response factors for the other tested VOCs can be attributed to differences in MOS surface catalytic reactions for these oxygenated species.
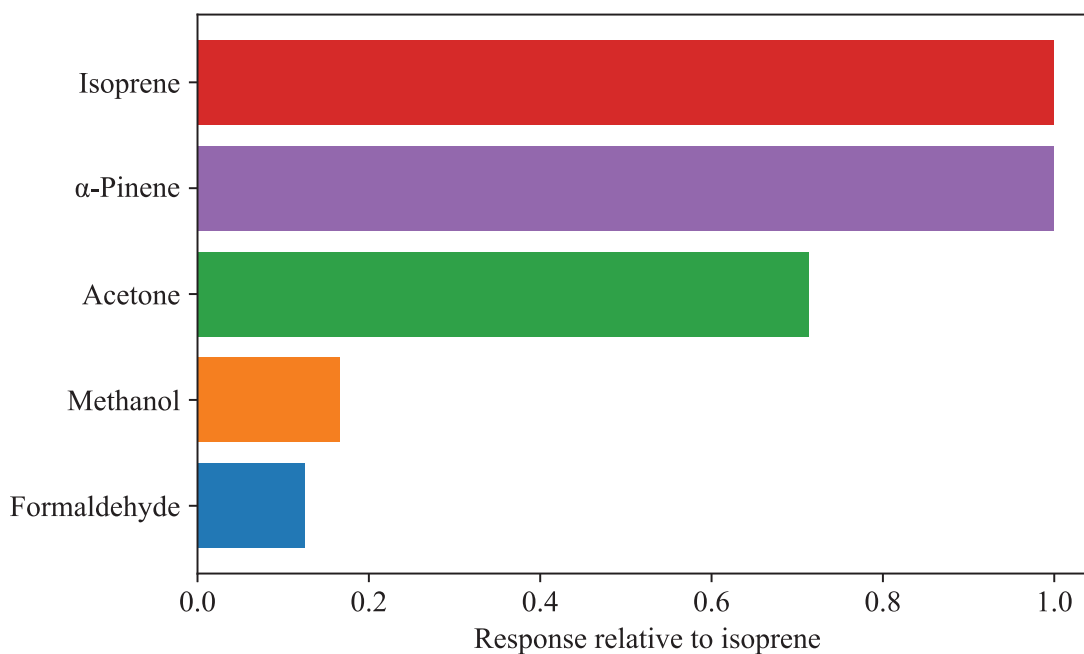
Figure 2-10. Relative sensor response to isoprene, α-pinene, methanol, acetone, and formaldehyde.

2.3.5   MOS selectivity with pre-separation using mixed matrix membrane

Up-stream separation using a mixed matrix membrane was implemented for

isoprene and α-pinene. Figure 2-11 presents the sensor response when separately exposed to isoprene and α-pinene in the presence and absence of the optimized mixed matrix membrane upstream. The optimized membrane is prepared using 0.1 g membrane material mass with 30 % branched MOF weight loading. Details about the membrane optimization are presented in Appendix A.

Without the membrane, the sensor response to isoprene and α-pinene was identical within measurement. For the membrane in place, the sensor response decreased to different extents between the two species. For a selective response factor defined as unity for isoprene in the membrane-MOS setup, the response factor to α-pinene was 0.13.
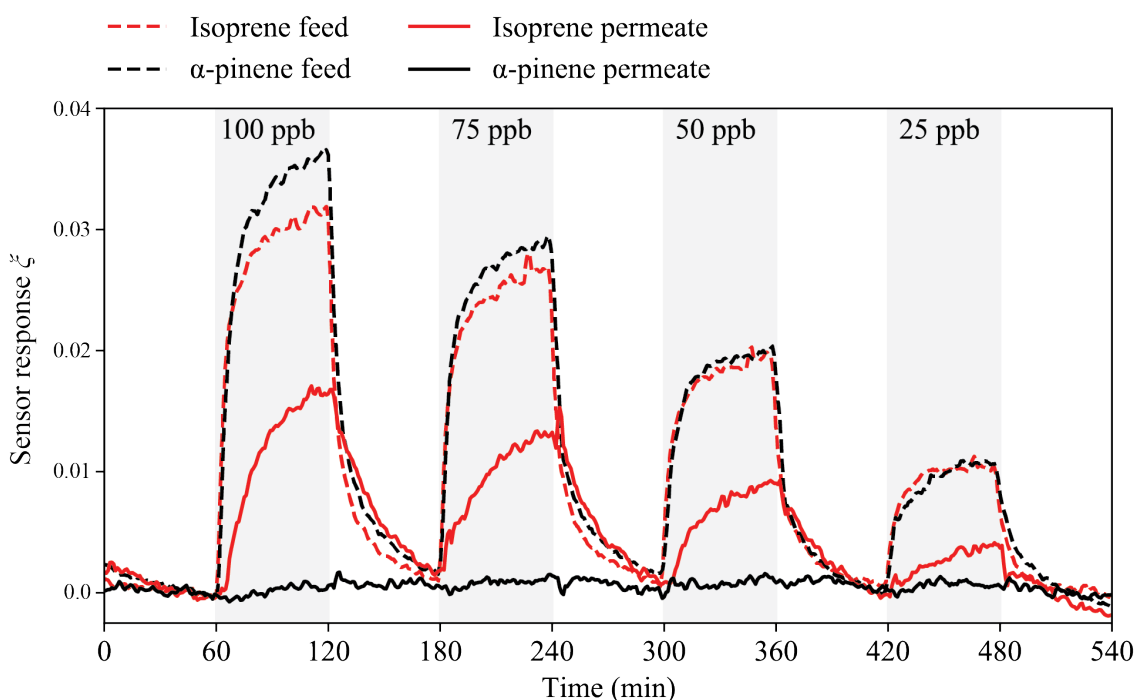
Figure 2-11. Performance of sensor system when exposed to flow of different analytes. The red and black lines represent the response to isoprene and α-pinene, respectively. The dashed and solid lines represent the response with and without the mixed matrix membrane, respectively. The white regions show periods when exposed to pure air.

For each concentration step of Figure 2-11, the condition was maintained for 1 h. The maximum sensor response ξ shows linear relationship to concentration changes (Figure 2-12). This result indicates that the separation performance of the mixed matrix membrane under the experimental conditions can be used for selective quantification of biogenic volatile organic compounds.
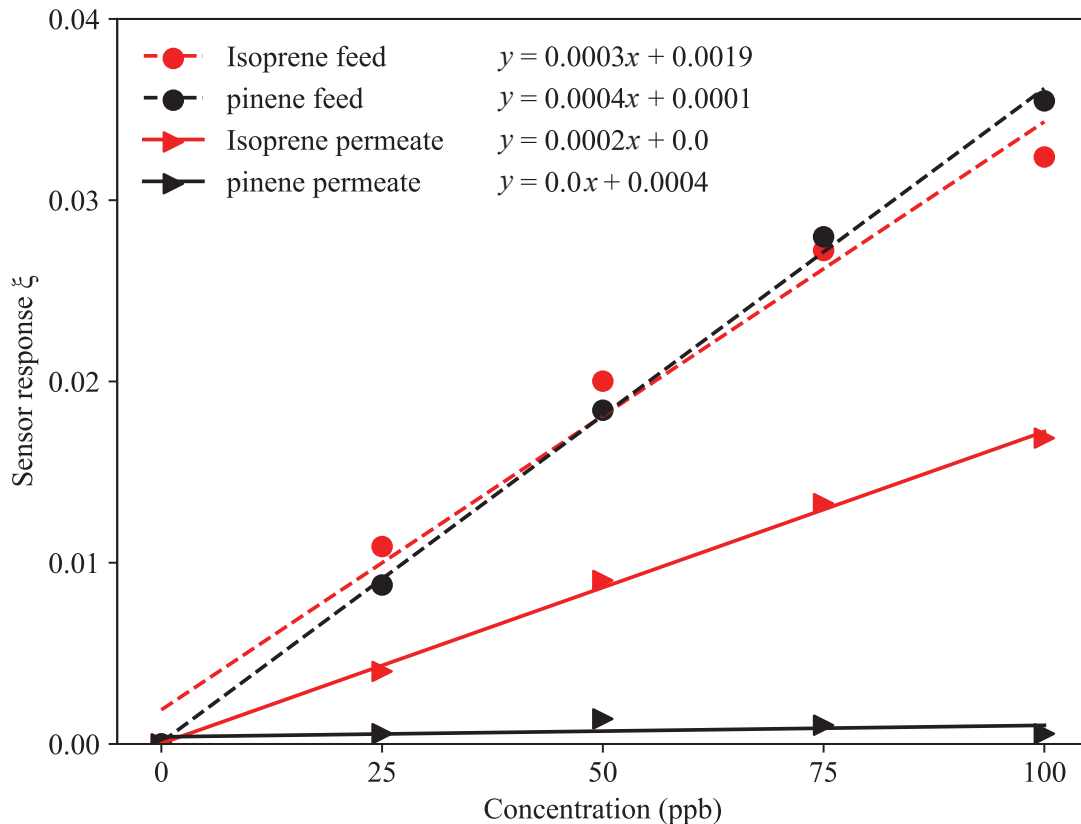
Figure 2-12. Linear regression for sensor responses under different conditions as presented in Figure 2-11.

2.4   Conclusion

Despite emission in large amounts, BVOCs are largely consumed by atmospheric oxidants, leading to ppb concentrations above the forest canopy (Atkinson and Arey 2003). Quantification of these concentrations requires high sensitivity and selectivity

towards the target species. This study designed and evaluated the potential of commercial metal oxide sensors as a detector for BVOCs and mixed matrix membrane as a pre-separation module for enhanced selectivity (Figure 2-13). The sensors were optimized to detect ppb-level isoprene, reaching a detection limit of 1.5 ppb. The sensor performance varied less than 10% over seven consecutive days. Calibrations of the sensor response ξ as a function of absolute humidity was achieved. Selectivity was obtained by adding a mixed matrix membrane upstream of the MOS sensor. In this MOS-membrane setup, discrimination between similar analytes, isoprene and α-pinene increased by a factor of 8, indicating the promising application for the pre-separation.
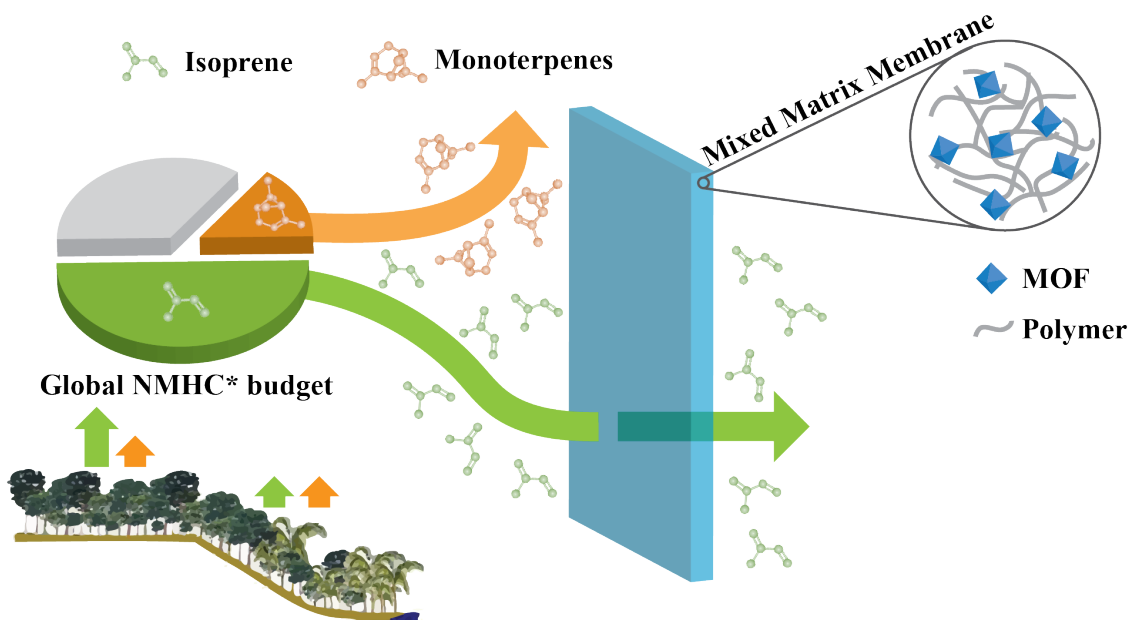
Figure 2-13. Overview of biogenic volatile organic compounds presented in this study and their separation using mixed matrix membranes. NMHC represents non-methane hydrocarbons.

The miniature sensing system studied here has the potential to be deployed on mobile platforms, such as unmanned aerial vehicles. This combination enables real-time measurement of BVOCs with great spatial coverage and fills the current gap for

quantification of important BVOC species. The species-specific information for BVOCs at low concentrations can facilitate the understanding their impact on the biosphere-atmosphere-climate system.

3 River winds and pollutant recirculation in central Amazonia: Observation

3.1 Introduction

Thermal contrast in a landscape of wide rivers and adjacent forest can induce important local atmospheric circulations that manifest as river winds (Simpson 1994, Miller et al. 2003, Crosman and Horel 2010). Wide rivers throughout Amazonia typically span 5 to 10 km. Under sunny skies, the daytime thermal difference between warm land and cool water contributes a local tendency for air to ascend over the warm land and to descend over the cool water. The resulting horizontal pressure gradients can drive air flow at surface elevation from the river to the land. In the absence of further complicating effects of local topography and other factors, such as frequent inclement weather during wet season and weakened thermal contrast under cloudy skies, a return wind from the land to the river can develop overhead at several hundred meters in altitude. In this way, closed recirculating sub-cells of river winds at the small mesoscale are possible. During the night, the system reverses. The land cools more rapidly than the river, and nighttime recirculation sub-cells are possible in the opposite directionality of the daytime

counterparts.

In Amazonia of northern Brazil, 11 million people live in the vicinity of wide rivers, corresponding to 39% of the total population in northern Brazil. The population was estimated using an Amazon GIS-based river basin framework (Venticinque et al. 2016) and data from the Brazilian National Water Agency (ANA 2021). The river and population centers are plotted in Figure 3-1. A distance of 10 km from a major river was selected as a threshold and 161 cities across nine Brazilian states was included. City populations were obtained from the data of the Brazilian Institute of Geography and Statistics (IBGE 2021).
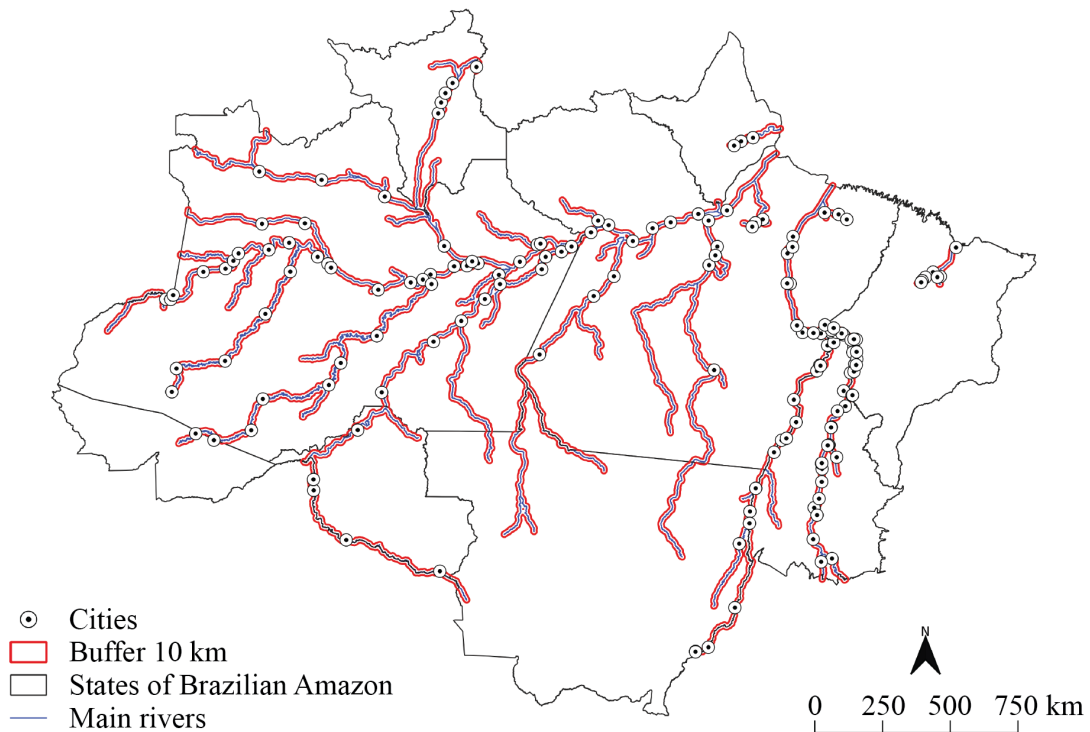
Figure 3-1. Map of the major rivers and cities throughout the Amazonian region of northern Brazil.

The extent to which local winds driven by these wide rivers affect the air quality of these individuals, including the day-to-day variability of these impacts, is largely

unknown, and the possible effects of these flows are not included in air quality models (Ma and Lyons 2003, David and Nair 2011, Li et al. 2020). As one example, observations aboard a boat showed that a change in surface wind direction in the late afternoon led to multifold increases in ozone (O_3) and nitrogen oxides (NO_x) concentrations (Trebs et al. 2012). Pollutant emissions from the nearby urban region of Manaus, Brazil, were advected by this river-induced atmospheric flow to the boat location (Kuhn et al. 2010, Martin et al. 2017, Shrivastava et al. 2019).

River winds represent an interaction between mesoscale meteorological forcing and local landcover (Betts et al. 2009). On different days, the induced flows can vary between extremes of strong winds to entirely absent depending on the heterogeneity of the sensible heat flux and the strength and direction of synoptic winds (Silva Dias et al. 2004, Fitzjarrald et al. 2008, Crosman and Horel 2010, Germano and Oyama 2020). Vertical profiles of meteorological variables and chemical concentrations in the lower several hundred meters of the atmosphere can in principle provide insights and understanding into the development and the effects of the altered atmospheric circulation, yet the needed data sets do not exist. Traditional measurement platforms like tethered balloons (Greco et al. 1992), aircrafts (Andreae et al. 2012, Martin et al. 2017, Fan et al. 2020), and instrumented towers (Martin et al. 2010, Andreae et al. 2015) are not suited to the collection of vertical profiles in the low atmosphere over rivers. Unmanned aerial vehicles (UAVs), in particular copter-type UAVs having take-off weights of <25 kg, represent a new and important capability for vertical profiles across the needed horizontal and vertical scales (Guimarães et al. 2019, Liu et al. 2020, Stewart and Martin 2020).

Electrochemical sensors suitable for UAV flight can detect and quantify air pollutants at atmospherically relevant concentrations (Spinelle et al. 2015, Cross et al. 2017).

In this chapter, vertical profiles of meteorological and chemical data from surface elevation to 500 m collected by a UAV were presented. The dataset was collected during the daytime over a wide river in the central Amazon of northern Brazil in the dry season. The meteorological data were treated by a cluster analysis. The clusters were further applied to interpret the vertical profiles of air pollution, including indicators of atmospheric recirculation that effectively slowed pollutant dispersion.

3.2   Experimental

3.2.1   UAV flights

UAV flights were launched from a boat from 10:00 to 17:00 (local time) across 11 September to 9 October 2019 (Figure 3-2a and b). Local time (LT) was 4 h earlier than UTC. The boat traversed in the morning from the harbor in Manaus to the measurement location in the Rio Negro (3.0708° S, 60.3604° W). Figure 3-2c shows the location of the launch site and the environs in the Rio Negro River. River width varied from 3 to 13 km in this region. For the dominant wind direction, the launch site was 37.5 km downwind from Manaus, Brazil, an urban center of more than 2 million people. The launch location responded to the study requirements of capturing regional sources of pollution within the prevailing synoptic meteorology (i.e., trade winds) as well as to the practical requirements of permissions of aviation authorities for UAV flights (i.e., sufficiently far from the Manaus international airport) and the presence of police patrols against river pirates (i.e., sufficiently close to the Manaus port region).

A hexacopter UAV (Matrice 600, DJI) was used in this study. Telemetry of latitude, longitude, and altitude was based on the Global Positioning System (GPS). The operational capability of the UAVs limited the flight time to < 30 min. The maximum ascending and descending speeds during the study period were 5 m s^{-1} and 3 m s^{-1}, respectively. The maximum altitude was 500 m above local ground, as restricted by manufacturer geofencing. The UAV was launched from the boat deck.
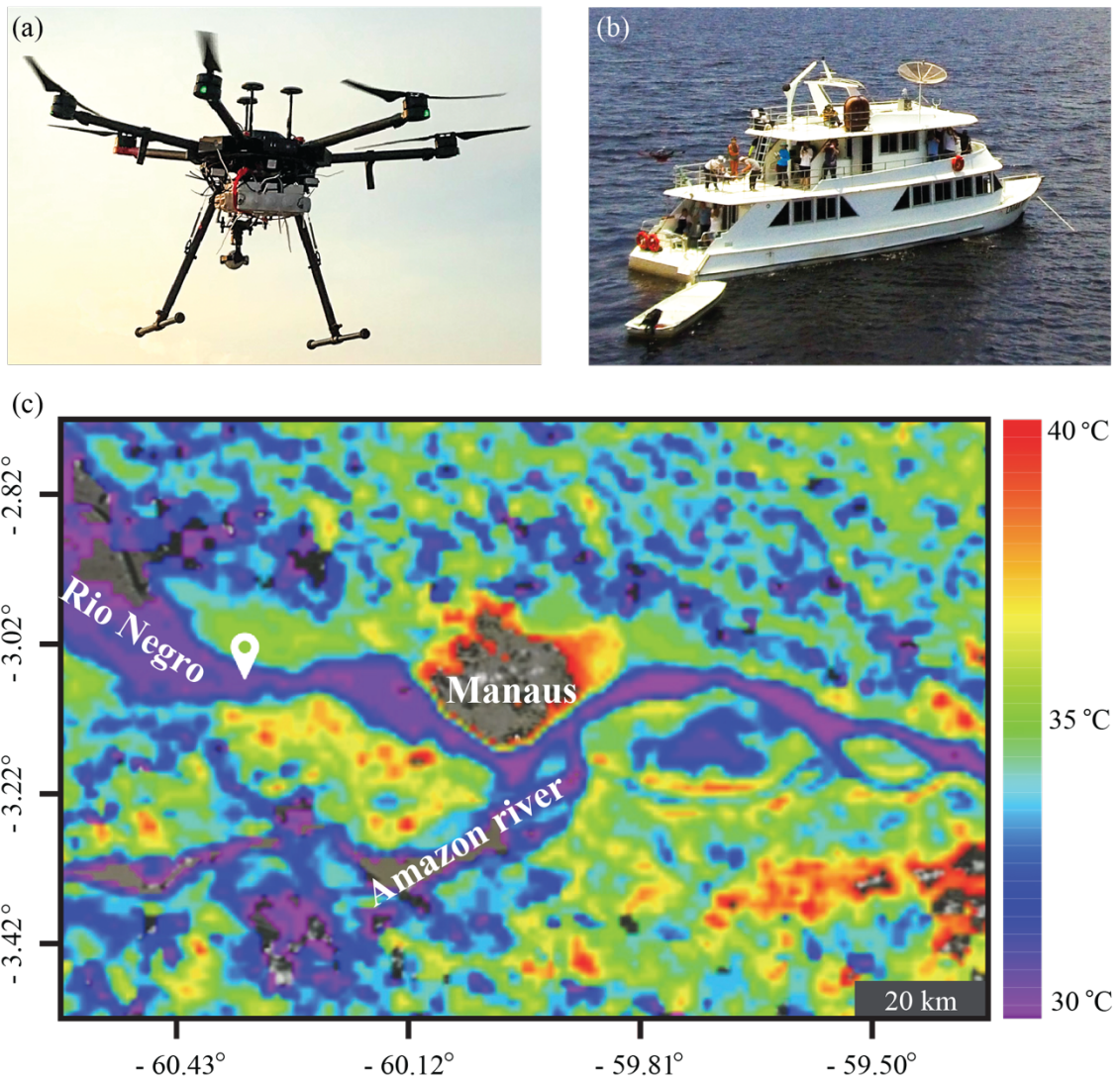
Figure 3-2. (a) photograph of the UAV. The sensor package was mounted to the UAV underside. (b)

photograph of the boat platform from which the UAV was launched and retrieved during the campaign. (c)

Surface temperatures on a fair weather day (Worldview 2020). The data for the false-color image were

taken by the *Aqua* satellite at 13:30 (LT) over Manaus, Brazil, in the central Amazon on 26 September

2019. Satellite image credit: NASA's Earth Observatory.

The UAV flight protocols collected a vertical profile once per hour. The routine

was interrupted on some days because of weather or other unexpected technical issues.

For each flight, the UAV ascended at a speed of 1 m s^{-1} from the boat to 500 m while

recording data.

3.2.2   Meteorological measurements

Wind measurements, including vertical profiles of wind direction and wind speed,

were performed by a UAV-wind sensor system (Model UAV6000, ZOGLAB

Microsystem Co.). Vertical profiles of 1-m resolution were collected by the UAV once

per hour from surface elevation to 500 m for 56 flights. The accuracy of wind speed was

0.5 m s^{-1}. The accuracy of wind direction was 3° for wind speeds faster than 2 m s^{-1}.

Temperature (±0.2 °C) and relative humidity (±2.5% RH) were also measured.

The native data of the wind sensor equipped on the UAV were relative to the front

orientation of the UAV. An onboard compass recorded the orientation of the UAV

relative to magnetic north. The magnetic declination at the UAV launching site aboard

the boat during the campaign period was 15.8333° W ± 0.3333° (NOAA 2020). A

correction to the native data for geodetic north was as follows:

$$\text{Wind direction} = D + C + M \qquad \text{(Eq. 3-1)}$$

where D was the magnetic declination, C was the compass reading, and M was

the wind direction from wind sensor.

A zenith-pointing lidar system (Model LWR2500, ZOGLAB Microsystem Co.) on the boat recorded altitude-resolved horizontal wind speed and direction from 50 m to 2500 m. The vertical resolution was 50 m. The accuracy for the wind speed was 0.5 m s^{-1}. The accuracy for the wind direction was 3°. Data were averaged for one minute. Relative wind direction changes compared to the measurement at the lowest altitude (50 m) were used in the analysis to compensate for boat rotation.

3.2.3 Chemical sensing

The chemical sensor package was affixed to the underside of the UAV. This position protected it from overheating under solar illumination. The sensor package was housed in a weather-proof plastic enclosure (20.1 cm × 15.5 cm × 7.9 cm). Electrochemical sensors measured carbon monoxide (CO) and total oxidants (O_x, defined as ozone and nitrogen dioxide) (Table 3-1). Data were recorded every 1 s.

Table 3-1. Sensor type, manufacturer, and model for species detected by the sensor package.

Species	Type	Manufacturer	Model
CO	Electrochemical	Alphasense	CO-B4
O_x	Electrochemical	Alphasense	Ox-B431

Calibration for temperature compensated for the temperature gradient with altitude during flight (Appendix Figure A-3). The root-mean-square error of the calibration was 40 ppb for CO and 6-8 ppb for O_x. For comparison, the observed magnitudes in the changes in the vertical trend for CO and O_x concentrations were 100 and 10 ppb, respectively. These magnitudes greatly exceed the error.

The calibration of the electrochemical sensors was difficult under the tropical field conditions when operated from the boat, and drift in sensor response was observed across several days. Drift is well documented for electrochemical sensors(Spinelle et al. 2015, Cross et al. 2017, Wei et al. 2018). The drift, however, was sufficiently small that precision was maintained across the measurements for the flights of a single day. In this case, normalized data from 0 to 1 based on the gradient for each day allowed qualitative patterns to be compared across days, as follows: $\delta_z = (C_z - C_0)/C_0$ where δ_z is a normalized datum at altitude z, C_z is the apparent concentration measured at altitude z, and C_0 is the apparent surface concentration. After application of quality-control criteria, the raw data set of 56 vertical profiles was reduced to a refined data set of 25 profiles (Appendix B-2).

Across the campaign, the average surface concentrations for CO and O_x were 223 ppb and 18 ppb, respectively. The O_x concentration was an upper limit of the O_3 concentration. These CO and O_x concentrations were in the same range as those of aircraft measurements at 500 m that were carried out in the GoAmazon2014/5 campaign in the same geographical region (Table 3-2). In that study, mid-day values of ozone ranged from 20 to 60 ppb in the dry season.

Table 3-2. Comparison of median and percentiles between the calibrated concentrations obtained from the sensor package of this study and the concentrations obtained by aircraft measurement during the dry season of GoAmazon2014/15. Aircraft measurements at 500 m in the region of 2.938344° S to 3.218605° S and 59.797218° W to 60.365074° W were used in the comparison(Martin et al. 2017).

	CO (ppb)	O_3 (ppb)
Aircraft (GoAmazon2014/15)		
25% percentile	135	25

Median	157	33
75% percentile	186	45
Sensor package (this study)		
25% percentile	45	0
Median	132	9
75% percentile	200	19

3.3 Results and discussion

3.3.1 Meteorological observations and clusters

A fuzzy c-means (FCM) clustering algorithm was applied to the vertical profiles of the radial wind components of speed and direction (Bezdek et al. 1984). Similar to k-means clustering, FCM clustering algorithm attempts to divide the input data into a collection of c fuzzy clusters under certain criterion. The determined clustering result minimizes the sum of weighted means of distance between the data points and cluster centroids. FCM is better than k-means clustering in the context of real-world complications with overlapping patterns and noises.

The FCM algorithm identified four clusters. This cluster count maximized the fuzzy partition coefficient and led to a meaningful interpretation of the set of clusters (Appendix B-4). The FCM algorithm assigned four fractional degrees of cluster membership to each vertical profile (Figure 3-3). The degrees of membership sum to unity for each profile.
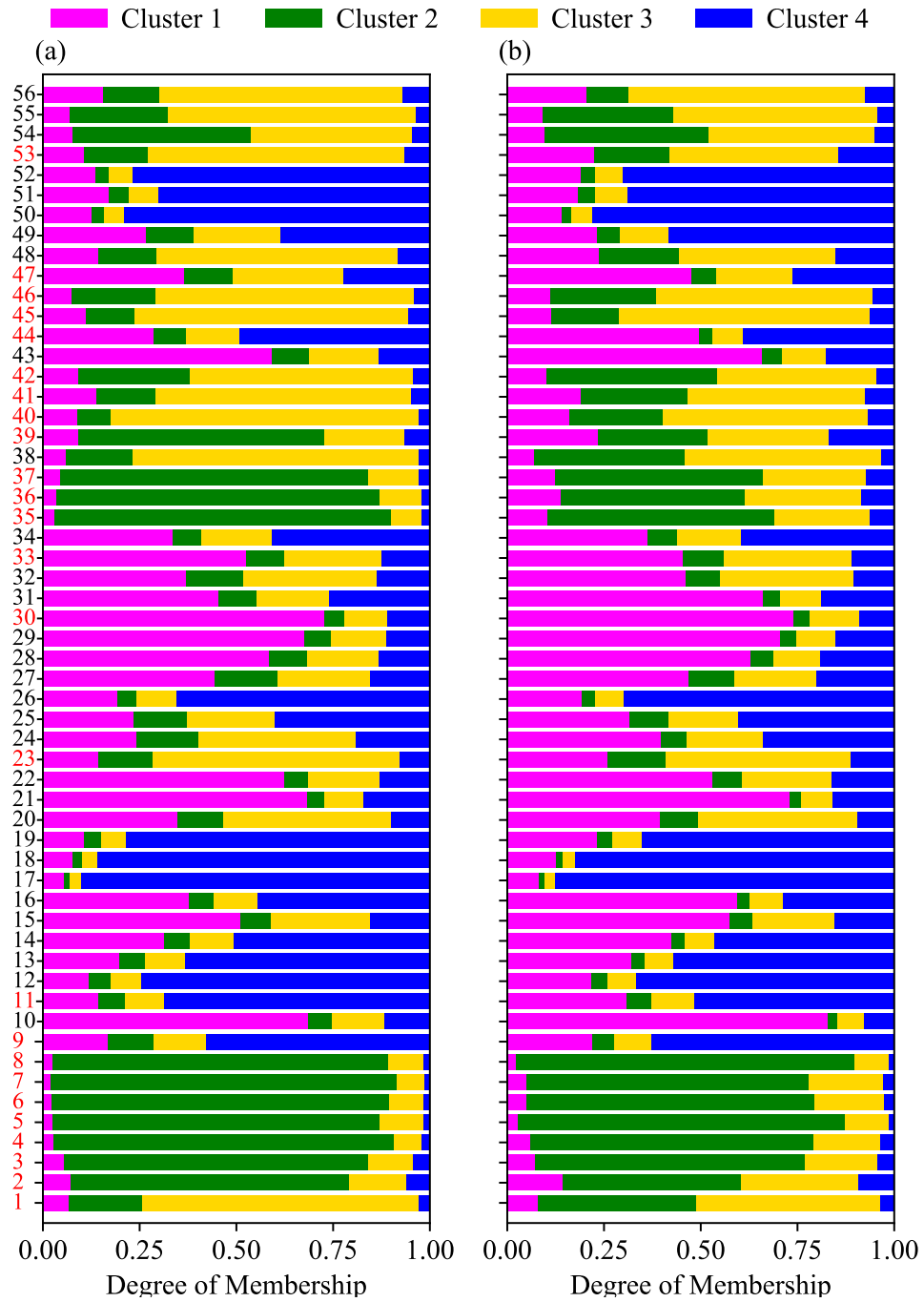
Figure 3-3. Degrees of membership to each cluster for each vertical profile using as the clustering input: (a) wind direction and speed and (b) wind components (*u*, *v*). Flights numbers 1 to 56 are listed. Red coloring for a flight number indicates that there was a contemporaneous vertical profile of chemical species concentrations for this flight.

The cluster centroids of wind direction and wind speed are plotted in Figure 3-4. A fuzzy c-means (FCM) clustering algorithm was also applied to the vertical profiles of wind components u and v as a complementary approach to clustering by wind speed and wind direction. Wind component u is in the north-south direction, and positive values indicate to the north. Wind component v is in the east-west direction, and positive values indicate to the east. The cluster centroids for u and v and the associated variability are plotted in Figure 3-5. The clustering by Cartesian wind direction u and v leads to the same categorization as by wind speed and wind direction (Figure 3-3), thereby reinforcing the confidence in the overall findings.
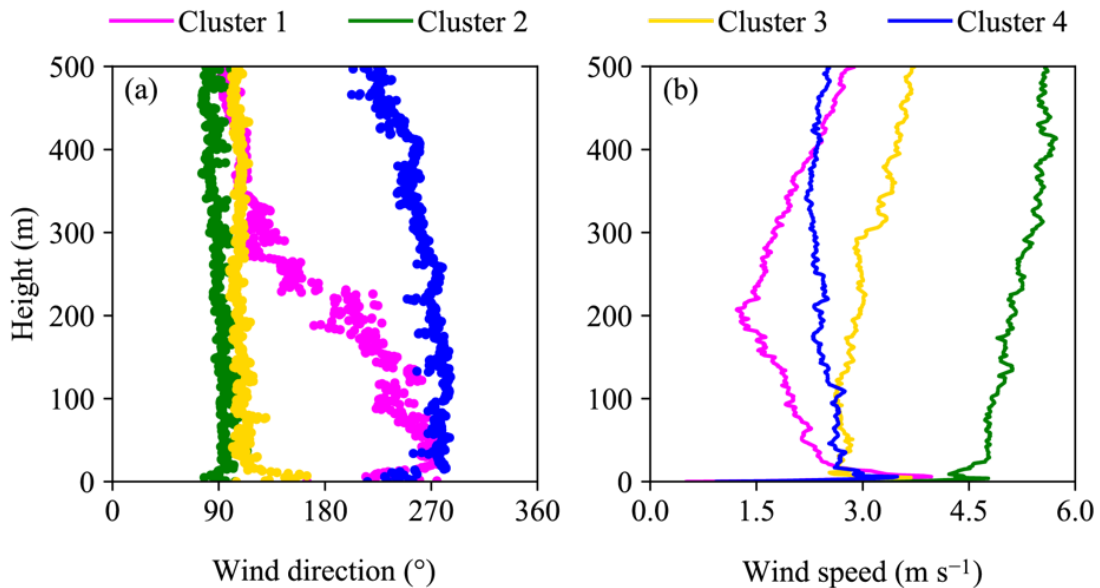
Figure 3-4. Four meteorological clusters identified by analysis of 56 vertical profiles of wind speed and direction data. (a, b) Cluster centroids of wind direction and wind speed from surface elevation to 500 m.
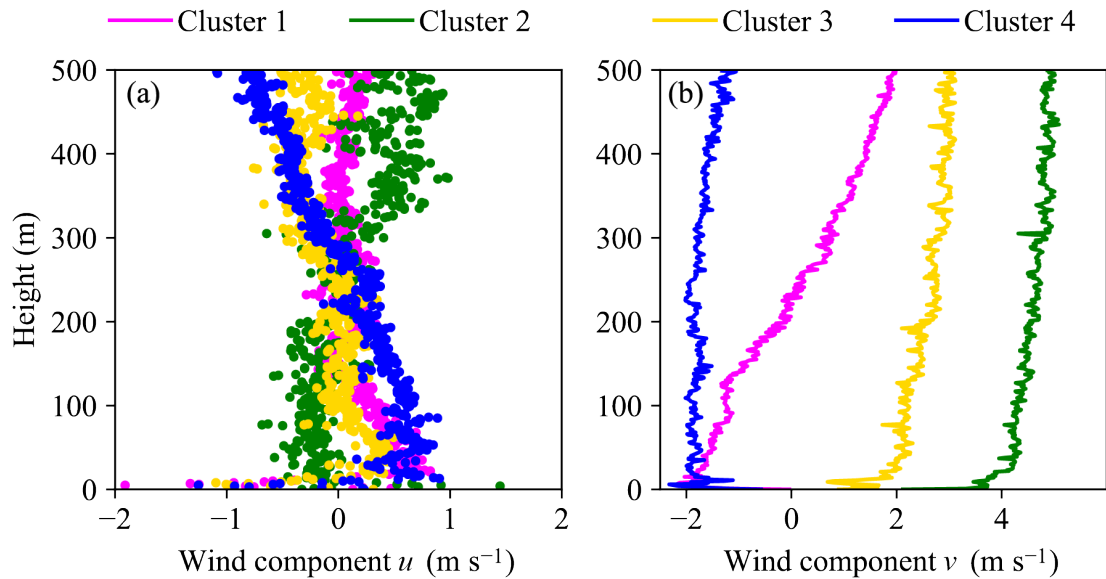
Figure 3-5. Four meteorological clusters identified by analysis of 56 vertical profiles of wind component data. (a, b) Cluster centroids of wind component u and v from surface elevation to 500 m.

For the lidar dataset, the wind direction and the wind speed from surface elevation to 500 m were classified using the FCM algorithm. The centroids of the four identified clusters are plotted in Figure 3-6. These clusters were dominant for 12%, 56%, 23%, and 9% of the time, respectively. The relative segmentation can be compared to that obtained for the UAV data set: 23%, 21%, 25%, and 31%. The explanation for differences is that the lidar clusters were derived from analysis of a continuous time series whereas the UAV clusters corresponded to stepwise intervals.
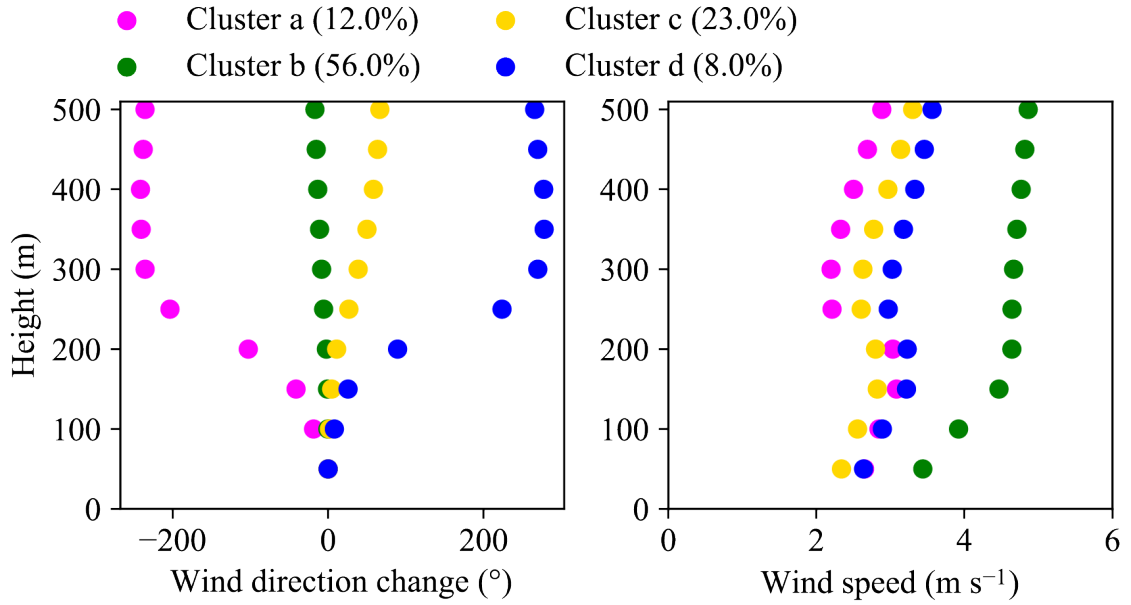
Figure 3-6. Four meteorological clusters identified by analysis of 56 vertical profiles of wind data from lidar. (a, b) Cluster centroids of wind direction and wind speed from surface elevation to 500 m.

Figure 3-7 shows a comparison of the degrees of membership for the UAV and lidar clusters across four days. The degrees of membership for the lidar clusters (a, b, c and d) correspond well to those identified for the UAV data ("UAV" cluster 1, 2, 3, and 4) for the same flight times. The data sets of the lidar on the boat reinforced the four cluster assignments.
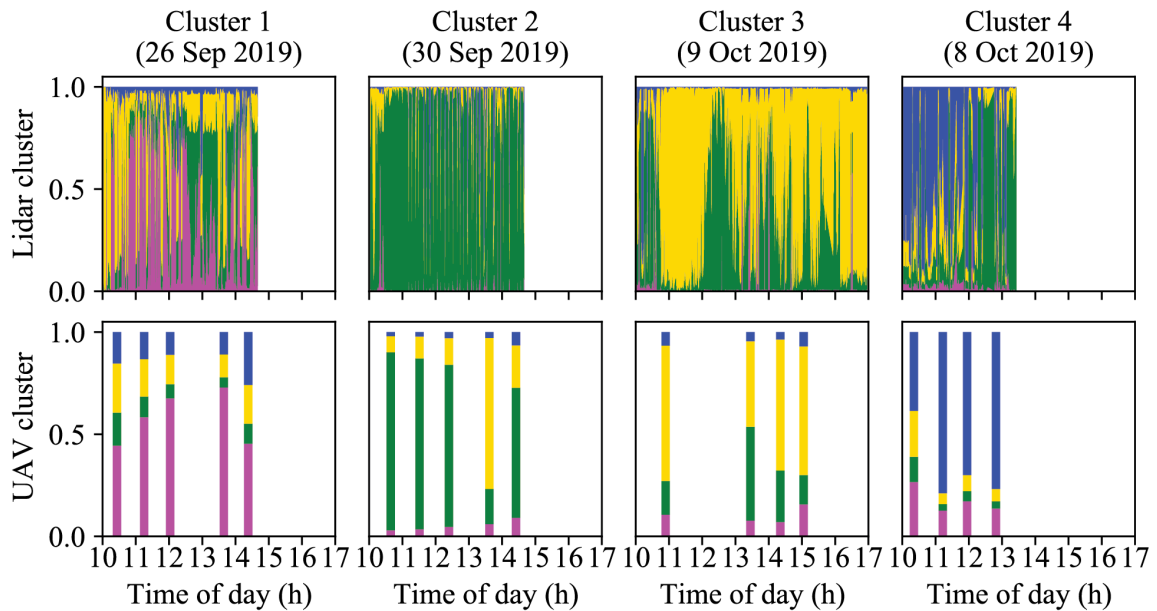
Figure 3-7. Degrees of membership to each cluster across the daily time series. The top row represents the lidar data. The bottom row represents the UAV clusters for comparison to the lidar data. The blank area indicates lack of data. The color coding follows that of Figure 3-4.

The four clusters are summarized in Table 3-3. The degree of membership to a single cluster exceeded 0.5 for 79% (44 of 56) of the profiles (Figure 3-3), and the clusters corresponded to distinct meteorological regimes.

Table 3-3. Clustering analysis of the vertical profiles of meteorological data. The parenthesized numbers indicate how many profiles out of 56 occurred in each cluster.

Cluster	Occurrence	Synoptic Wind Speeds (m s⁻¹)	Other Characteristics
1. Strong local circulatory flows of river winds.	23% (13)	2.5	Fair weather

Cluster	Occurrence	Synoptic Wind Speeds (m s^{-1})	Other Characteristics
2. No apparent circulatory flow. Flow over river appears same as over forest.	21% (12)	>4	Fair weather
3. Weak to perturbed local circulatory flows of river winds.	25% (14)	<4	Cirrus and high-altitude stratus clouds
4. Other types of flows.	31% (17)	2.5	Inclement weather and other factors

Cluster 1, prevalent for fair-weather cumulus clouds over the land, had the distinguishing feature of a complete reversal of wind direction at mid-height. The centroid for this cluster had westerlies below 100 m that transitioned into easterlies above 300 m (Figure 3-4). Correspondingly, there was a local minimum in the wind speed at 200 m. Trade winds (i.e., easterlies) dominated the wind field above 300 m, and the local circulatory flow of the river-forest landscape affected the wind field at lower altitudes. The raw meteorological data for flights in cluster 1 are plotted in Figure 3-8. These observations represent a canonical example of strong local circulatory flows of a closed sub-cell (Miller et al. 2003, Silva Dias et al. 2004, Betts et al. 2009). During periods of cluster 1, satellite images show that there were typically no clouds over the river (Figure

3-9a). The air rising over the land desiccated, and it subsequently descended without cloud formation over the rivers (Ramos da Silva et al. 2011).
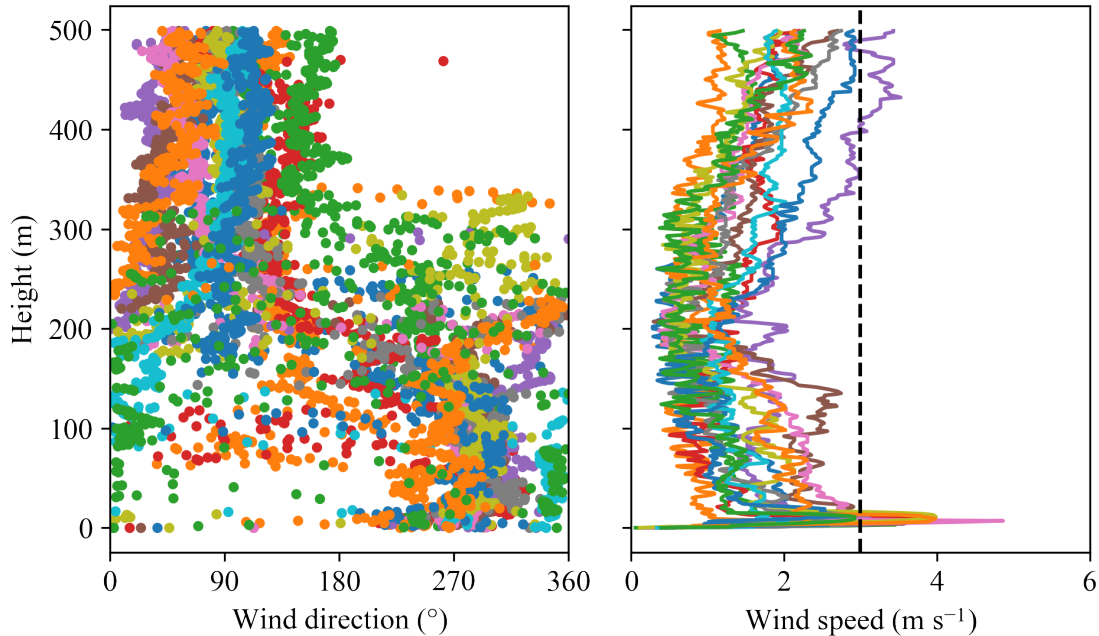
Figure 3-8. Vertical profiles of wind direction and wind speed for flights in cluster 1. The color represents different flights.

Interestingly, the sub-cell of the river winds for cluster 1 ran as easterlies and westerlies. The expectation given the river orientation and the positioning of the boat could be for northerlies and southerlies, at least for the ideal situation of a river breeze. An ideal situation corresponds to no regional winds, uniform heating at both riverbanks, and consistent east-west river orientation. However, in the real case, the physics were more mixed, including additional simultaneous forcing by both synoptic and river-forest factors. Easterly trade winds were present, the southern bank of the river was usually warmer than the northern bank, and the river orientation around flowed in the direction of

northwest to southeast, instead of west to east, on a slightly larger spatial scale (Figure 3-2c).
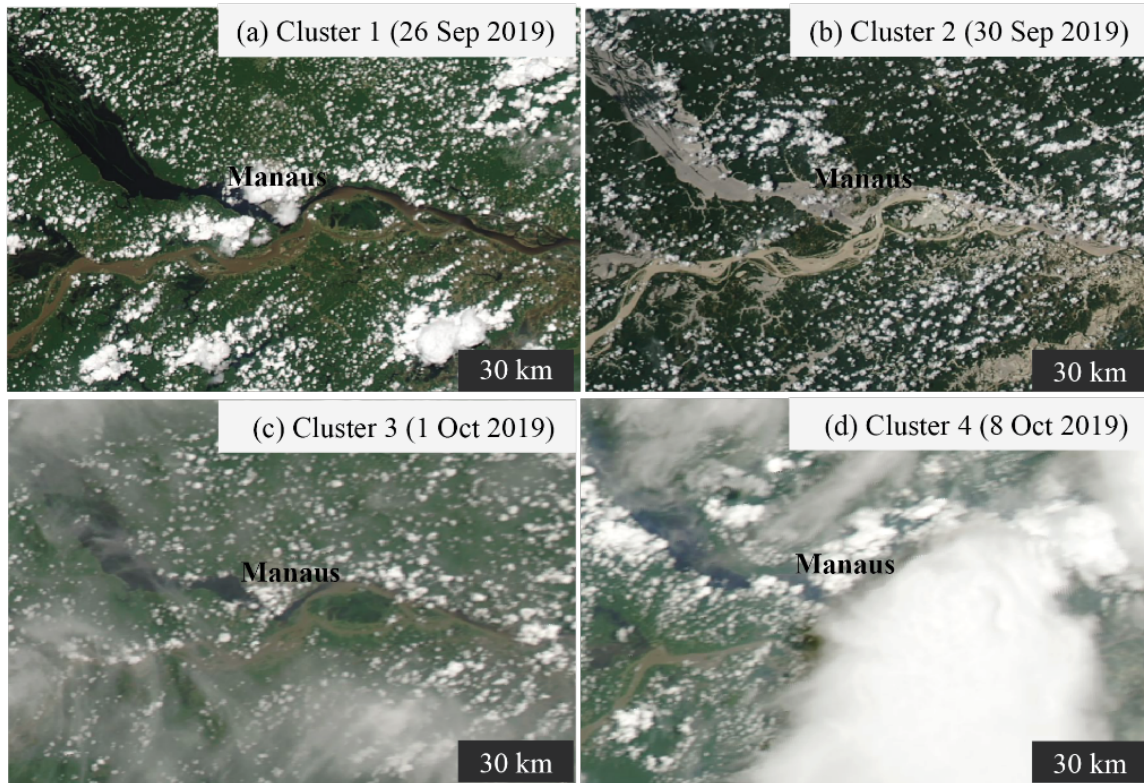
Figure 3-9. Satellite images of cloud coverage that were typical of clusters 1, 2, 3, and 4, respectively(Worldview 2020). Images were taken by the *Aqua* satellite at 13:30 (LT) on 26 September 2019, 30 September 2019, 1 October 2019, and 8 October 2019. The imaged rivers correspond to those apparent in Figure 3-2c. Satellite image credit: NASA's Earth Observatory.

These factors contributed to the difference between the expectations for ideal river breezes and the observations of real river winds produced by simultaneous mixed forcing physics. Besides, the wind roses of other research sites away from the rivers show that westerlies are rare in the central Amazon because of the prevailing equatorial trade winds (Figure 3-10). The observation of westerly surface winds for cluster 1 is thus a direct consequence of the induced flows that manifested as river winds.

(a)

(b)
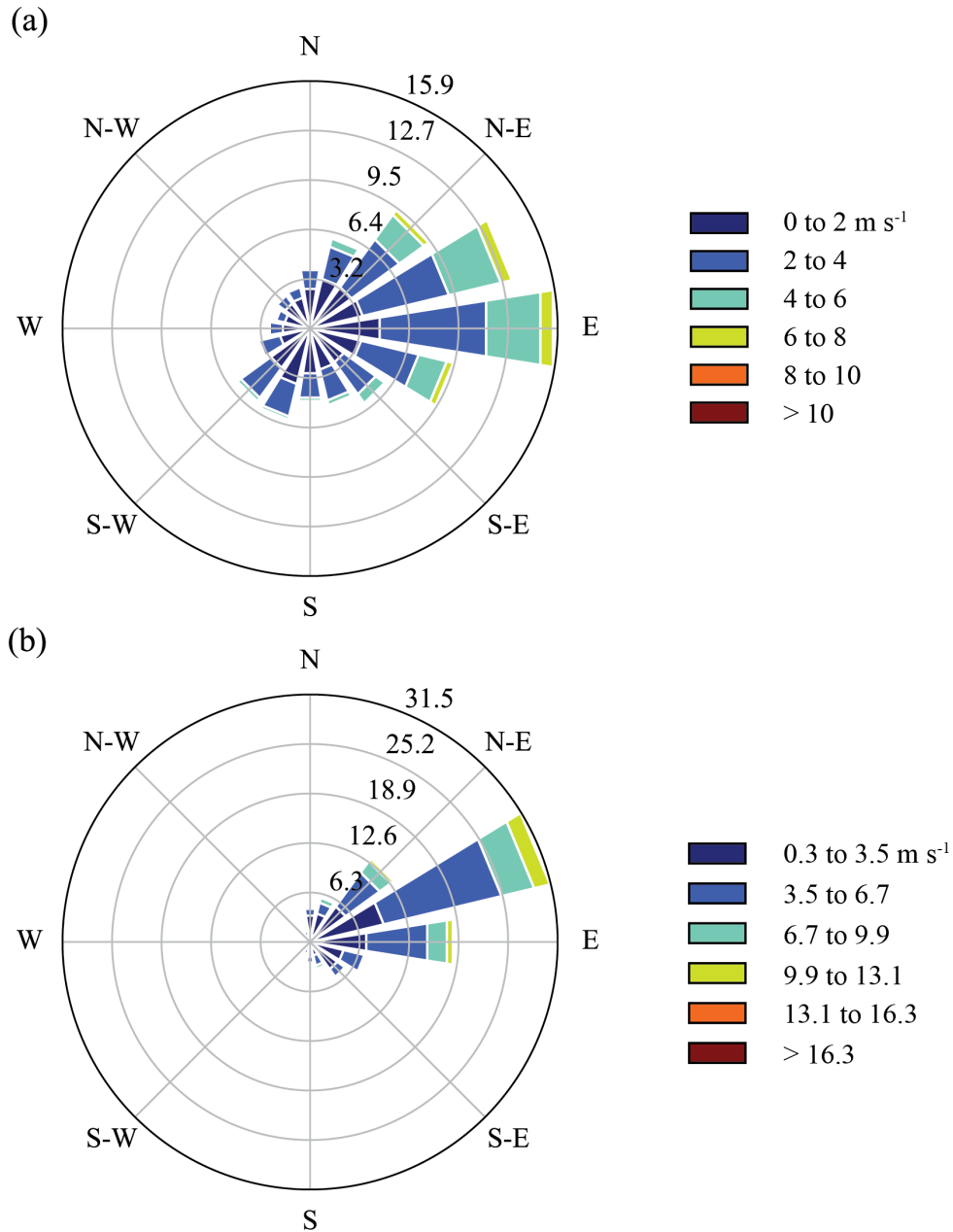
Figure 3-10. Daytime wind rose from 10:00 to 17:00 (LT). (a) Data set of 1 Sep 2014 to 31 Oct 2014 collected during the GoAmazon2014/15 campaign at the T3 site located 70 km to the west of Manaus (Martin et al. 2017). (b) Data set of 1 Sep 2019 to 31 Oct 2019 collected from the ATTO tower located 156 km to the northeast of Manaus (Andreae et al. 2015).

Cluster 2, which like cluster 1 also occurred at times of fair-weather cumulus clouds, was characterized by fast (>4 m s^{-1}) and uniform easterlies of the trade winds

from the surface elevation up to 500 m throughout the day (Figure 3-4). The characteristic signs of strong local circulatory flows of river winds that were apparent in the meteorology of cluster 1 were absent for cluster 2. Instead, the vertical profiles were as they occur over the forested regions under the influence of the trade winds. Although the satellite observations of fair-weather cumulus clouds might suggest favorable weather for thermally induced circulation over the river (cluster 2, Figure 3-9b), the pressure gradient at the synoptic scale was large enough, as reflected in the fast winds, that the air flow was dominated by this synoptic forcing (Sozzi et al. 1998). The physics of local circulation were overwhelmed.

The characteristics of cluster 3 were similar to those of cluster 2 in terms of easterlies and the absence of signs of strong local circulatory flows. The wind speeds (<4 m s^{-1}), however, were less than those of cluster 2, and the associated satellite images also differed between the two clusters. For cluster 3, cirrus clouds were typically present (Figure 3-9c). They reduced surface insolation, resulting in a smaller temperature difference between the land and the river (Lee et al. 2009). The development of the thermally induced local flows of river winds has two requirements (Crosman and Horel 2010): (1) the temperature difference between the land and the river and hence the buoyancy of the air over them must induce a sufficiently large horizontal pressure gradient for horizontal air movement and (2) the pressure gradient from the synoptic winds must be sufficiently small that the local pressure gradient is retained. For cluster 3, both requirements were met but only weakly. Forcing from the synoptic winds and the thermal effects from the river-forest landscape simultaneously affected the atmospheric flow, and they did so with high variability. As a result, although there were similar

centroids of wind direction between clusters 2 and 3 (Figure 3-4), there was a signature

difference between them of low variability around the centroid of wind direction for

cluster 2 compared to a high variability for cluster 3 (Figure 3-11).
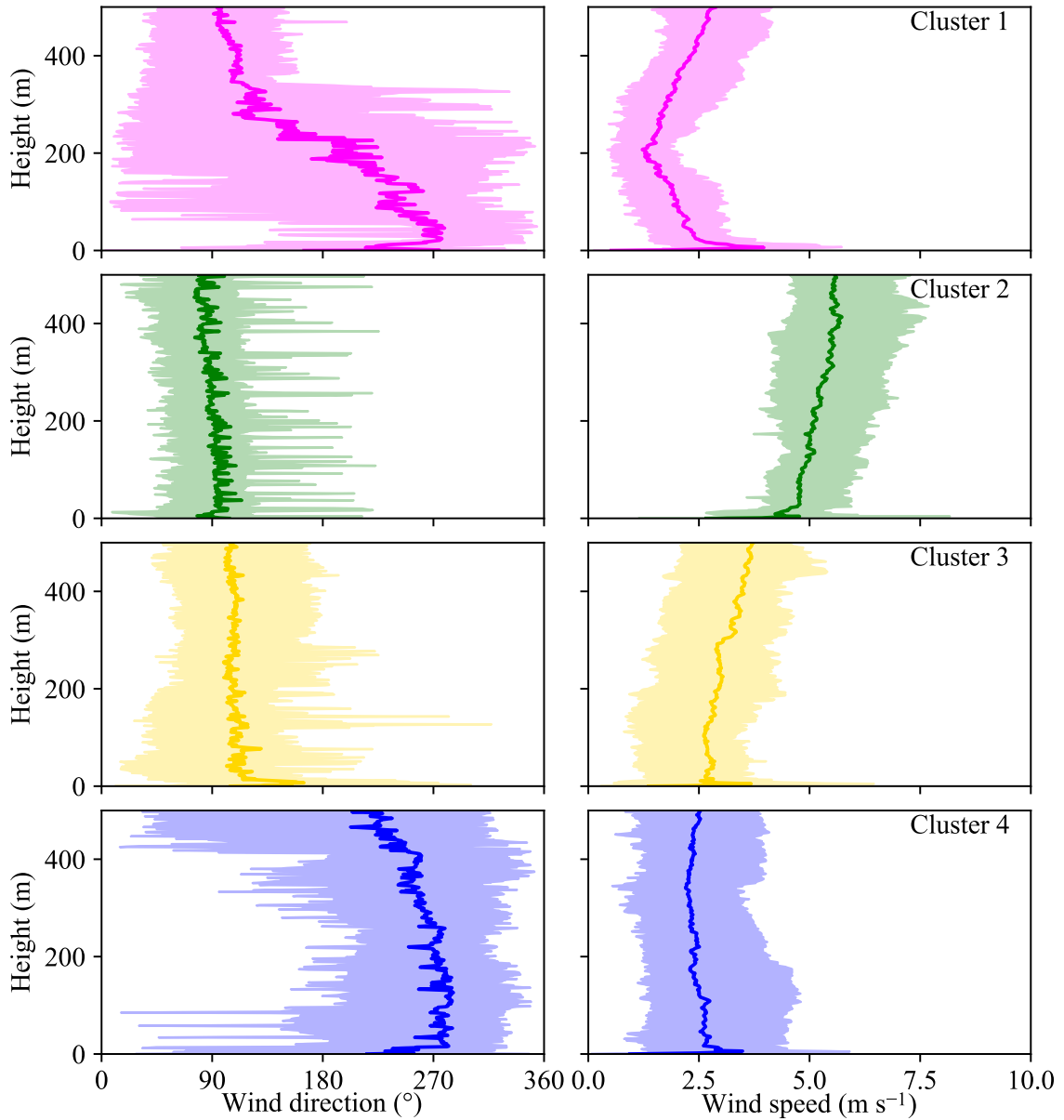
Figure 3-11. Variability of wind direction and wind speed within each cluster. The solid lines are cluster

centroids. The shading represents 90% quantiles of the underlying profiles in the cluster.

Cluster 4 had weak westerlies in the surface region. Above 300 m, there was a drift southerly to the point of maximum UAV altitude (i.e., 500 m). The wind speed of the centroid was 2.5 m s^{-1} from the surface elevation to 500 m. There were two main features that distinguished cluster 4 from cluster 1: (1) the drift of wind direction was above 300 m and (2) the wind speed did not have a minimum at mid-height. These characteristics of cluster 4 might be related to several different possibilities, including various types of strong convection. For instance, 47% (8 of 17) of the profiles in cluster 4 occurred proximate to the arrival or departure of inclement weather, as reflected by the presence of large convective clouds in the satellite images (Figure 3-9d).

The remainder of the analysis focuses on cluster 1, which was observed in 23% of the flights, to explore links between river winds and recirculation of local pollution.

3.3.2   Vertical profiles of pollutant concentrations

The coupling represented by cluster 1 between pollution and local recirculation is depicted conceptually in Figure 3-12.
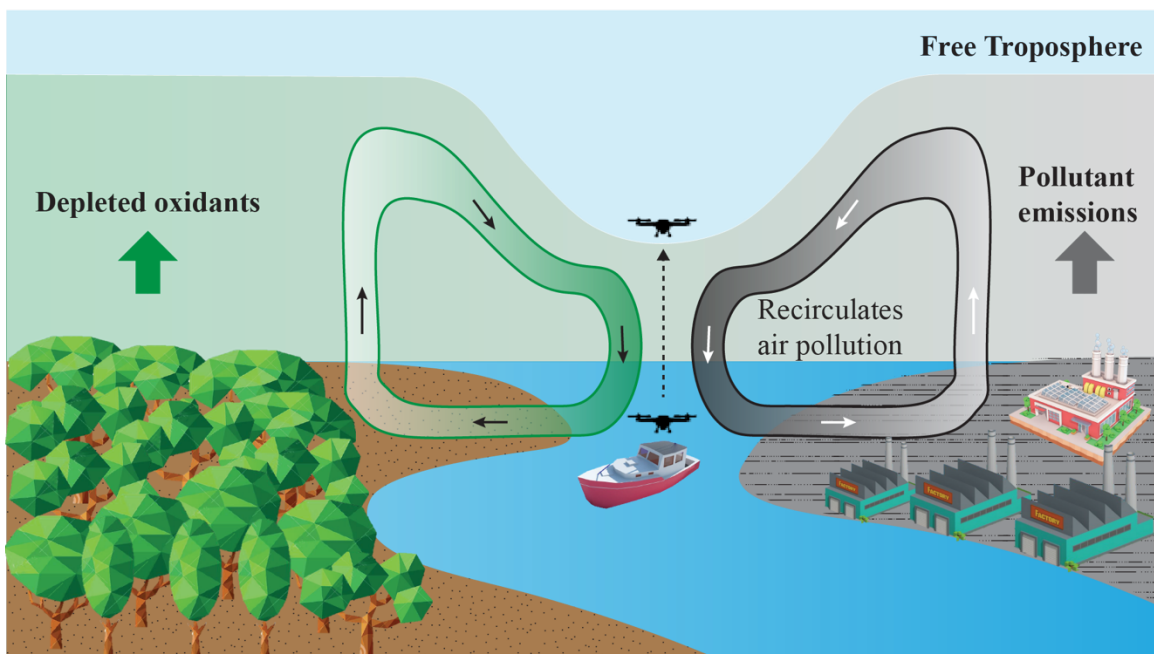
Figure 3-12. Representation of thermally driven recirculatory flow of river winds and reduced rates of pollutant dispersion in a river-forest landscape.

Among 25 chemical profiles, three of them fell within cluster 1. Vertical profiles of pollutant concentrations are plotted in Figure 3-13 for a representative flight of cluster 1. Changes in wind direction at mid-altitude accompanied increases in the carbon monoxide (CO) and total oxidants (O_x, defined as O_3 and NO_2) concentrations, and normalized gradients in species concentration from the surface elevation to 500 m for each flight were used in the analysis. Scatter in wind direction from 100 to 200 m arose from the low wind speeds that accompanied the reversal in wind direction across this altitude range (gray region, Figure 3-13). Arrows in Figure 3-13 demarcate inflection points in the pollutant concentrations at 180 m. The altitude of the increased concentrations aligned with the height at which the wind direction changed in the circulation cell.
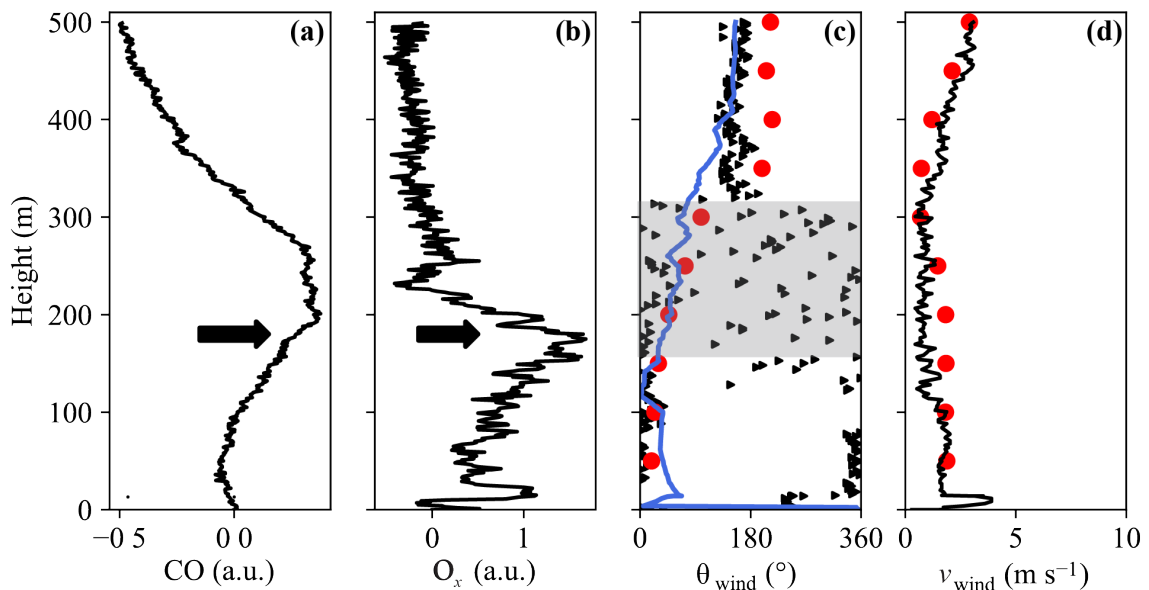
Figure 3-13. Vertical profiles of normalized CO and O_x concentrations, along with meteorological parameters, from surface elevation to 500 m for an individual UAV flight at 13:53 (LT) on 7 Oct 2019

(flight 47, representative flight of cluster 1). (a) Normalized CO concentration. (b) Normalized O_x concentration. (c) Wind direction. (d) Wind speed. Horizontal arrows show inflection points in the vertical profiles. Lidar observations from the boat are in overlay as red points. The gray bar highlights the altitude band across which low wind speeds occurred, and wind direction was less certain. For comparison, the blue line is a 50-m moving average of the UAV data.

The UAV measurements of the wind speed and the wind direction were confirmed by the lidar observations aboard the boat. The red points in Figure 3-13 show the lidar observations, which had a vertical resolution of 50 m. The 1-m UAV data were smoothed to 50 m to allow for the comparison (blue line, Figure 3-13). Typical daytime boundary layer heights approach 1500 m during dry season in the central Amazon (Carneiro and Fisch 2020). Figure 3-14 further shows the lidar data from surface elevation to 1500 m during the flight of Figure 3-13. At altitudes far above the river winds, wind direction was unchanged, and wind speed continuously increased, as expected.
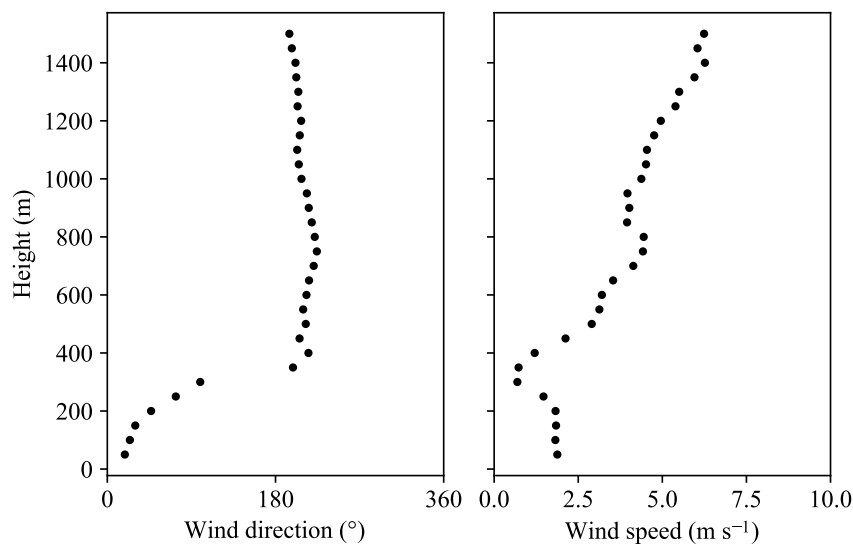
Figure 3-14. Wind direction and wind speed from lidar measurements at 50-m spatial resolution for a representative flight of cluster 1 (Figure 3-13).

The vertical profiles of pollutant concentrations in Figure 3-13 can be explained by strong local circulatory flows of a closed sub-cell over a river-forest landscape when there were nearby pollutant emissions. As depicted in Figure 3-12, polluted air from the land source was transported from the surface to above 300 m in the branch of upward convection in the circulation cell, and this pollution then descended over the river to below 300 m in the downward branch of the cell. Back-trajectories indicate that the air originated to the southeast where there were many wood-burning brick kilns that had high CO emissions nearby the river (Figure 3-15)(de Sa et al. 2019). One group of brick kilns was within 10 km of the UAV launch location. There were also biomass burning hotspots on these days further along the back-trajectories from 80 to 120 km, representing 4 to 6 h of transport time, and biomass burning was also a strong source of CO emissions (Ribeiro et al. 2018).
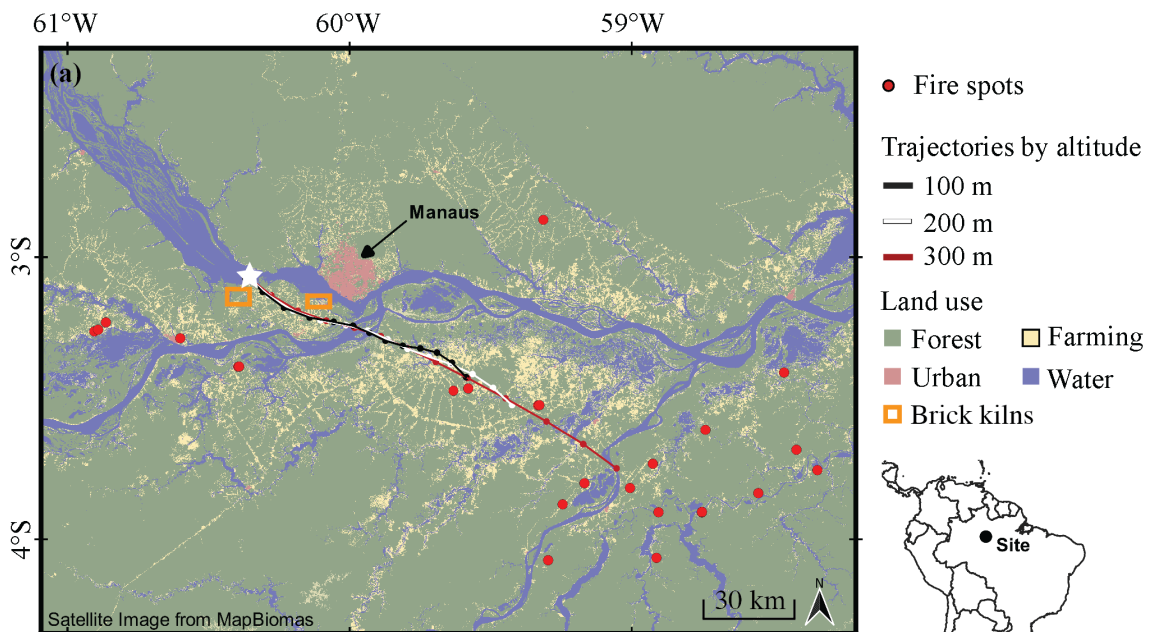
Figure 3-15. Back-trajectories for 7 Oct 2019 of flight 47 from 14:00 (LT) at 100 m (black), 300 m (white), and 500 m (red). Each point represents 1 h. Locations of groups of brick factories, serving as pollution

sources, are shown as orange rectangles (Martin et al. 2016). Sites of biomass burning are shown as red points. The location of the UAV launching site aboard the boat is represented by a white star.

For all clusters, the CO concentration decreased with height. Vertical profiles are plotted in Figure 3-16 for flights representative of each cluster (i.e., based on the degree of membership). A decrease in CO concentration with altitude for all clusters is consistent with other Amazon observations of CO concentrations across a larger altitude range from 500 m to 3000 m (Sachse et al. 1988, Andreae et al. 2012). In the case of cluster 1, there was an inflection point of CO concentration at mid-height. Figure 3-13 shows that the O_x concentrations likewise decreased and then increased across 100 m to 250 m for cluster 1. Wind speed and wind direction changed across the same altitude range (Figure 3-4). Although O_x was lost by dry deposition to both the forest canopy and the river surface, the rate of dry deposition to the water surface was lower (Wesely 1989). The local circulation uplifted O_x-depleted air from the nearby land surface, leading to reduced O_x concentrations for the altitude at which the sub-cell descended over the river (Figure 3-12).
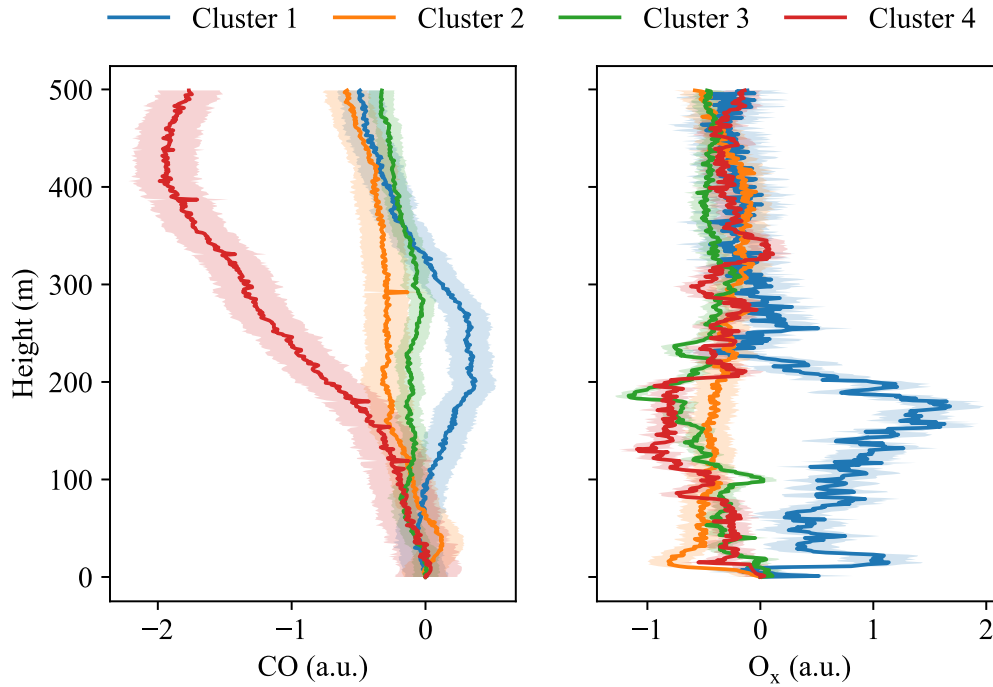
Figure 3-16. Representative chemical profiles for each cluster. Representative flights are selected based on high degree of membership within a cluster. The shaded area is the corresponding uncertainty based on pre-calibration curves.

3.4   Conclusion

The vertical profiles of meteorological variables sampled by UAV flights over a wide river in the central Amazon corresponded to a thermally driven closed sub-cell of strong local circulatory flows, constituting river winds, over the river-forest landscape for 23% (13 of 56) of the flights during the daytime of the dry season. The height of the transition layer for the river winds varied from 150 to 300 m over the surface elevation among different days compared to 1000 to 1500 m for the boundary layer height. Synoptic winds slower than 4 m s^{-1} and an absence of high-altitude clouds favored the development of the sub-cell of river winds. By comparison, for 21% of the flights river

winds were not observed, and during these times strong synoptic trade winds prevailed. More complex behavior than these two limiting extremes was observed during the other flights (56%), in part because of complex mesoscale meteorology such as inclement weather and in part because of mixed physics at times of simultaneous forcing by both synoptic and river-forest factors.

This study provides the first in-situ vertical profile measurements of river winds in central Amazonia. Prior work on this topic was limited to simulation results constrained by onshore data. The dataset collected with sensors onboard unmanned aerial vehicles as well as wind lidar fills the gap between theoretical results and extrapolation from surface measurements. The coupling of river winds to the distribution of atmospheric pollutants was examined. Air quality models can be improved by quantitatively accounting for river winds (at present they do not), and the models can be tested against the data constraints of this study for the role of river winds in the distribution of atmospheric pollutants.

The impacts of local recirculation can be considerable in certain regions. Human settlement throughout northern Brazil is strongly favored along rivers, so the effects of the coupling between pollution dispersion and river winds on local air quality and human health can be important when certain small mesoscale regimes prevail on some days. Regional numerical air quality models today do not incorporate these river-derived processes. Moreover, on days that river winds prevail, the extrapolation of any measurements of chemical concentrations over the river surface or land nearby its banks to a larger regional scale should be considered cautiously. The local circulations can change the spatial pattern and residence time of locally emitted pollution. Linked

epidemiological studies that integrate the role of river recirculation in explaining the spatial micro-heterogeneity of human health outcomes, including environmental equity, should be considered in the future.

The ongoing migration of biomass burning deeper into Amazonia where rivers are abundant and human population along the rivers is prevalent adds urgency to efforts to understand the impact of river winds on air pollution (Davidson et al. 2012). There has been a large and sustained uptick in agricultural and deforestation fires as additional pollution sources in the interior of the Amazon region over the past decade (Amigo 2020, Farias). This phenomenon has unknown health consequences and tie-ins to local meteorology, including river winds. This pattern of biomass burning differs from earlier decades of historical deforestation that was largely restricted along the southern and eastern borders of the Amazon region rather than also in its interior where the population is distributed primarily along rivers. There is a distinct possibility that the coupling between polluted river winds and air quality is degrading public health of the vulnerable populations of northern Brazil. Air pollution management strategies, including air pollution monitoring locations and air quality modeling, should incorporate the effects of river winds into pollution mitigation strategies and policies.

4   River winds and pollutant recirculation in central Amazonia: Modelling

4.1   Introduction

The Amazon basin is the largest river basin on Earth and plays an important role in the biosphere-atmosphere exchange of energy, water, and gases on regional and global scales (Pöschl et al. 2010, Martin et al. 2016, Martin et al. 2017). Several world's longest and widest rivers flow in the Amazon basin, such as the Amazon, Madeira, Negro, and Tapajos rivers (Gibbs 1972). Large rivers are important elements in atmospheric processes in Amazonia and exert significant impacts on atmospheric chemistry and regional climate (Silva Dias et al. 2004, Lu et al. 2005, Fitzjarrald et al. 2008, Santos et al. 2014, Santos et al. 2019).

Thermally driven local circulations in the form of river winds are one of the most important atmospheric processes induced by rivers in the first few hundred meters of the overlying atmospheric boundary layer (Silva Dias et al. 2004). Similar to the sea and lake breezes, river winds are driven by thermal contrast over the river-forest landscape. In the daytime, higher land temperatures and lower river temperatures lead to convective

turbulent motions with the ascent of air over the land and subsidence of air over the river. As a result, there is a tendency for onshore air movement from the river towards the land near the surface, and a local air circulation cell develops in the vertical plane. At night, the air circulation reverses given the cool land and warm river.

Theoretically, there is a 180° reversal of horizontal wind direction between the lower and higher levels of the circulation cell. In a real scenario for rivers, the circulations are strongly influenced by local topography and are formed through a complex interplay of synoptic-scale winds, the physics of thermal contrast in the landscape, and flow over a terrain of variable roughness.

River winds can strongly affect the transport and dispersion of local emissions, in some cases leading to re-circulation. A boat-based campaign was carried out close to the confluence of the Rio Negro River (hereafter, "Rio Negro") and the Solimões River, and collected meteorological and chemical data near the river surface (Trebs et al. 2012). They observed a change of local wind direction in the afternoon and an associated multi-fold increase in ozone (O_3) and nitrogen oxides (NO_x) concentration. Chapter 3 finds that the vertical profiles of carbon monoxide (CO) and total oxidants ($O_x \equiv O_3 + NO_2$) over the river were significantly altered in the presence of river winds. At those times, O_x-depleted air from the nearby forest (i.e., because of reactive loss of O_3 on leaf surfaces) as well as CO emissions from local pollution ascended over the land and descended over the river as they were entrained into the river-forest recirculation. Model simulations further supported the frequent occurrence of river winds in Amazonia and their effects (Oliveira and Fitzjarrald 1994, Silva Dias et al. 2004, Lu et al. 2005, Zhao et al. 2021).

Literature studies suggested that the vertical influence of river winds on pollution dispersion may extend through the depth of planetary boundary layer (Oliveira and Fitzjarrald 1993, Silva Dias et al. 2004). However, this conclusion highly depends on factors such as thermal gradients between the river and surrounding forests and the strength of trade wind, and the relationship can be quantified through numerical modelling (Crosman and Horel 2010).

Large Eddy Simulation (LES) is an important numerical modelling tool that is widely used in atmospheric boundary layer studies. In a typical LES experiment setup, a filter width, or grid size in practical sense, is pre-determined and serve as the threshold between resolving the turbulence and parameterization (Heus et al. 2010). LES combines the advantage of less dependence on parameterization over large scale models and larger coverage over Direct Numerical Simulation (DNS). LES complements the observational studies by presenting a complete view when limited observation data are available, in terms of time and scale.

Among many applications of LES in atmospheric studies, flow over thermally heterogeneous terrain is one of them and can be considered as a simplified case for river winds. Van Heerwaarden et al used LES to study the impact of heterogeneous land surface on cloud formation by altering Bowen ratios to simulate the heterogeneity (van Heerwaarden and de Arellano 2008). The heterogeneity-induced circulations can reach the top of the atmospheric boundary layer and redistribute the moisture, indicated by relative humidity over different terrain. Similarly, the impact of heterogeneous terrain on the segregation of chemical species was studied using the LES and the circulation was

found to have different impacts on chemicals with different reactivity (Ouwersloot et al. 2011).

This chapter focuses on the application of LES in simulating river winds and their impacts on chemical transport. The model was first validated by comparing the meteorological profiles with observational data presented in chapter 3. The impact of river winds on chemical transport and interpretation of riparian tower measurement was investigated in the absence of synoptic-scale wind field.

4.2   Experimental

River winds and the induced pollutant recirculation was simulated using the *Dutch Atmospheric Large Eddy Simulation* (DALES) (Version 4.1) (Heus et al. 2010). DALES has been validated in the Amazon region (Ouwersloot et al. 2011). Within DALES, there was an on-line module for chemical kinetics so that coupled emissions, chemistry, and transport could be examined within the atmospheric boundary layer (Vilà-Guerau de Arellano et al. 2005). The domain setup is depicted in Figure 4-1. The default river width was 5 km in a domain width of 25 km. There was a periodic lateral boundary condition. The forest size in the periodic domain was sufficiently wide to isolate the river in each cell. There was a point source of CO emissions (0.13 mg m^{-2} s^{-1} or 100 ppb m s^{-1}) that was 2.5 km inland (Figure 4-1).
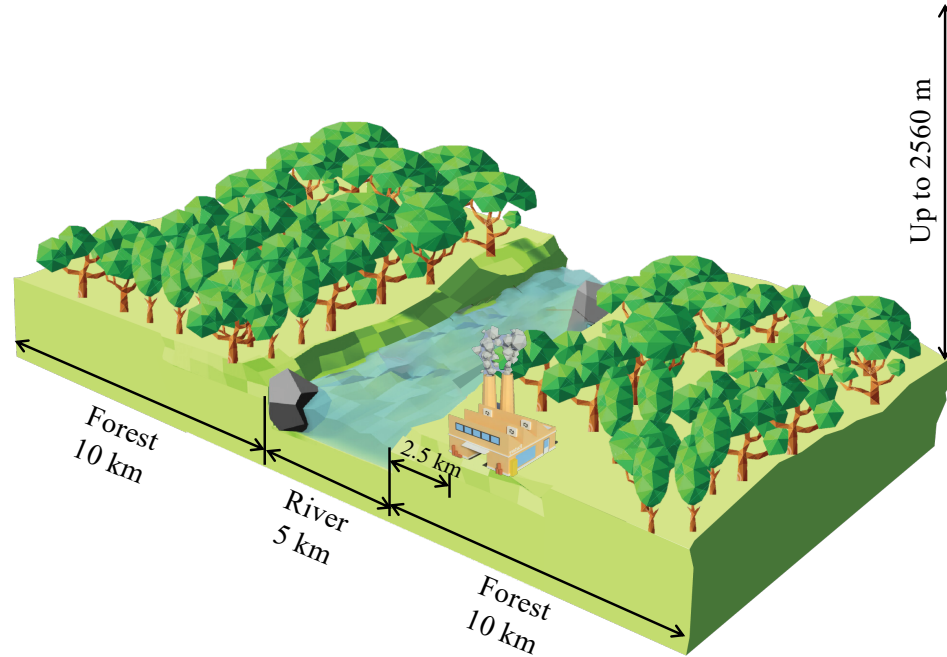
Figure 4-1. Plan view of the setup for the large eddy simulation (LES) of pollutant emissions from a nearby point source

A homogeneous landscape held in the longitudinal direction. The grid size within the domain was 50 m × 50 m × 20 m. This size was selected to adequately resolve turbulent energies (Ma et al. 2021). The simulation timestep was 1 s. For each simulation, the first hour was used for model spin up, and the simulation was conducted for an additional two hours after that. The simulation time was sufficient to establish steady-state results for the explored meteorology and chemistry. An average across the last hour was used for the results presented herein.

Parameters of DALES for the Amazon environment were previously developed (Vilà-Guerau de Arellano et al. 2011, Vilà-Guerau de Arellano et al. 2020). For the forest landscape, sensible and latent heat fluxes for the reference case of the set of simulations were prescribed and based on literature for the central Amazonia (Oliveira and Fitzjarrald

1994, Broedel et al. 2017). For the river landscape, the heat fluxes of the reference case were based on values for other large water bodies, such as lakes (Verburg and Antenucci 2010, van Emmerik et al. 2013). Noontime (local time) values were used for heat fluxes. The parameters were optimized to reproduce the meteorological observations of the campaign and details are shown in Table 4-1. The simulated chemical concentrations were normalized from 0 to 1 across the minimum and maximum values.

Table 4-1. LES configuration

Domain	
Horizontal, (L_x, L_y)	(5000, 25000)
Vertical, L_z	2560
Grid points, (N_x, N_y)	(100, 500)
Grid points, N_z	128
Resolution, (Δx, Δy, Δz)	(50, 50, 20)
Geographic coordinates for radiation	
Latitude	-3.003
Longitude	300.6
Julian day	280
Starting hour simulation	16 UTC (12 LT)
Boundary conditions	
Horizontal	Periodic
Upper	Sponge layer

Lower	Coupled land surface model	
Time integration		
Time step, dt	Variable, set by CFL criterion for a maximum value 1 s	
Integration time	10800 s	
Averaging time statistics	60 s	
Initial conditions		
Wind profile	$0 < z < 2560$ m	$(u, v) = (0, 0)$ m s^{-1}
Subgrid turbulent kinetic energy profile	$0 < z < 2560$ m	TKE $= 0.0$ m^2 s^{-2}
Potential temperature profile	$0 < z < 200$ m	$\theta = 300$ K
	$200 < z < 2560$ m	$\theta = 300 + 0.006\,(z - 190)$ K
Specific humidity profile	$0 < z < 200$ m	6 g$_{water}$ kg$_{air}^{-1}$
	$200 < z < 2560$ m	3 g$_{water}$ kg$_{air}^{-1}$

Surface layout	
Patches, (P_x, P_y)	(50, 1)
$0 < P_x < 21$	Forest surface
$20 < P_x < 31$	River surface
$30 < P_x < 51$	Forest surface

Surface types		
	Forest surface	River surface
Roughness length momentum	0.1 m	0.001 m
Roughness length heat	0.1 m	0.001 m
Initial surface temperature	303 K	298 K
Albedo	0.15	0.07
Vegetation resistance	50 s m^{-1}	1×10^{-4} s m^{-1}
Prescribed kinematic temperature flux	0.15 K m s^{-1}	7.5×10^{-3} K m s^{-1}
Prescribed kinematic moisture flux	1×10^{-4} kg kg^{-1} m s^{-1}	1.3×10^{-4} kg kg^{-1} m s^{-1}

4.3   Results and discussion

4.3.1   Model validation

The simulation results of meteorological parameters are shown in Figure 4-2. The simulated surface air temperature at steady state was below 302 K for the river and above

304 K for the forest, within the range reported in the literature for the Rio Negro and nearby forests (Santos et al. 2019). The overall ambient air temperature gradient above the river and the forest was 2 to 3 K (Figure 4-2a).

Model simulations captured the main features of river winds. The transition height where rapid change in wind direction occurred was simulated as 260 m above the river (Figure 4-2b), consistent with the field observations (see chapter 3, Figure 3-8). The simulated wind speed was 1 to 3 m s^{-1}, and there was a local wind minimum observed at the transition height in line with field measurements.
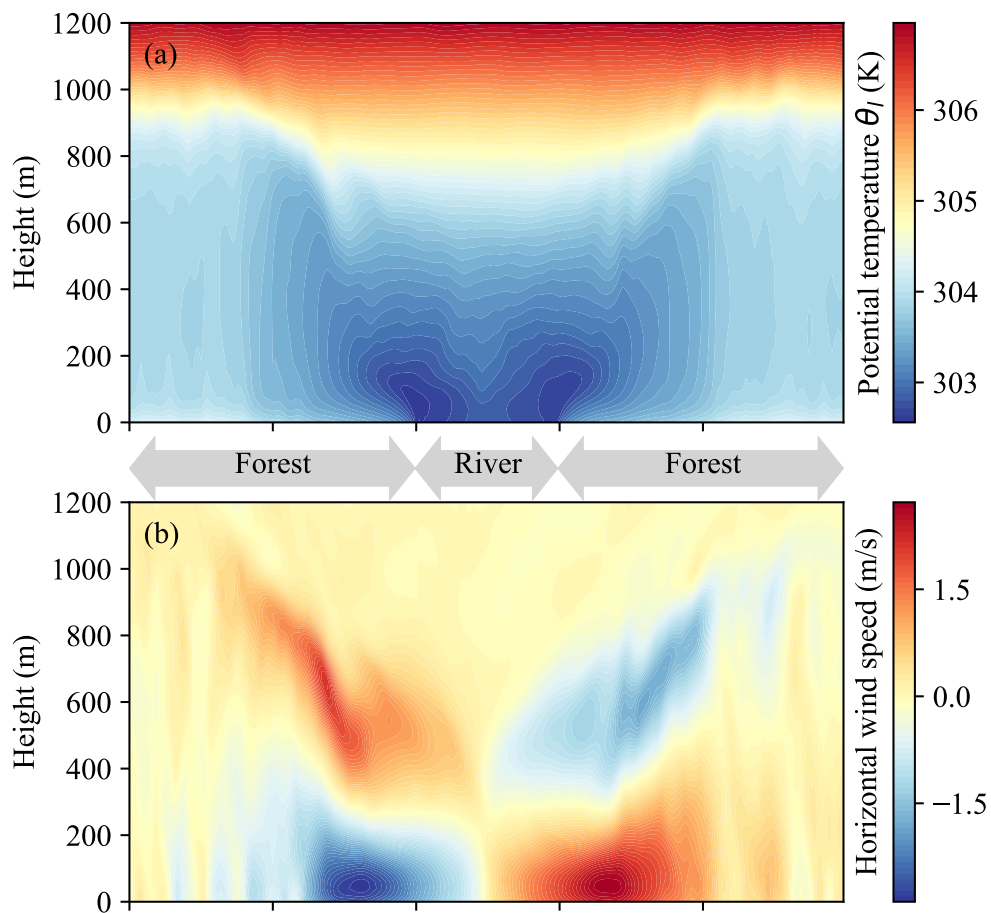
Figure 4-2. Simulation results of meteorological parameters in the presence of river winds. Vertical cross section of (a) simulated potential temperature and (b) simulated horizontal wind speed.

Simulations show that the influence of river winds can extend 5 km horizontally towards the forests (Figure 4-2a and b). The river width was set as 5 km in the DALES simulations. This horizontal influence is expected to increase with increasing river width. As an example, the influence of the thermally induced river winds can extend as far as 20 km inland for a river width of 20 km (Oliveira and Fitzjarrald 1994).

4.3.2 Impact of river winds on chemical transport

Atmospheric recirculation of local emissions was explored quantitatively within a large eddy simulation (LES). The setup and parameters were constructed as an idealized counterpart to the actual conditions of cluster 1 (chapter 3) in the absence of synoptic winds (Heus et al. 2010, Ouwersloot et al. 2011). In the idealized simulation, CO was continuously emitted from a nearby point source on land. The results also hold for tracers other than CO if they have an atmospheric lifetime that also exceeds the transport time through the circulation cell. The simulation represented an idealized treatment of many local factors as a strategy for gaining insight into the governing processes and the quantitative extent of slowed pollutant dispersion for the nearby human population.

A baseline LES was run for a homogeneous landscape of a forest in the absence of a river (Figure 4-3a). For this reference simulation, the pollution from the point source was transported upward, there was no recirculation back to the surface, and the pollution was dispersed by dilution and entrainment away from the riparian zone of human settlement. An experiment LES was conducted by altering the landscape to include a river (Figure 4-3b). For this simulation, a thermally driven closed sub-cell of strong local circulatory flows formed over the river-forest landscape. The pollution was carried

upward in this sub-cell over the land, mixed toward the middle of the river, and recirculated back to the nearby surface (Figure 4-3b).
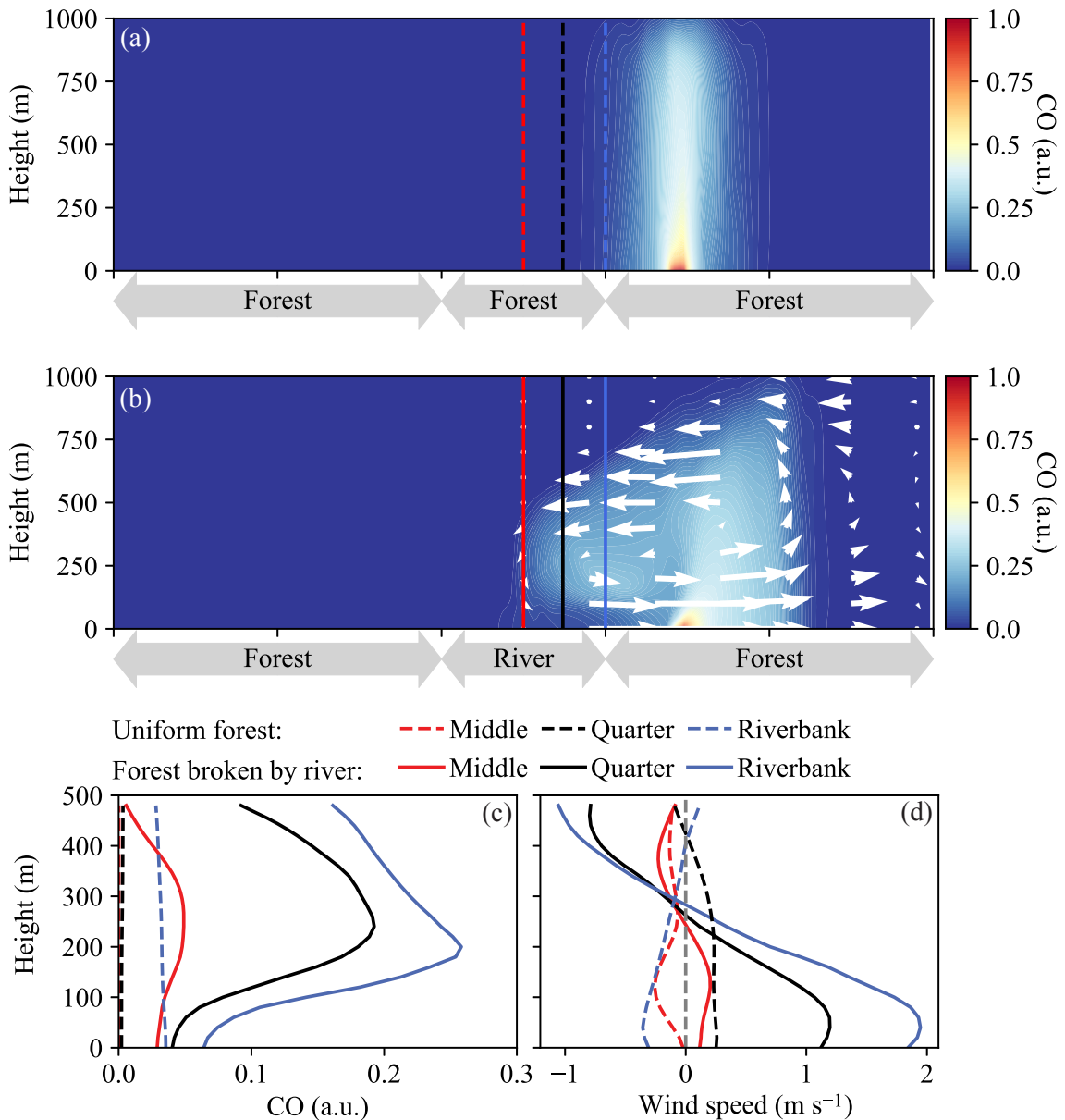
Figure 4-3. Large eddy simulation (LES) of river winds. The simulation ran for 3 h, and the results were averaged over the last hour. (a) Forested landscape. (b) Forested landscape broken by a river of 5-km width. White arrows depict the simulated wind field. (c) Vertical profiles of normalized CO concentration (CO, a.u.). Profiles over the riverbank, 25% across the river, and 50% across the river are represented by blue, black, and red lines, respectively. Dashed and solid lines represent the results for the landscapes of

panels *a* and *b*, respectively. (d) Vertical profiles of wind speed (m s^{-1}). Positive values of wind speed

represent a wind direction from the middle of the river toward the forest.

Vertical profiles at 25% and 50% along the horizontal transect of the river were

used to simulate UAV sampling. The pollution concentration reached a maximum value

at mid-height (Figure 4-3c, solid lines). This simulated behavior is consistent with the

observations (Chapter 3, Figure 3-13). Vertical profiles of the horizontal speeds of the

simulated river winds are plotted in Figure 4-3d. The maximum of the simulated speed

was 2 m s^{-1}, and its direction flipped at approximately 250 m. Both simulation results are

in good agreement with the observations for cluster 1 (Chapter 3, Figure 3-4). The LES-

simulated maximum height of the sub-cell of the river winds also agreed with an earlier

parameterized treatment within a Eulerian chemical transport model (Medeiros et al.

2018).

Recirculation to the surface riparian zone rather than transport away from it

implies greater air pollution in the zone of human settlement. The extent of increased air

pollution due to reduced pollutant dispersion was assessed in the simulation by taking a

vertical profile at the riverbank. In the simulation, the pollution concentration at the

riverbank approximately doubled in the presence compared to in the absence of the LES-

simulated recirculation (Figure 4-3c, blue lines).

The result presented here agrees with previous WRF-Chem modelling result on

height of the river breeze circulation cell (Medeiros et al. 2018). For trace air pollutant

transportation, the two results complimented each other on different scales. The LES

result herein focused on the emission sources nearby (within 10 km) while the WRF-

Chem model mainly studied the impact on Manaus plume dispersion on a larger scaled

(10 ~ 100 km). WRF-Chem simulation and the airborne measurement (above 500 m) from GoAmazon studies revealed that the river breeze in the studied region was not strong enough to alternate the mesoscale pollution dispersion.
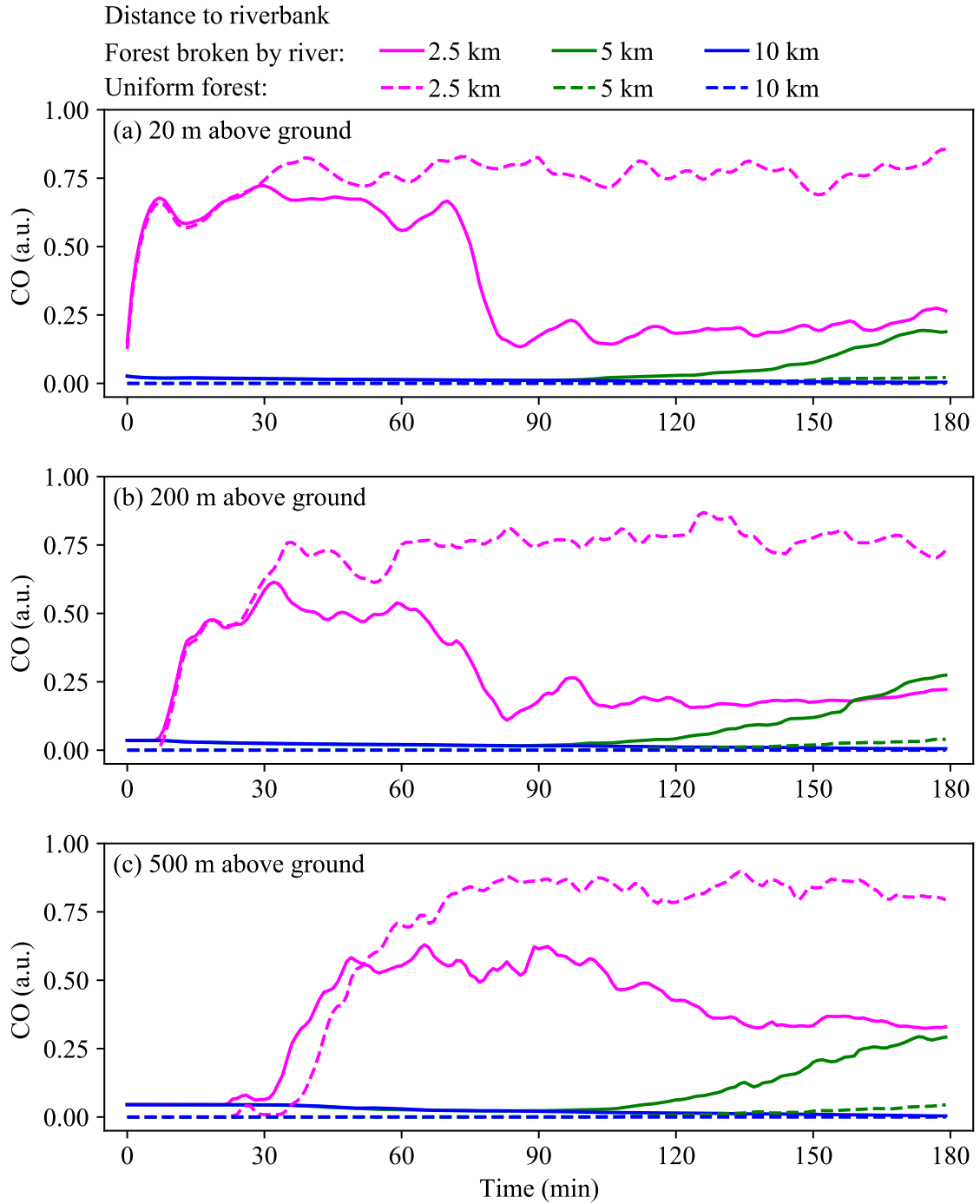
Figure 4-4. Time series of virtual tower measurements on the riverbank for simulation shown in Figure 4-3. Three different heights were selected for comparison, including (a) 20 m, (b) 200 m and (c) 500 m. Different colors represent distance of the tower location from the riverbank. The point source is 2.5 km from the riverbank and is on the same side with all the virtual towers. Solid lines and dashed lines represent different scenarios for the presence and absence of river, respectively.

To better understand the impact of river winds on interpretation of tower measurement, a set of virtual measurement results is shown in Figure 4-4. The impact of river winds only extend to about 5 km (approximately the width of the river) away from the riverbank, consistent with the result shown in Figure 4-2 and Figure 4-3. For virtual measurement results that are 10 km away from the riverbank, which is beyond the impact range of river winds, there is no different between homogeneous and heterogeneous landscape, no matter the height of the measurement. For virtual measurement results that are 5 km away from the riverbank, river winds promote the chemical transport, and the impact of increasing concentration is present at all heights as shown in Figure 4-4. There is no obvious difference between the impact of different heights. For virtual measurement results that are 2.5 km away from the riverbank, i.e. right at the point source, river winds dilute the pollution once developed. The decrease of concentration is observed at all heights shown in Figure 4-4 and the difference between homogeneous and heterogeneous landscape is more significant at lower altitude. Impacts of river winds on pollutant recirculation strongly depend on the riparian location of the measurement and tower measurement adjacent to large water bodies should take the impact of local circulation into consideration.

4.4   Conclusion

River winds caused by thermal contrast among heterogeneous terrain in the extensive Amazon river-forest landscape significantly impact atmospheric chemical transport in the riparian ecoregion. In this study, the role of river winds was investigated for chemical transport using numerical modelling tools. The simulation results highlighted the potential impact of river breeze and other microscale local circulations (within 10 km horizontally and 500 m vertically) is rather significant. River winds can play an important role on the dispersion of air pollutants (CO) and important atmospheric oxidants (O_3). Such circulation, although negligible at higher altitude, might amplify the impact of anthropogenic pollutions by extending their affecting area and residence time.

The impacts of river winds on chemical transport in the riparian region also depend on other factors such as the strength of synoptic-scale trade winds, which is not included in the scope of this chapter. More details about the effect of parallel and perpendicular trade winds on river winds can be found in (Ye et al. 2021). Further studies on decoupling the effect of different factors, such as insolation and topography, on the development of river winds are needed.

The effects of river winds on chemical transport are relevant to air quality and public health in the Amazon basin. The linkages should be carefully considered and included in atmospheric models to better represent the transport and evolution of pollution in riparian regions. The results and implications presented here are also applicable to other gaseous pollutants of similar atmospheric lifetime that originate from biogenic and anthropogenic sources nearby the rivers during times of thermal heterogeneity across the landscape. Impacts of river winds on the dispersion air pollutants

with different atmospheric lifetimes and transporting behaviors should be further studied

and understood.

5   Conclusions

Tropical regions exert dominant impacts on global circulations of energy, moisture and oxidants. Advance in sensing technology and unmanned aerial vehicles empowers the high-resolution atmospheric measurement in challenging environments like tropical rainforests. Important phenomenon happening at intermediate scales can be better understood with these new capabilities. This dissertation investigated the potential of low-cost air sensors for trace level atmospheric sensing and the application of commercial meteorological and chemical sensors for river winds observation. The observational data set was used in a simplified LES study and can be used for further model studies to gain better knowledge in controlling factors and impacts of thermally driven circulations.

In chapter 2, commercial metal oxide sensors were assembled in a sensor array and evaluated for sensitivity, stability, and selectivity for quantification of trace level biogenic volatile organic compounds. Detection limit, an important benchmark for sensitivity, was improved to 1.5 ppb for isoprene by optimizing the controlling electronics and operation temperature. Stability and selectivity were evaluated for standalone sensor system in laboratory dry conditions. Calibrations under different humidity conditions were conducted to correct sensor response in changing humidity. Mixed matrix membrane was placed in front of the sensor system to improve selectivity towards isoprene against α-pinene and a differentiating factor of 8 was achieved.

In chapter 3, the first in-situ daytime vertical profile data set for river winds in the central Amazonia collected by UAVs were presented. Meteorological variables, such as wind speed and wind direction, and chemical species, such as carbon monoxide and total oxidants, were analyzed using fuzzy c-means clustering. Four clusters were identified, including different scenarios of strong river winds, strong synoptic scale wind, weak to perturbed river winds and other complications. The favorable conditions for river winds development were weak synoptic scale wind (< 4 m s^{-1}) and strong thermal contrast, i.e. no high-altitude clouds. River winds can be attenuated or completely overwhelmed depending on the background weather conditions. The impacts of river winds on pollutant recirculation were investigated by taking CO and O_x measurement as proxies.

In chapter 4, pollutant recirculation induced by river winds were explored through numerical modelling tools. LES modelling for river winds were validated with observational evidence. The modelled transition height of river wind circulations is within the observed range of $150 - 300$ m. Impacts of river winds on pollutant dispersion were found to be dependent on location and altitude, which should be considered carefully for interpretation and extrapolation of tower measurement results. Further analysis on dominating factors of river wind strength, such as thermal contrast and background wind field, should be better understood from observational and modelling perspective to advise on the real impacts of river winds on the riparian human settlements.

There are still limitations in measurement by low-cost sensors, which should not be ignored when used to draw scientific conclusions. The response time of BVOC selective sensing system does not meet the requirement of real time field deployment yet. Even for

commercial sensors with fast response, the drift of baseline and sensitivity is still a major

concern when aiming for accurate quantification. Except for the limitations from the

sensor side, there are also constraints from the UAV. The size of UAV data set is

relatively small due to the limited flight time and the turbulence induced by UAV can

have some impacts on the measurement result. Therefore, more efforts should be taken to

improve the accuracy and confidence of measurement results collected by low-cost

sensors onboard UAVs.

Appendix A: Optimization of mixed matrix membranes

The selectivity performance of the mixed matrix membrane for volatile organic compounds depends on MOF weight loading, membrane thickness and morphology of the MOF particles. MOF filler materials typically increase the permeability of a membrane while the selectivity varies depending on the characteristics of the pairs for separation. Increasing the weight loading of MOF faces the trade-off between larger improvement in permeability and a higher chance of interfacial void defects. The interfacial void defects, when present, eliminate the selective separation due to the uncontrolled structure. The performance of 6FDA-DAM / HKUST-1 mixed matrix membranes was examined for the factors mentioned above.

Figure A-1a shows the impact of thermal activation on permeability and selectivity. Thermal activation at 150 °C under vacuum can effectively remove the residual solvent and clear any blockage of the pore structure in MOF. This clearance opens the door for faster permeation.
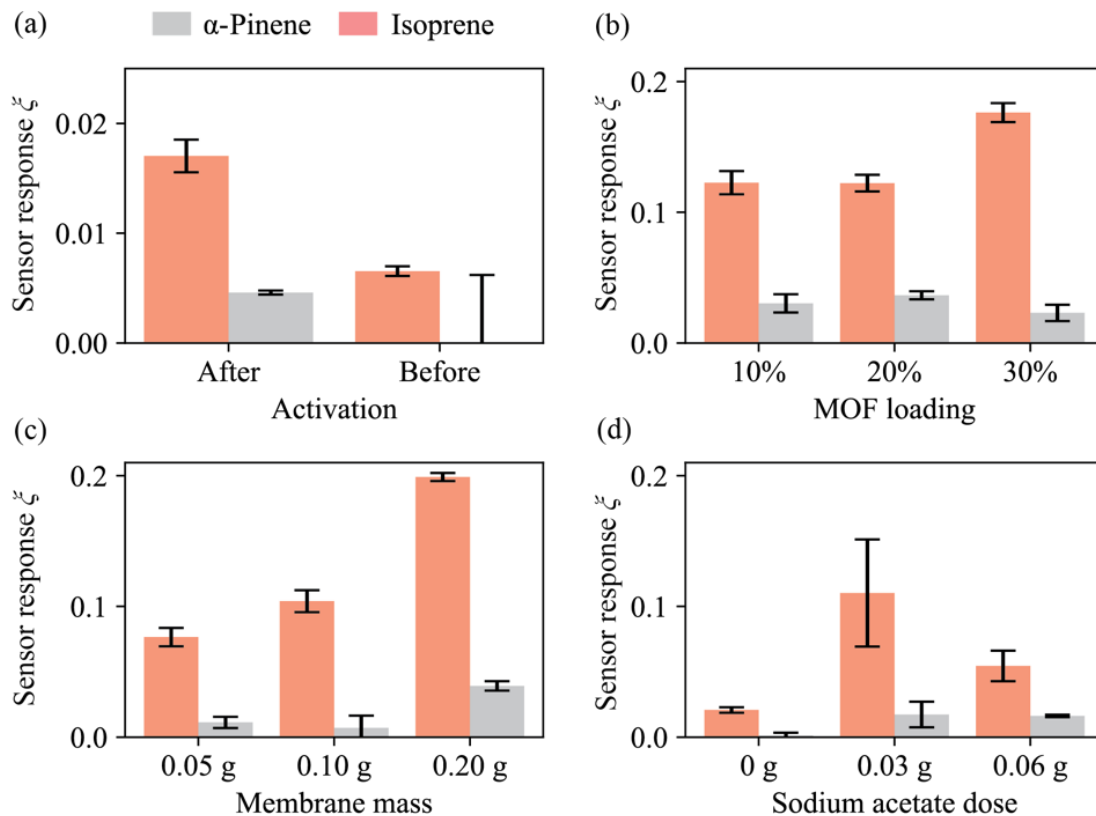
Figure A-1. (a) Selectivity comparison ranging from MOF weight loading of 10%, 20%, and 30%. (b) Selectivity comparison ranging from membrane casting mass of 0.05 g, 0.10 g, and 0.20 g. (c) Selectivity comparison for bulk and branched MOF particles. (d) Selectivity comparison for membranes before and after thermal activation.

Figure A-1b shows comparison of sensor response after the mixed matrix membrane for MOF weight loadings of 10%, 20%, and 30%. Increasing the MOF weight loading from 10% to 30% led to a 50% increase in after-membrane response to isoprene. It also doubled the selectivity of isoprene over α-pinene. The membrane preparation minimized the interfacial void defect within the weight loading range of 0 to 30%. The membranes were tested in a standard gas permeation system (Maxwell Robotics) for comparison with literature (Chi et al. 2019). The comparable selectivity for small gas molecules indicated that the membranes did not have significant interfacial voids (Table

A-1). The increase in selectivity with weight loading can be attributed to the weaker interaction between isoprene and HKUST-1 and thus the higher permeability towards isoprene in comparison to pinene.

Table A-1. Comparison in permeability between this study and literature. Pure gas permeation experiments for small gas molecules were performed on an automated pure-gas permeation systems (Maxwell Robotics) of constant volume and variable pressure.

	$P(CO_2)/$ $P(CH_4)$	$P(CO_2)/$ $P(N_2)$	$P(H_2)/$ $P(CH_4)$	$P(H_2)/$ $P(N_2)$	$P(O_2)/$ $P(N_2)$	Data source
6FDA-DAM	19.9±1.1	17.7±0.9	13.1±0.7	11.7±0.6	3.3±0.2	Chi et al., 2019
6FDA-DAM	21.5	21.8	12.6	12.8	3.2	This study
30% MMM (branched)	16.5±0.8	16.3±0.8	10.1±0.5	10.0±0.5	3.0±0.1	Chi et al., 2019
30% MMM (branched)	14.0	15.8	8.4	9.4	2.9	This study

Figure A-1c shows the comparison for response and selectivity for different membrane thicknesses at 30% MOF weight loading. Thinning the membrane did not change the response or the selectivity. However, thickening the membrane led to a doubled sensor response for isoprene and more than a tripled response for α-pinene. There is thus a slight decrease in the selectivity. The thicker membrane is more likely to

have interfacial defects, which might lead to the increasing permeability for both species. The membranes within the range of adjustment are relatively thick and the dependence of membrane performance on membrane thickness is not expected in this range.
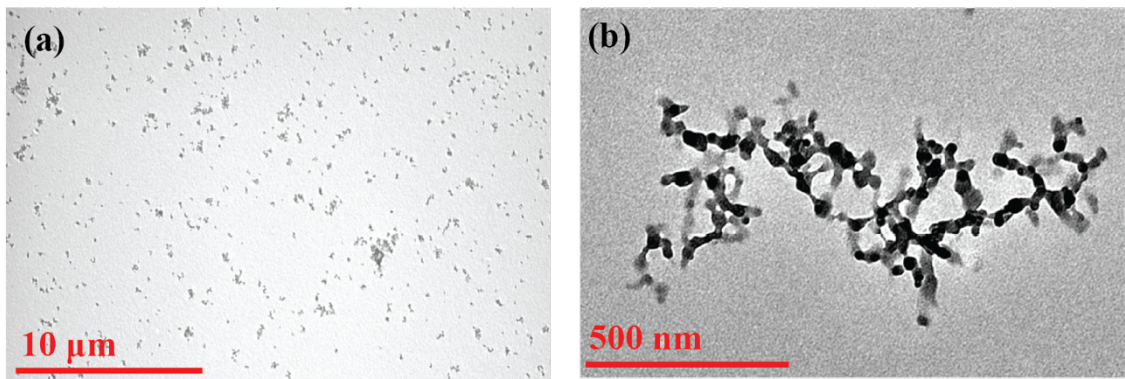
Figure A-2. TEM results of MOF nanoparticles at different scales

Figure A-1d shows the separation performance of membranes containing MOF particles of different sizes. The addition of sodium acetate was used to control the morphology and size of the MOF fillers through coordination modulation. The branched MOF fillers, synthesized with addition of sodium acetate, tend to have better permeation and separation performance compared with the bulk MOF crystals. TEM pictures of branched MOF fillers are shown in Figure A-2.

Appendix B: Details about UAV data set

B-1. Chemical sensing system calibration and correction

The calibration for the chemical sensing system was performed from 1 to 10 July 2019, in Songshan, Taiwan (121.5780° E, 25.0510° N), co-located to the Songshan Environment Protection Administration (EPA) station. For calibration, the minute-averaged outputs (mV) from each sensor were compared with the minute-averaged data from the station (Figure A-3).
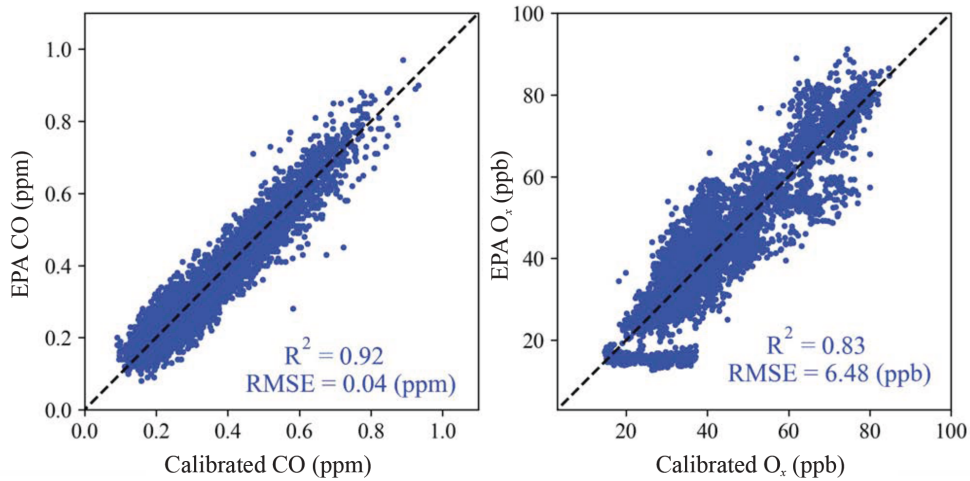
Figure A-3. Calibration of chemical sensors

The concentration as a function of sensor output V (mV) and temperature T (°C) was expressed as follows:

$$[X] = a\,V + b\,T + c \qquad \text{(Eq. A-1)}$$

where [X] is the mixing ratio (ppmv for CO; ppbv for O_x). The parameter values *a*, *b*, and *c* are listed in Table A-2. The coefficient R^2 of determination based on the variance between the calibrated concentration and the reference data set approached 0.7 for O_x and 0.9 for CO.

Table A-2. Fitting parameters used in Eq. A-1. The coefficient R2 of determination represents the proportion of the variance in the data set explained by Eq. A-1.

Fitting parameters	*a*	*b*	*c*	R^2
O_x	4.56	2.34	-63.45	0.72
CO	0.00	0.00	-0.04	0.90

B-2. Quality control for chemical profiles

For the chemical sensing system, two sets of quality-control criteria were applied to the data sets, as follows:

1. Doubly recorded temperature provided an important diagnostic of overall sensing performance. One temperature sensor was located in the meteorological package separate from the package of chemical sensors, and one temperature sensor was located within the same package as the chemical sensor. During the daytime, atmospheric temperature decreased with height. For sufficient mixing throughout the flight, the time series of temperature should reach a minimum temperature at 500 m for an altitude range of 0 to 500 m. However, an examination of the temperature time series showed that for some flights there was a lag in the temperature minimum within the package of chemical sensors, meaning that there was a time difference between maximum altitude and minimum temperature. The effect arose from poor

mixing within in the chemical sensor package. In comparison, the meteorological sensor did change linearly with altitude without this lag. This comparative result indicates that the chemical sensor package had technical issues related to internal mixing of air for those flights. Data sets of flights for which the temperature lagged longer than 2 min were excluded from further chemical analysis.

2. Under ideal conditions, the profiles of all the species measured through the flight should be symmetric for ascending and descending legs provided that the atmosphere does not change appreciably in a period of 15 min. In the observations, however, the two data sets did not mirror each other exactly, in part because the descent was three times faster due to a UAV battery constraint. Even so, similar trends are expected when the sensing system functions correctly. Therefore, a symmetry check was a basic data quality control step. For some flights, there were asymmetric temperature and chemical species profiles between the ascending and descending legs. This difference was possibly related to a time lag caused by poor mixing within the sensor package, among other factors (e.g., changed air mass). For a scientifically conservative analysis, only data sets having numerically similar values on the ascending and descending legs were included in the analysis. Because the rate of ascent was slower than that of descent, allowing more effective time for measurement at each altitude during ascent, the ascending rather than the descending profiles were used in the analysis.

After application of the two sets of quality-control criteria, the raw data set of 56 vertical profiles was reduced to a refined data set 25 profiles.

B-3. Details about UAV flights

Detailed information about 56 UAV flights of which data were used in chapter 3 is presented in Table A-3. Start time of the flight was presented in local time (LT), which is 4 h earlier than UTC. Each flight took about 12 min to complete, including launch and recovery. Cluster number corresponds to the dominant degree of membership as determined from the meteorological clustering analysis in chapter 3. Chemical profiles were denoted as "Y"es if meeting the quality control criteria. The strength of synoptic scale wind can be reflected by wind speed at 500 m, which is an average across 450 m to 500 m. The thermal contrast between the land and the water body depends on the strength of the solar radiation, and thus the cloudiness over the interested region. Fair weather days with few clouds tend to favor a more significant thermal contrast. Satellite images of cloud cover are grouped into several categories, as follows: (Ia) a fair-weather day having cumulus clouds over the land and no clouds over the river; (Ib) a fair-weather day having few clouds over both land and river; (II) cirrus and high-altitude stratus clouds; and (III) heavy clouds suggestive of inclement weather. Flights having no clear satellite images within a two-hour timeframe of the flight (09:30 - 11:30 for Terra and 12:30 - 14:30 for Aqua and Suomi) are marked by "-" in the table.

Table A-3. List of UAV flights.

Index	Date	Time (LT)[1]	Cluster[2]	Efficient mixing[3]	Wind speed at 500 m (m s^{-1})[4]	*Terra*	*Aqua*	*Suomi*
1	20190911	15:52	3	Y	4	-	-	-
2	20190912	17:05	2	Y	7	-	-	-

Appendix B: Details about UAV data set

Index	Date	Time (LT)[1]	Cluster[2]	Efficient mixing[3]	Wind speed at 500 m (m s^{-1})[4]	Terra	Aqua	Suomi
3	20190913	11:11	2	Y	8	-	-	-
4	20190913	12:11	2	Y	7	-	-	-
5	20190913	13:11	2	Y	6	-	-	I(a)
6	20190913	14:09	2	Y	6	-	-	I(a)
7	20190913	15:01	2	Y	6	-	-	-
8	20190913	16:01	2	Y	5	-	-	-
9	20190916	11:32	4	Y	3	II	-	-
10	20190917	11:21	1	N	2	II	-	-
11	20190918	11:01	4	Y	3	I(b)	-	-
12	20190918	12:36	4	N	2	-	III	III
13	20190918	14:07	4	N	1	-	III	III
14	20190918	15:10	4	N	1	-	-	-
15	20190923	11:11	1	N	1	II	-	-
16	20190923	12:41	4	N	2	-	II	II
17	20190923	14:28	4	N	2	-	-	-
18	20190923	15:17	4	N	2	-	-	-
19	20190923	16:07	4	N	2	-	-	-
20	20190924	10:23	3	N	2	I(a)	-	-

Appendix B: Details about UAV data set

Index	Date	Time (LT)[1]	Cluster[2]	Efficient mixing[3]	Wind speed at 500 m (m s^{-1})[4]	Terra	Aqua	Suomi
21	20190924	11:21	1	N	2	I(a)	-	-
22	20190924	12:26	1	N	2	-	-	-
23	20190924	14:05	3	Y	4	-	II	II
24	20190925	10:33	3	N	2	I(a)	-	-
25	20190925	13:31	4	N	2	-	III	III
26	20190925	14:30	4	N	3	-	III	III
27	20190926	10:27	1	N	4	II	-	-
28	20190926	11:16	1	N	2	II	-	-
29	20190926	12:03	1	N	2	-	-	-
30	20190926	13:42	1	Y	3	-	I(a)	I(a)
31	20190926	14:24	1	N	2	-	I(a)	I(a)
32	20190927	10:23	1	N	2	II	-	-
33	20190927	11:20	1	Y	3	II	-	-
34	20190927	12:10	4	N	1	-	-	-
35	20190930	10:40	2	Y	7	I(a)	-	-
36	20190930	11:33	2	Y	6	I(a)	-	-
37	20190930	12:25	2	Y	6	-	-	-
38	20190930	13:39	3	N	3	-	I(a)	I(a)

Appendix B: Details about UAV data set

Index	Date	Time (LT)[1]	Cluster[2]	Efficient mixing[3]	Wind speed at 500 m (m s^{-1})[4]	Terra	Aqua	Suomi
39	20190930	14:26	2	Y	6	-	I(a)	I(a)
40	20191001	10:30	3	Y	4	-	-	-
41	20191001	11:20	3	Y	4	-	-	-
42	20191001	12:12	3	Y	4	-	-	-
43	20191001	13:52	1	N	2	-	II	II
44	20191001	14:43	4	Y	2	-	-	-
45	20191007	11:04	3	Y	2	I(a)	-	-
46	20191007	12:22	3	Y	4	-	-	-
47	20191007	13:53	1	Y	3	-	I(b)	I(b)
48	20191007	15:09	3	N	3	-	-	-
49	20191008	10:24	4	N	4	-	-	-
50	20191008	11:13	4	N	3	-	-	-
51	20191008	12:20	4	N	4	-	-	-
52	20191008	12:47	4	N	3	-	III	III
53	20191009	10:57	3	Y	5	I(b)	-	-
54	20191009	13:30	2	N	4	-	II	III
55	20191009	14:25	3	N	4	-	II	III
56	20191009	15:37	3	N	2	-	-	-

B-4. Determination of cluster counts for fuzzy c-means clustering

The traditional optimization of fuzzy c-means clustering involves the maximization of fuzzy partition coefficient, which is inversely corelated to the cluster distance. The fuzzy partition coefficient ranges from 0 to 1 by definition, for which 1 is the best clustering. The coefficient is a metric of the quality of the data clustering described by a certain model. Due to the limited size of the dataset (56 profiles) and the high dimensionality of the input variable (i.e., 1000 dimensions), the intrinsic optimization parameter could not be fully objectively automated (Figure A-4). Additional information was needed to determine the most representative cluster count.
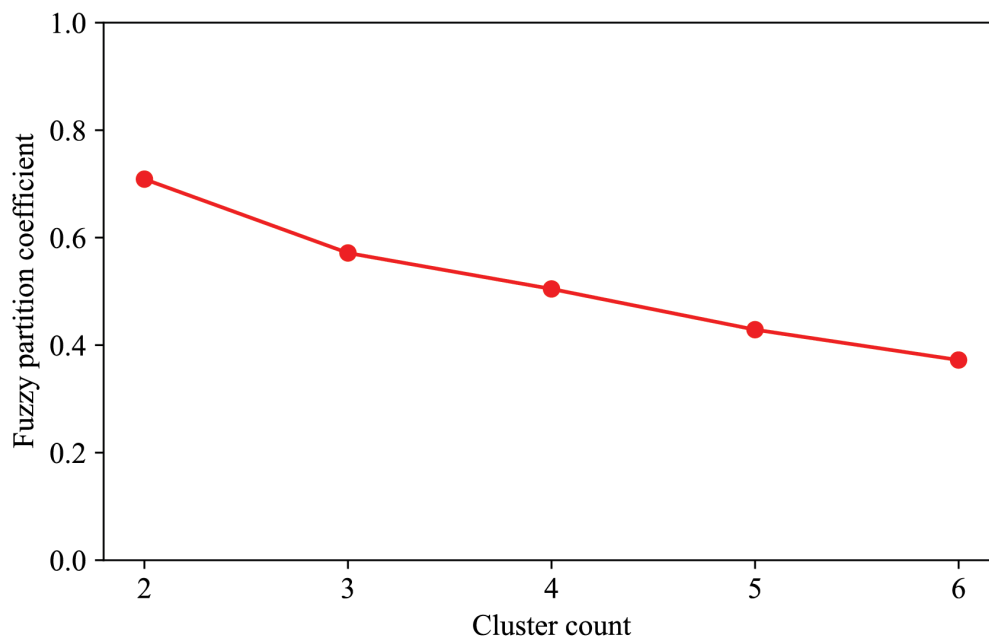
Figure A-4. Values of the fuzzy partition coefficient of the FCM analysis plotted against the number of clusters.

For this purpose, cluster counts from 2 to 6 were tested. The cluster centroids are shown in Figure A-5.
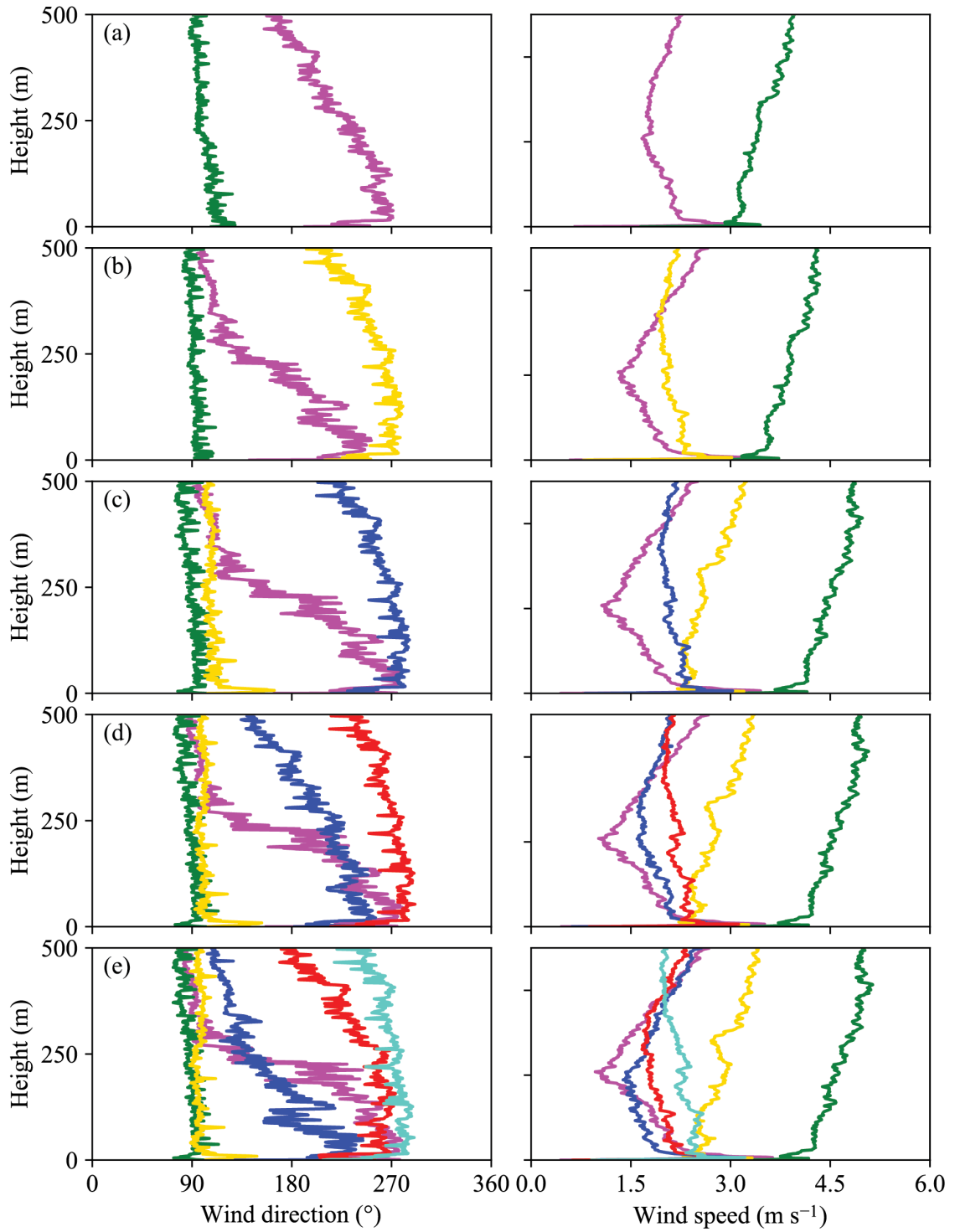
Figure A-5. Dependence of the cluster centroids from the FCM analysis on the number of clusters: (a) two clusters, (b) three clusters, (c) four clusters, (d) five clusters, and (e) six clusters.

For an increase in cluster counts from 2 to 4, clusters were stepwise separated that represented strong local circulatory flows of river winds, no apparent circulatory flow (i.e., flow over river appears same as over forest), weak to perturbed local circulatory flows of river winds, and other types of flows. Further increasing the cluster count split the final cluster. This splitting was not relevant to the focus of the present study, and the cluster count was chosen as 4 for the most meaningful interpretation.

B-5. Details about sensing system on the UAV.

During the 2019 boat campaign, the chemical sensing system deployed on the UAV had more sensors other than CO and O_x discussed in chapter 3. The detailed sensor configurations are listed in Table A-4.

Table A-4. Complete sensor configuration for the chemical sensing system. All sensors were purchased from Alphasense Co.

Sensor model	Species
IRC-A1	Carbon dioxide
CO-B4	Carbon monoxide
NO-B4	Nitric oxide
NO2-B42F	Nitrogen dioxide
Ox-B421	Ozone and nitrogen dioxide
SO2-B4	Sulfur dioxide
PID-AH2	Total volatile organic compounds
OPC-N2	Particulate matter
BMP280	Pressure
HTU21D	Temperature and relative humidity

For physical parameters measurement, vertical profiles of relative humidity and temperature were analyzed for typical days dominated by strong trade winds (Figure A-6a) and well-developed river winds (Figure A-6b), respectively. The derived parameters, such as absolute humidity and potential temperature, were also plotted. Absolute humidity ρ_v and potential temperature θ_l are calculated from temperature and relative humidity using Eq A-2 and Eq A-3.

$$\rho_v = 6.112 \times \exp\left(\frac{17.67 \times T}{T+243.5} \times \frac{RH \times 2.1674}{273.15+T}\right), \qquad \text{Eq A-2}$$

where T is temperature (unit: °C) and RH is relative humidity ranged between 0 and 1.

$$\theta_l = (273.15 + T) \times \left(\frac{P_0}{P}\right)^{\frac{R}{c_p}}, \qquad \text{Eq A-3}$$

where T is temperature measured at certain height (unit: °C), P_0 is pressure at surface level (unit: hPa), and P is pressure measured at same height as temperature (unit: hPa). R is the gas constant of air, and c_p is the specific heat capacity at a constant pressure. $R/c_p = 0.286$ for air.
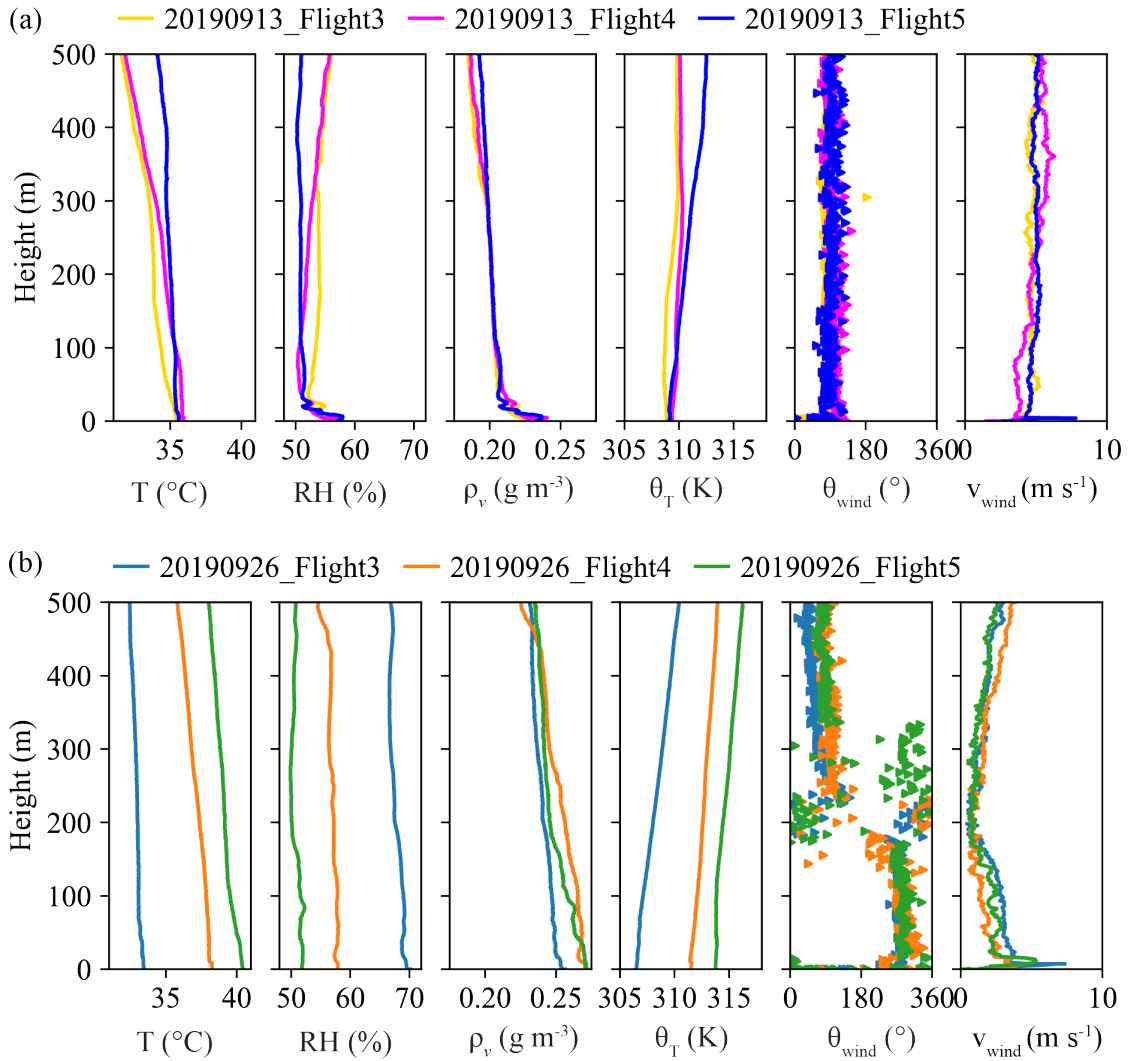
Figure A-6. Vertical profiles of physical parameters from river surface to 500 m for UAV flights on days (a) when trade winds prevail, (b) when river winds prevail.

For flights collected when river winds prevail, temperature tends to be higher and has smaller vertical gradient compared with flights dominated by strong trade winds. There is no obvious difference between the relative humidity profiles between the two groups. Despite the expected relative humidity change brought by river winds, it was not reflected in the data set collected by low-cost sensors (van Heerwaarden and de Arellano 2008). For the derived absolute humidity and potential temperature, the patterns stay

consistent with the raw data.

Among different chemical sensor measurements, electrochemical sensors for CO, O_x, NO, and NO_2 have observed interesting patterns. For other compounds that were measured by the chemical sensing system, such as CO_2, SO_2, total volatile organic compounds, and particulate matters, did not show meaningful data patterns due to the large noise. The scaled concentrations of CO, O_x, NO, and NO_2 are plotted as a function of altitude (i.e., vertical profiles) in Figure A-7. The vertical profiles of wind speed and wind direction are also plotted. The profiles were recorded from 10:00 to 17:00 (LT) on 13 Sep 2019. The wind direction was dominated by easterlies characteristic of the equatorial trade winds, and the wind speed was typically larger than 5 m s^{-1}. It was a typical fair-weather day without overhead clouds.

Figure A-7. Vertical profiles of chemical species from river surface to 500 m for UAV flights on days when trade wind prevails. Data were collected from 10:00 to 17:00 (local time) on 13 September 2019. A wind direction of 0° is North.

Decreasing CO concentration with height was expected from previous studies in the tropical region, albeit over forest rather than river landscapes (Sachse et al. 1988,

Andreae et al. 2012). These trends, as examples of well-mixed conditions, can be considered in the context of the regional sources of CO. In the Amazon region, the background CO concentration is maintained by the photooxidation process of VOCs. Additional CO sources include surface emissions such as incomplete combustion from industry, transportation, and biomass burning.

For NO and NO_2, the background concentration in the Amazon region is usually less than 0.5 ± 0.3 ppb of NO_y (Bakwin et al. 1990, Liu et al. 2016). These concentrations derive from soil emissions. However, this concentration is lower than the minimum limit of detection (MLD) of the sensor. By comparison, the NO and NO_2 concentrations observed in the vertical profiles are greater than the sensor MLD. The vertical profiles in Figure A-7 show that the NO_2 concentration increased with height, and the NO concentration was relatively high at the surface and decreased abruptly above 300 m. These NO_x profiles are the consequence of human activities, such as biomass burning and urban emissions.

Vertical profiles of increasing O_x concentrations with height were observed (Figure A-7). As an upper limiting, the O_x concentration is taken as the O_3 concentration. Mid-day values of ozone in this region in the dry season range from 20 to 60 ppb, and in the absence of substantial pollution the concentrations of NO_2 are considerably less. The forest canopy and river water surface can serve as a sink of dry deposition for ozone, leading to an increasing vertical profile for ozone.

For days when river winds prevail, there are some interesting features despite the limited qualified chemical profiles. These profiles were characterized by a mid-altitude change of CO, O_x, and NO_2 concentrations, as illustrated in Figure A-8. The height of

wind direction change aligned with the height at which the concentrations of the chemical species increased. Detailed explanation is available in chapter 3.
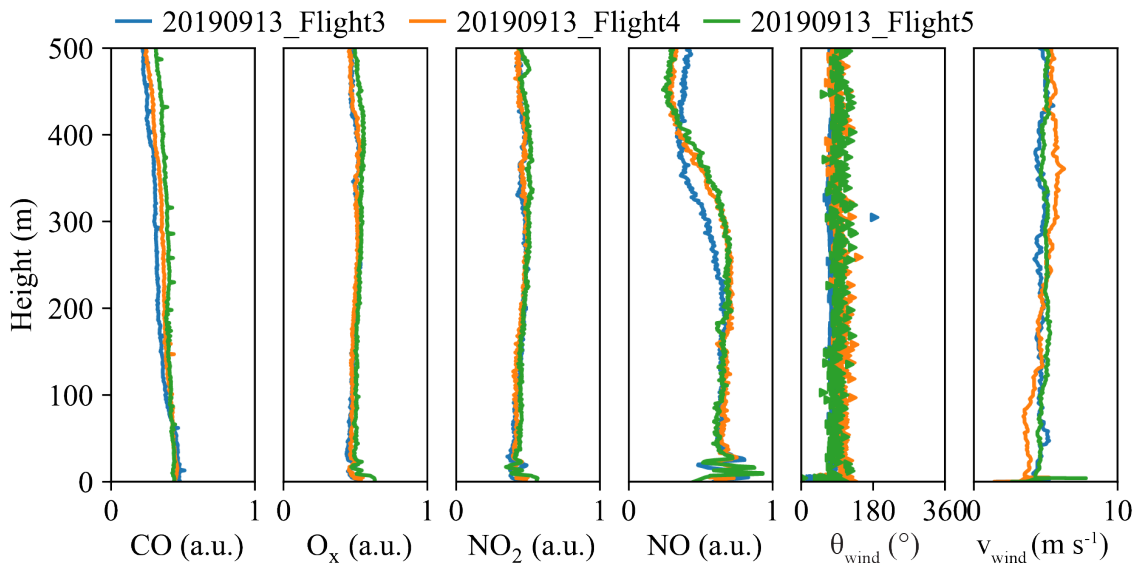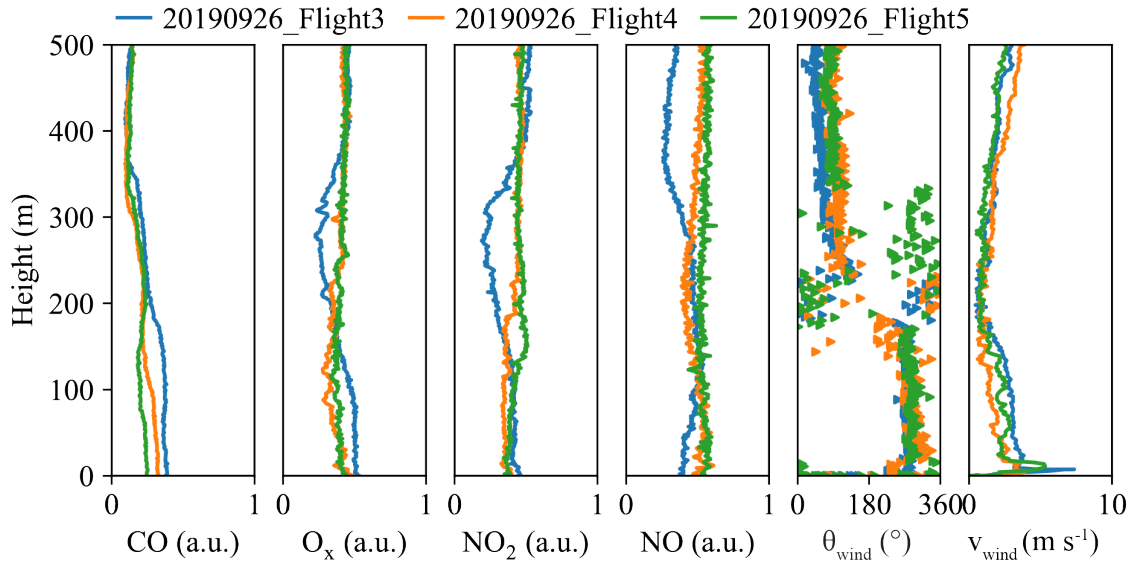

Figure A-8. Vertical profiles from river surface to 500 m for UAV flights on days when river winds prevail. Data were collected from 10:00 to 17:00 (local time) on 26 September 2019.

Bibliography

Alphasense (2021). "Alphasense metal oxide semiconductors product description." Retrieved Jun 14, 2021, 2021, from https://www.alphasense.com/products/metal-oxide-sensors/.

Amigo, I. (2020). "The Amazon's fragile future." Nature **578**(7796): 505-507.

ANA (2021). "Brazillian National Water Agency." Retrieved Jan 6, 2021, from https://www.gov.br/ana/pt-br.

Andreae, M. O., et al. (2015). "The Amazon Tall Tower Observatory (ATTO): overview of pilot measurements on ecosystem ecology, meteorology, trace gases, and aerosols." Atmospheric Chemistry and Physics **15**(18): 10723-10776.

Andreae, M. O., et al. (2012). "Carbon monoxide and related trace gases and aerosols over the Amazon Basin during the wet and dry seasons." Atmos. Chem. Phys. **12**(13): 6041-6065.

Andreae, M. O., et al. (2004). "Smoking rain clouds over the Amazon." Science **303**(5662): 1337-1342.

Atkinson, R. and J. Arey (2003). "Gas-phase tropospheric chemistry of biogenic volatile organic compounds: a review." Atmospheric Environment **37**: 197-219.

Avissar, R., et al. (2002). "The Large-Scale Biosphere-Atmosphere Experiment in Amazonia (LBA): Insights and future research needs." Journal of Geophysical Research **107**(D20).

Bakwin, P. S., et al. (1990). "Emission of nitric oxide (NO) from tropical forest soils and exchange of NO between the forest canopy and atmospheric boundary layers." Journal of Geophysical Research: Atmospheres **95**(D10): 16755-16764.

Bates, K. H. and D. J. Jacob (2019). "A new model mechanism for atmospheric oxidation of isoprene: global effects on oxidants, nitrogen oxides, organic products, and secondary organic aerosol." Atmospheric Chemistry and Physics **19**(14): 9613-9640.

Batista, C. E., et al. (2019). "Intermediate-scale horizontal isoprene concentrations in the near-canopy forest atmosphere and implications for emission heterogeneity." Proceedings of the National Academy of Sciences **116**(39): 19318-19323.

Bernardo, P., et al. (2009). "Membrane gas separation: a review/state of the art." Industrial & engineering chemistry research **48**(10): 4638-4663.

Betts, A., et al. (2009). "The Amazonian boundary layer and mesoscale circulations." Amazonia and global change. Geophysical monograph **186**.

Bezdek, J. C., et al. (1984). "FCM: The fuzzy c-means clustering algorithm." Computers & Geosciences **10**(2): 191-203.

Boisier, J. P., et al. (2015). "Projected strengthening of Amazonian dry season by constrained climate model simulations." Nature Climate Change **5**(7): 656-660.

Broedel, E., et al. (2017). "Simulation of surface fluxes in two distinct environments along a topographic gradient in a central Amazonian forest using the INtegrated LAND Surface Model." Hydrology and Earth System Sciences Discussions **2017**: 1-49.

Burgués, J. and S. Marco (2020). "Environmental chemical sensing using small drones: A review." Science of The Total Environment: 141172.

Butler, R. A. (2020). "10 Facts about the Amazon Rainforest in 2020." Retrieved Sep 15, 2021, from https://rainforests.mongabay.com/amazon/amazon-rainforest-facts.html.

Carneiro, R. G. and G. Fisch (2020). "Observational analysis of the daily cycle of the planetary boundary layer in the central Amazon during a non-El Niño year and El Niño year (GoAmazon project 2014/5)." Atmospheric Chemistry and Physics **20**(9): 5547-5558.

Chi, W. S., et al. (2019). "Mixed‐matrix membranes formed from multi‐dimensional metal–organic frameworks for enhanced gas transport and plasticization resistance." ChemSusChem.

Chung, T.-S., et al. (2007). "Mixed matrix membranes (MMMs) comprising organic polymers with dispersed inorganic fillers for gas separation." Progress in polymer science **32**(4): 483-507.

Crosman, E. T. and J. D. Horel (2010). "Sea and lake breezes: A review of numerical studies." Boundary-layer meteorology **137**(1): 1-29.

Cross, E. S., et al. (2017). "Use of electrochemical sensors for measurement of air pollution: correcting interference response and validating measurements." Atmospheric Measurement Techniques **10**(9): 3575.

David, L. M. and P. R. Nair (2011). "Diurnal and seasonal variability of surface ozone and NOx at a tropical coastal site: Association with mesoscale and synoptic meteorological conditions." Journal of Geophysical Research-Atmospheres **116**.

Davidson, E. A., et al. (2012). "The Amazon basin in transition." Nature **481**(7381): 321-328.

Davidson, E. A., et al. (2012). "The Amazon basin in transition." Nature **481**(7381): 321-328.

de Sa, S. S., et al. (2019). "Contributions of biomass-burning, urban, and biogenic emissions to the concentrations and light-absorbing properties of particulate matter in central Amazonia during the dry season." Atmospheric Chemistry and Physics **19**(12): 7973-8001.

de Souza, D. O., et al. (2016). "Urbanization effects on the microclimate of Manaus: A modeling study." Atmospheric Research **167**: 237-248.

Dias, M. S., et al. (2004). "River breeze circulation in eastern Amazonia: observations and modelling results." Theoretical and applied climatology **78**(1): 111-121.

Dos Santos, M. J., et al. (2014). "Influence of local circulations on wind, moisture, and precipitation close to Manaus City, Amazon Region, Brazil." Journal of Geophysical Research: Atmospheres **119**(23): 13,233-213,249.

Elmi, I., et al. (2008). "Development of ultra-low-power consumption MOX sensors with ppb-level VOC detection capabilities for emerging applications." Sensors and Actuators B: Chemical **135**(1): 342-351.

Fan, M., et al. (2020). "Comparison of aircraft measurements during GoAmazon2014/5 and ACRIDICON-CHUVA." Atmospheric Measurement Techniques **13**(2): 661-684.

Fang, M., et al. (2015). "ZIF-8/PDMS mixed matrix membranes for propane/nitrogen mixture separation: experimental result and permeation model validation." Journal of Membrane Science **474**: 103-113.

Farias, E. (2020). "Amazônia em Chamas 20: Fumaça das queimadas encobre Manaus." Retrieved Feb 26, 2021, from https://amazoniareal.com.br/amazonia-em-chamas-20-fumaca-das-queimadas-encobre-manaus-09-09-2020/.

Fitzjarrald, D. R., et al. (2008). "Spatial and temporal rainfall variability near the Amazon-Tapajós confluence." Journal of Geophysical Research: Biogeosciences **113**: G00B11.

Fitzjarrald, D. R., et al. (2008). "Spatial and temporal rainfall variability near the Amazon-Tapajós confluence." Journal of Geophysical Research **113**(G1).

Garg, A., et al. (2015). "Zebra GC: A mini gas chromatography system for trace-level determination of hazardous air pollutants." Sensors and Actuators B: Chemical **212**: 145-154.

Garstang, M. and D. R. Fitzjarrald (1999). Observations of surface to atmosphere interactions in the tropics, Oxford University Press.

Germano, M. F. and M. D. Oyama (2020). "Local circulation features in the eastern Amazon: high-resolution simulation." Journal of Aerospace Technology and Management **12**.

Gibbs, R. J. (1972). "Water chemistry of the Amazon River." Geochimica et Cosmochimica Acta **36**(9): 1061-1066.

Gloor, M., et al. (2013). "Intensification of the Amazon hydrological cycle over the last two decades." Geophysical Research Letters **40**(9): 1729-1733.

Greco, S., et al. (1992). "Low-level nocturnal wind maximum over the central Amazon basin." Boundary-Layer Meteorology **58**(1-2): 91-115.

Guenther, A., et al. (1995). "A global model of natural volatile organic compound emissions." Journal of Geophysical Research **100**(D5): 8873.

Guenther, A., et al. (2006). "Estimates of global terrestrial isoprene emissions using MEGAN (Model of Emissions of Gases and Aerosols from Nature)." Atmospheric Chemistry and Physics **6**(11): 3181-3210.

Guenther, A. B., et al. (2012). "The Model of Emissions of Gases and Aerosols from Nature version 2.1 (MEGAN2.1): an extended and updated framework for modeling biogenic emissions." Geoscientific Model Development **5**(6): 1471-1492.

Guimarães, P., et al. (2019). "Vertical profiles of ozone concentration collected by an unmanned aerial vehicle and the mixing of the nighttime boundary layer over an Amazonian urban area." Atmosphere **10**(10): 599.

Güntner, A. T., et al. (2016). "Selective sensing of isoprene by Ti-doped ZnO for breath diagnostics." Journal of Materials Chemistry B **4**(32): 5358-5366.

Hagan, D. H., et al. (2018). "Calibration and assessment of electrochemical air quality sensors by co-location with regulatory-grade instruments." Atmospheric Measurement Techniques **11**(1): 315-328.

Heus, T., et al. (2010). "Formulation of the Dutch Atmospheric Large-Eddy Simulation (DALES) and overview of its applications." Geoscientific Model Development **3**(2): 415-444.

IBGE (2021). "Brazillian Institute of Geography and Statistics." Retrieved Jan 6, 2021, from https://www.ibge.gov.br/.

Jiao, W., et al. (2016). "Community Air Sensor Network (CAIRSENSE) project: evaluation of low-cost sensor performance in a suburban environment in the southeastern United States." Atmospheric Measurement Techniques **9**(11): 5281-5292.

Kanan, S., et al. (2009). "Semiconducting metal oxide based sensors for selective gas pollutant detection." Sensors **9**(10): 8158-8196.

Kesselmeier, J., et al. (2009). "Natural volatile organic compound emissions from plants and their roles in oxidant balance and particle formation." Geophysical Monograph Series **186**: 183-206.

Kesselmeier, J. and M. Staudt (1999). Journal of Atmospheric Chemistry **33**(1): 23-88.

Korotcenkov, G. and B. K. Cho (2011). "Instability of metal oxide-based conductometric gas sensors and approaches to stability improvement (short survey)." Sensors and Actuators B: Chemical **156**(2): 527-538.

Kuhn, U., et al. (2010). "Impact of Manaus City on the Amazon Green Ocean atmosphere: ozone production, precursor sensitivity and aerosol load." Atmospheric Chemistry and Physics **10**(19): 9251-9282.

Lathière, J., et al. (2006). "Impact of climate variability and land use changes on global biogenic volatile organic compound emissions." Atmospheric Chemistry and Physics **6**(8): 2129-2146.

Lee, J., et al. (2009). "Distribution and Radiative Forcing of Tropical Thin Cirrus Clouds." Journal of the Atmospheric Sciences **66**(12): 3721-3731.

Leidinger, M., et al. (2014). "Selective detection of hazardous VOCs for indoor air quality applications using a virtual gas sensor array." Journal of Sensors and Sensor Systems **3**(2): 253-263.

Lewis, S. L. (2006). "Tropical forests and the changing earth system." Philosophical Transactions of the Royal Society B: Biological Sciences **361**(1465): 195-210.

Li, W., et al. (2020). "Identification of sea breeze recirculation and its effects on ozone in Houston, TX, during DISCOVER-AQ 2013." Journal of Geophysical Research-Atmospheres **125**(22).

Li, W., et al. (2016). "MOF-derived hierarchical hollow ZnO nanocages with enhanced low-concentration VOCs gas-sensing performance." Sensors and Actuators B: Chemical **225**: 158-166.

Lin, T., et al. (2019). "Semiconductor metal oxides as chemoresistive sensors for detecting volatile organic compounds." Sensors **19**(2): 233.

Liu, B., et al. (2020). "Vertical profiling of fine particulate matter and black carbon by using unmanned aerial vehicle in Macau, China." Science of The Total Environment **709**: 136109.

Liu, B., et al. (2020). "Vertical profiling of fine particulate matter and black carbon by using unmanned aerial vehicle in Macau, China." Science of the Total Environment **709**.

Liu, X., et al. (2020). "Low-cost sensors as an alternative for long-term air quality monitoring." Environmental research **185**: 109438.

Liu, Y., et al. (2016). "Isoprene photochemistry over the Amazon rainforest." Proceedings of the National Academy of Sciences **113**(22): 6125-6130.

Lu, L., et al. (2005). "Mesoscale circulations and atmospheric CO_2 variations in the Tapajós Region, Pará, Brazil." Journal of Geophysical Research: Atmospheres **110**: D21102.

Lu, L., et al. (2005). "Mesoscale circulations and atmospheric CO2 variations in the Tapajós Region, Pará, Brazil." Journal of Geophysical Research: Atmospheres **110**(D21).

Ma, Y., et al. (2021). "Optimization and representativeness of atmospheric chemical sampling by hovering unmanned aerial vehicles over tropical forests." Earth and Space Science.

Ma, Y., et al. (2021). "Optimization and representativeness of atmospheric chemical sampling by hovering unmanned aerial vehicles over tropical forests." Earth and Space Science **8**(4): e2020EA001335.

Ma, Y. M. and T. J. Lyons (2003). "Recirculation of coastal urban air pollution under a synoptic scale thermal trough in Perth, Western Australia." Atmospheric Environment **37**(4): 443-454.

Martin, S. T., et al. (2010). "An overview of the Amazonian aerosol characterization experiment 2008 (AMAZE-08)." Atmospheric Chemistry and Physics **10**.

Martin, S. T., et al. (2010). "Sources and properties of Amazonian aerosol particles." Reviews of Geophysics **48**(2).

Martin, S. T., et al. (2017). "The Green Ocean Amazon Experiment (GoAmazon2014/5) observes pollution affecting gases, aerosols, clouds, and rainfall over the rain forest." Bulletin of the American Meteorological Society **98**(5): 981-997.

Martin, S. T., et al. (2017). "The Green Ocean Amazon experiment (GoAmazon2014/5) observes pollution affecting gases, aerosols, clouds, and rainfall over the rain forest." Bulletin of the American Meteorological Society **98**(5): 981-997.

Martin, S. T., et al. (2016). "Introduction: observations and modeling of the Green Ocean Amazon (GoAmazon2014/5)." Atmospheric Chemistry and Physics **16**(8): 4785-4797.

McKinney, K. A., et al. (2019). "A sampler for atmospheric volatile organic compounds by copter unmanned aerial vehicles." Atmospheric Measurement Techniques **12**(6): 3123-3135.

Mead, M., et al. (2013). "The use of electrochemical sensors for monitoring urban air quality in low-cost, high-density networks." Atmospheric Environment **70**: 186-203.

Medeiros, A. S. S., et al. (2018). "River Breezes for Pollutant Dispersion in GoAmazon2014/5." Atmos. Chem. Phys. Discuss. **2018**: 1-28.

Miller, S. T. K., et al. (2003). "Sea breeze: Structure, forecasting, and impacts." Reviews of Geophysics **41**(3).

Mirzaei, A., et al. (2016). "Detection of hazardous volatile organic compounds (VOCs) by metal oxide nanostructures-based gas sensors: A review." Ceramics international **42**(14): 15119-15141.

NOAA (2020). "World Magnetic Model." Retrieved August 30, 2020, 2020, from https://www.ngdc.noaa.gov/geomag/calculators/magcalc.shtml.

Nobre, C. A., et al. (2009). "Understanding the climate of Amazonia: Progress from LBA." Amazonia and Global Change **186**: 145-147.

Oliveira, A. P. and D. R. Fitzjarrald (1993). "The Amazon river breeze and the local boundary layer: I. observations." Boundary-Layer Meteorology **63**(1): 141-162.

Oliveira, A. P. and D. R. Fitzjarrald (1994). "The Amazon river breeze and the local boundary layer: II. linear analysis and modelling." Boundary-Layer Meteorology **67**(1): 75-96.

Ouwersloot, H. G., et al. (2011). "On the segregation of chemical species in a clear boundary layer over heterogeneous land surfaces." Atmospheric Chemistry and Physics **11**(20): 10681-10704.

Paiva, R. C. D., et al. (2011). "Reduced precipitation over large water bodies in the Brazilian Amazon shown from TRMM data." Geophysical Research Letters **38**(4).

Pierce, T., et al. (1998). "Influence of increased isoprene emissions on regional ozone modeling." Journal of Geophysical Research: Atmospheres **103**(D19): 25611-25629.

Pijolat, C., et al. (1999). "Gas detection for automotive pollution control." Sensors and Actuators B: Chemical **59**(2-3): 195-202.

Pöschl, U., et al. (2010). "Rainforest aerosols as biogenic nuclei of clouds and precipitation in the Amazon." Science **329**(5998): 1513-1516.

Ramos da Silva, R., et al. (2011). "Cloud streets and land–water interactions in the Amazon." Biogeochemistry **105**(1-3): 201-211.

Ribeiro, I. O., et al. (2018). "Biomass burning and carbon monoxide patterns in Brazil during the extreme drought years of 2005, 2010, and 2015." Environmental Pollution **243**: 1008-1014.

Robeson, L. M. (2008). "The upper bound revisited." Journal of membrane science **320**(1-2): 390-400.

Sachse, G. W., et al. (1988). "Carbon monoxide over the Amazon Basin during the 1985 dry season." Journal of Geophysical Research **93**(D2): 1422.

Santos, M. J., et al. (2019). "Seasonal flooding causes intensification of the river breeze in the central Amazon." Journal of Geophysical Research: Atmospheres **124**(10): 5178-5197.

Santos, M. J., et al. (2014). "Influence of local circulations on wind, moisture, and precipitation close to Manaus City, Amazon Region, Brazil." Journal of Geophysical Research: Atmospheres **119**(23): 13233-13249.

Seinfeld, J. H. and S. N. Pandis (2016). Atmospheric Chemistry and Physics: from Air Pollution to Climate Change, John Wiley & Sons.

Shrivastava, M., et al. (2019). "Urban pollution greatly enhances formation of natural aerosols over the Amazon rainforest." Nature Communications **10**(1): 1046.

Silva Dias, M. A. F., et al. (2004). "River breeze circulation in eastern Amazonia: observations and modelling results." Theoretical and Applied Climatology **78**(1): 111-121.

Silva Dias, M. A. F., et al. (2004). "River breeze circulation in eastern Amazonia: observations and modelling results." Theoretical and Applied Climatology **78**(1-3): 111-121.

Simpson, J. E. (1994). Sea breeze and local winds., Cambridge University Press.

Sindelarova, K., et al. (2014). "Global data set of biogenic VOC emissions calculated by the MEGAN model over the last 30 years." Atmospheric Chemistry and Physics **14**(17): 9317-9341.

Sozzi, R., et al. (1998). "Method for estimation of surface roughness and similarity function of wind speed vertical profile." Journal of Applied Meteorology **37**(5): 461-469.

Spinelle, L., et al. (2017). "Review of portable and low-cost sensors for the ambient air monitoring of benzene and other volatile organic compounds." Sensors **17**(7): 1520.

Spinelle, L., et al. (2015). "Review of low-cost sensors for the ambient air monitoring of benzene and other volatile organic compounds." Eur. Union, Luxembourg City, Luxembourg, Tech. Rep. EUR **27713**.

Spinelle, L., et al. (2015). "Field calibration of a cluster of low-cost available sensors for air quality monitoring. Part A: Ozone and nitrogen dioxide." Sensors and Actuators B: Chemical **215**: 249-257.

Stewart, M. P. and S. T. Martin (2020). Atmospheric Chemical Sensing by Unmanned Aerial Vehicles. Unmanned Aerial Vehicles. Hauppauge, New York, Nova Science Publishers.

Tantekin-Ersolmaz, Ş. B., et al. (2001). "n-Pentane/i-pentane separation by using zeolite–PDMS mixed matrix membranes." Journal of Membrane Science **189**(1): 59-67.

Trebs, I., et al. (2012). "Impact of the Manaus urban plume on trace gas mixing ratios near the surface in the Amazon Basin: Implications for the NO-NO2-O3 photostationary state and peroxy radical levels." Journal of Geophysical Research: Atmospheres **117**(D5).

Van Den Broek, J., et al. (2018). "Highly selective and rapid breath isoprene sensing enabled by activated alumina filter." ACS Sensors **3**(3): 677-683.

van Emmerik, T. H. M., et al. (2013). "Measuring heat balance residual at lake surface using Distributed Temperature Sensing." Limnology and Oceanography: Methods **11**(2): 79-90.

van Heerwaarden, C. C. and J. V. G. de Arellano (2008). "Relative humidity as an indicator for cloud formation over heterogeneous land surfaces." Journal of the Atmospheric Sciences **65**(10): 3263-3277.

Venticinque, E., et al. (2016). "An explicit GIS-based river basin framework for aquatic ecosystem conservation in the Amazon." Earth Syst. Sci. Data **8**(2): 651-661.

Verburg, P. and J. P. Antenucci (2010). "Persistent unstable atmospheric boundary layer enhances sensible and latent heat loss in a tropical great lake: Lake Tanganyika." Journal of Geophysical Research: Atmospheres **115**: D11109.

Vilà-Guerau de Arellano, J., et al. (2005). "Transport and chemical transformations influenced by shallow cumulus over land." Atmospheric Chemistry and Physics **5**(12): 3219-3231.

Vilà-Guerau de Arellano, J., et al. (2011). "The role of boundary layer dynamics on the diurnal evolution of isoprene and the hydroxyl radical over tropical forests." Journal of Geophysical Research: Atmospheres **116**: D07304.

Vilà-Guerau de Arellano, J., et al. (2020). "Interactions between the Amazonian rainforest and cumuli clouds: a large-eddy simulation, high-resolution ECMWF, and observational intercomparison study." Journal of Advances in Modeling Earth Systems **12**(7): e2019MS001828.

Villa, T. F., et al. (2016). "Development and validation of a UAV based system for air pollution measurements." Sensors **16**(12): 2202.

Wang, H., et al. (2020). "Designer Metal – Organic Frameworks for Size - Exclusion - Based Hydrocarbon Separations: Progress and Challenges." Advanced Materials **32**(44): 2002603.

Wei, P., et al. (2018). "Impact analysis of temperature and humidity conditions on electrochemical sensor response in ambient air quality monitoring." Sensors **18**(2).

Wesely, M. L. (1989). "Parameterization of surface resistances to gaseous dry deposition in regional-scale numerical models." Atmospheric Environment **23**(6): 1293-1304.

Williams, R., et al. (2015). "Next generation air monitoring (NGAM) VOC sensor evaluation report." EPA: Washington, DC, USA.

Williams, R., et al. (2018). "Peer review and supporting literature review of air sensor technology performance targets." US Environmental Protection Agency: Washington, DC, USA.

Worldview (2020). "Worldview." Retrieved August 6, 2020, from https://worldview.earthdata.nasa.gov.

Yan, M., et al. (2021). "Humidity compensation based on power-law response for MOS sensors to VOCs." Sensors and Actuators B: Chemical **334**: 129601.

Ye, J., et al. (2021). "Near-canopy horizontal concentration heterogeneity of semivolatile oxygenated organic compounds and implications for 2-methyltetrols primary emissions." Environmental Science: Atmospheres **1**(1): 8-20.

Ye, J., et al. (2021). "River Winds and Local Dispersion of Atmospheric Volatile Organic Compounds in the Amazonian Riparian Ecoregion." submitted.

Zampolli, S., et al. (2009). "Real-time monitoring of sub-ppb concentrations of aromatic volatiles with a MEMS-enabled miniaturized gas-chromatograph." Sensors and Actuators B: Chemical **141**(1): 322-328.

Zampolli, S., et al. (2005). "Selectivity enhancement of metal oxide gas sensors using a micromachined gas chromatographic column." Sensors and Actuators B: Chemical **105**(2): 400-406.

Zanni, S., et al. (2018). "Indoor air quality real-time monitoring in airport terminal Aaeas: an opportunity for sustainable management of micro-climatic parameters." Sensors **18**(11): 3798.

Zhang, Y., et al. (2018). "Gas sensor based on samarium oxide loaded mulberry-shaped tin oxide for highly selective and sub ppm-level acetone detection." Journal of colloid and interface science **531**: 74-82.

Zhao, T., et al. (2021). "River winds and pollutant recirculation near the Manaus city in the central Amazon." Communications Earth & Environment **2**(1): 1-8.

Zhao, X., et al. (2018). "Metal-organic frameworks for separation." Advanced Materials **30**(37): 1705189.